Universitat Ramon Llull

DOCTORAL THESIS

Title	Correlation between cardiovascular disease biomarkers and biochemical and physical milieu in complex vascular environments
Presented by	Jordi Martorell López
Centre	IQS School of Engineering
Department	Chemical Engineering
Directed by	Dra. Mercedes Balcells Camps Dr. José Javier Molins Vara

C. Claravall, 1-3
08022 Barcelona
Tel. 936 022 200
Fax 936 022 249
E-mail: urlsc@sec.url.es
www.url.es

Acknowledgements

A la meva família, per recolzar-me incondicionalment en tots els aspectes de la meva vida i donar-me la plataforma mes sòlida possible pel meu creixement personal.

A la Dra. Merche Balcells, per no dubtar mai de les meves capacitats, per haver superat junts les adversitats, i per fer possibles els millors anys de la meva vida.

Al Dr. JJ Molins, porque siempre ha sabido ser el mejor espejo en el que mirarse durante el trayecto de Ingeniero a Doctor y Profesor.

To Professor Elazer R. Edelman, not only a prolific source of wisdom and inspiration but also a solid, reliable and reachable support whenever I needed him.

To Dr. Vipul Chitalia, Dr. Kumaran Kolandaivelu and Dr. Vijaya Kolachalama, for your help, your inputs and your different perspectives of life. By far, the three people I have learned the most from during this adventure.

Al Dr. Andrés A. García-Granada, al Dr. Guillermo Reyes y a César Alquézar, por su cercanía y solidaridad, colaborando siempre en aquellas facetas que menos dominaba.

To Dr. Adam Groothuis, to remind me that business and science should always run together.

To the members of the Edelman Lab and the employees of CBSET, an amazing group of smart, efficient and friendly people.

A la Emi, per impregnar-me d'esperit aventurer i de ganes d'aconseguir els meus objectius.

To Bill, because since the day I met you I knew that we would be friends forever.

A la Montse, per ser-hi sempre independentment de la situació personal mútua.

A la Clàudia, per aconsellar-me sàviament al llarg dels anys.

0.1 – Index

0.2 – List of abbreviations

AF: Arterial Flow

bFGF: Basic Fibroblast Growth Factor

BMS: Bare Metal Stent

CAD: Computer-Aided Design

CAM: Computer-Aided Manufacturing

CAMs: Cell Adhesion Molecules

CCA: Common Carotid Artery

CFD: Computer Fluid Dynamics

CNC: Computer Numerical Control

CS: Calf Serum

DES: Drug-Eluting Stent

DMEM: Dulbecco's Modified Eagle Medium

DFS: Dynamic Flow System

EBM-2: Endothelial cell Basal Medium-2

EGM-2: Endothelial Growth Medium-2

ELISA: Enzyme-Linked Immunosorbent Assay

EC: human coronary Artery Endothelial Cells

ECA: External Carotid Artery

EGF-1: Epidermal Growth Factor

eGFP: enhanced Green Fluorescent Protein

FBS: Fetal Bovine Serum

FCS: Fetal Calf Serum

FDA: Food and Drug Administration

H&E: Hematoxylin & Elastin

HSA: Human Serum Albumin

IA: Indoxil Acetate

ICA: Internal Carotid Artery

ICAM-1: InterCellular Adhesion Molecule

IF: Immunofluorescence

IGS: Initial Graphics exchange Specification

IGF: Insulin-like Growth Factor

IS: Indoxil Sulfate

JNK: c-Jun N-terminal Kinases

LAD: Left Anterior Descending coronary artery

LCX: Left Circumflex coronary artery

LDL: Low Density Lipoprotein

LM: Left Main coronary artery

mTOR: mammalian Target Of Rapamycin

NaOH: Sodium hydroxide

NF-κB: Nuclear Factor Kappa-light-chain-enhancer of activated B cells

NVV: Normalized vTan·VolRec

OF: Oscillatory Flow

Ox-LDL: Oxidized Low Density Lipoprotein

PBMC: Peripheral Blood Mononuclear Cells

PBS: Phosphate Buffer Saline

PDMS: Polydimethylsiloxane

PECAM-1: Platelet Endothelial Cell Adhesion Molecule-1

PGA: Polyglycolic Acid

PS: Penicillin + Streptomycin

PSG: Penicillin + Streptomycin + L-glutamine

PU: Polyurethane

SEM: Scanning Electron Microscopy

SMC: human aortic Smooth Muscle Cells

ST: Stent Thrombosis

STA: Static control

sTF: Soluble Tissue Factor

STL: STereoLithography

TCP: Tissue Culture Plate

TVEG: Tissue-Engineered Vascular Grafts

TF: Tissue Factor

TF: Tissue Factor Pathway Inhibitor

TNF-α: Tumor Necrosis Factor α

VCAM-1: Vascular Cell Adhesion Molecule-1

VEGF: Vascular Endothelial Growth Factor

vTan: Tangential velocity

VolRec: Volume of Recirculation

A: Area

CS: Control Surface

CV: Control Volume

D: Diffusivity

F: Force

L: cylinder Length

Q: Heat

U: Internal energy

V: Volume

Ws: Shaft Work

d: Diameter

e: Energy level

g: Gravity

n: Normal vector

p: Pressure

r: cylinder Radius

t: Time

u: Fluid velocity in x

v: Fluid velocity in y

w: Fluid velocity in z

θ: Concentration

μ: Viscosity

ρ: Density

0.3 – Figures, tables and equations

0.4 – Collaborations and funding

This thesis has been possible thanks to the combined effort of several researchers and laboratories. Here is a detailed list of collaborators and funding sources that have facilitated the success of this thesis.

Dr. Mercedes Balcells and Dr. José Javier Molins supervised every step of the thesis and Dr. Elazer Edelman gently offered senior tutorship to the whole project. The visual basic interface was developed, along with computational fluid dynamics simulations, at the chemical engineering department at IQS. They were tutored by Dr. Vijaya Kolachalama's and Dr. Caroline O'Brien from Dr. Edelman's Harvard-MIT Biomedical Engineering Center at MIT. Angioscopic data from real coronary patients was obtained thanks to Dr. Lawrence García from St. Elizabeth Hospital, while Doppler ultrasound records were obtained thanks to Dr. Blanca Molins at ICC Sant Pau. Vessel-like constructs were created using help from Dr. Andrés A. García-Granada, Dr. Guillermo Reyes and César Alquézar from the industrial engineering department at IQS, from Elisabet Rosàs, Pablo Santomá, Jay Wang, Eric Gómez, Alfredo Palmés, Cecilia Louis and Joseph Wallins who collaborated at MIT and finally Dr. Adam Groothuis, Dr. Brett Zani, Kathryn Regan and Philip Seifert at CBSET. Microparticle tracking was result of a collaboration with Dr. José Antonio Bea from Universidad de Zaragoza. All biological experiments were performed at MIT. Tissue factor work would have been impossible without Dr. Vipul Chitalia's insight and Dr. Kumaran Kolandaivelu's expertise.

The project used funds from different sources, listed here;

- Generalitat de Catalunya 2013FI_B2 00093
- Ministerio de Innovacion Plan Nacional BFU2009-09804
- NIH grant NIH/NIGMS RO1/GM049039
- NIH grant K08 DK080946
- Center for Integration of Medicine & Innovative Technology CIMIT Y11-177
- Cambra de Comerç de Barcelona
- MISTI Seed Fund 2010
- Fundació Empreses IQS
- POSIMAT

0.5 – Abstract

Progression of atherosclerosis and thrombosis in patients at risk of cardiovascular disease depend heavily upon the unique physical and biochemical environment of each individual. Characteristics such as vessel architecture, biochemical composition of blood or type of treatment define the outcome of cardiovascular interventions. Stent placement and graft positioning seek to recover vessel patency, yet are limited by restenosis and thrombosis. Composite, patient-specific, multi-scale models able to integrate microscopic cellular responses in the context of relevant macroscopic flow and structural conditions may help understand the progression of these events, providing insight into how to mitigate adverse responses in specific settings and individuals. Based on previously validated *in silico* and *in vitro* methods, an arterial replication platform was developed. Vascular architectures from coronary and carotid bifurcations were derived from clinical imaging and used to generate conjoint computational meshing for *in silico* analysis and polymeric, biocompatible scaffolds for *in vitro* models. In parallel with three dimensional flow simulations, the geometrically-realistic constructs were seeded with vascular cells critical to vessel hemostasis and response to injury and exposed to relevant, physiologic flows and uremic, inflammatory or anti-proliferative conditions. Following functional characterization, *in vitro* surrogates of atherosclerotic and thrombogenic progression were locally quantified and correlated with the biological, chemical and physical characteristics of the cellular environment. The extent of recirculation and the presence of inflammatory agents, anti-proliferative chemicals and uremic serum and solutes were critical to the activation of atherosclerosis and thrombosis progression biomarkers. Integrated frameworks such as the one described in this thesis could be very useful in a range of biomedical fields. The platform may help researchers to answer an array of biological and clinically relevant questions and holds the capacity to cast bioimplantable vascular grafts in a close future.

La progresión de la aterosclerosis y la trombosis en pacientes con riesgo de enfermedad cardiovascular depende en gran medida del entorno único a nivel físico y bioquímico de cada individuo. Características tales como la arquitectura de la vasculatura, composición bioquímica de la sangre o el tipo de tratamiento definen el resultado de las intervenciones cardiovasculares. La colocación de un *stent* o de un *bypass* busca recuperar la permeabilidad del vaso, pero se ve limitada por la restenosis y la trombosis. El diseño de modelos multi-escala específicos para cada paciente puede ayudar a entender la progresión de estos eventos al tener capacidad para integrar las respuestas celulares microscópicas en el contexto del flujo macroscópico y de las condiciones estructurales. Dichos modelos pueden proporcionar información sobre cómo mitigar respuestas adversas en función de cada individuo. Usando métodos *in silico* e *in vitro* previamente validados se ha desarrollado una plataforma de replicación arterial para reproducir bifurcaciones vasculares coronarias y carótidas derivadas de imágenes clínicas, que se han usado para generar archivos computacionales para análisis *in silico* por un lado y para fabricar modelos arteriales poliméricos biocompatibles para análisis *in vitro* por otro. En paralelo con las simulaciones de flujo, los modelos físicos fueron sembrados con células vasculares centrales en la hemostasia y la respuesta a las lesiones. Los modelos vasculares fueron expuestos a flujos fisiológicos relevantes y a entornos urémicos, inflamatorios o anti-proliferativos. Tras la caracterización funcional de los modelos, el progreso de la aterosclerosis y la trombosis se cuantificó a nivel local y se correlacionó con las características biológicas, químicas y físicas del entorno celular. La cantidad de recirculación y la presencia de agentes inflamatorios, productos químicos anti-proliferativos y de suero y solutos urémicos fueron críticos para la activación de los biomarcadores de evolución de aterosclerosis y trombosis. Plataformas integradas tales como la descrita en esta tesis podrían ser muy útiles en una variedad de campos de la biomedicina. La plataforma puede ayudar a los investigadores a responder una serie de cuestiones biológicas clínicamente relevantes y tiene la capacidad de producir injertos vasculares bioimplantables en un futuro próximo.

La progressió de l'aterosclerosi i la trombosi en pacients amb risc de malaltia cardiovascular depèn en gran mesura de l'entorn únic a nivell físic i bioquímic cada individu. Característiques tals com l'arquitectura de la vasculatura, la composició bioquímica de la sang o el tipus de tractament defineixen el resultat de les intervencions cardiovasculars. La col·locació d'un *stent* o d'un *bypass* busca recuperar la permeabilitat del vas, però es veu limitada per la restenosis i la trombosi. El disseny de models multi-escala específics per a cada pacient pot ajudar a entendre la progressió d'aquests esdeveniments en tenir la capacitat per integrar les respostes cel·lulars microscòpiques en el context del flux macroscòpic i de les condicions estructurals. Aquests models poden proporcionar informació sobre com mitigar respostes adverses en funció de cada individu. Emprant mètodes *in silico* i *in vitro* prèviament validats, s'ha desenvolupat una plataforma de replicació arterial per reproduir bifurcacions vasculars coronàries i caròtides derivades d'imatges clíniques que s'han fet servir per generar arxius computacionals per a anàlisi *in silico* per una banda i per fabricar models arterials polimèrics biocompatibles per a anàlisis *in vitro* de l'altra. En paral·lel amb les simulacions de flux, els models físics van ser sembrats amb cèl·lules vasculars centrals en l'hemostàsia i la resposta a les lesions. Els models vasculars van ser exposats a fluxos fisiològics rellevants i a entorns urèmics, inflamatoris o anti-proliferatius. Després de la caracterització funcional dels models, el progrés de l'aterosclerosi i la trombosi es va quantificar a nivell local i es va correlacionar amb les característiques biològiques, químiques i físiques de l'entorn cel·lular. La quantitat de recirculació i la presència d'agents inflamatoris, productes químics anti proliferatius i de sèrum i soluts urèmics van ser crítics per a l'activació dels biomarcadors d'evolució d'aterosclerosi i trombosi . Plataformes integrades tals com la descrita en aquesta tesi podrien ser molt útils en una varietat de camps de la biomedicina. La plataforma pot ajudar els investigadors a respondre una sèrie de qüestions biològiques clínicament rellevants i té la capacitat de produir empelts vasculars bioimplantables en un futur pròxim.

1 – INTRODUCTION

The endothelium, a monolayer of endothelial cells (EC) that lines the inner surface of blood vessels, is exposed to a complex biomechanical milieu (Figure 1, Figure 2). EC are responsible for relaying biochemical messages regulators that ensure blood fluidity, nutrient transport and an appropriate control of coagulation to the underlying tissue and flowing blood. In the presence of local injury, the smooth muscle cell (SMC) multilayer becomes exposed to flow and interactions between EC and SMC in the presence of hemodynamic forces lead to a cascade of reactions that modulate vessel patency, promote low-density lipoprotein internalization, cell adhesion molecular expression, monocyte adhesion and tissue factor expression. EC-SMC crosstalk and their interactions with the local environment has been the subject of research for several years. Within the realm of understanding the impact of flow and vascular repair due to injury, previous work focused on developing bench-top model systems to examine the differences in EC biology in the presence and absence of SMC and understanding the regulatory interaction between alterations in hemodynamics and the vessel wall.

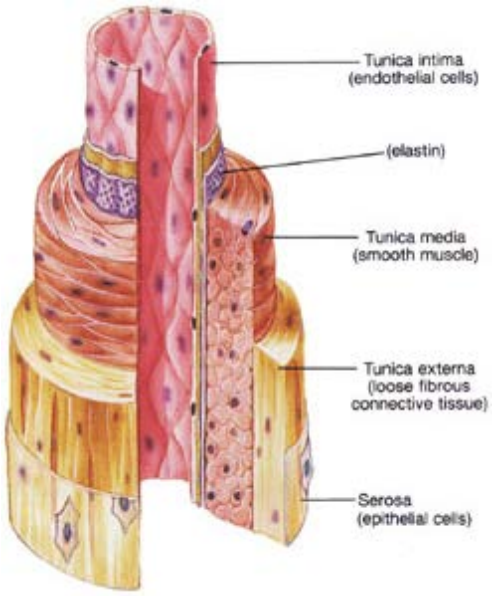

Figure 1 - Arterial vessel anatomy[1]

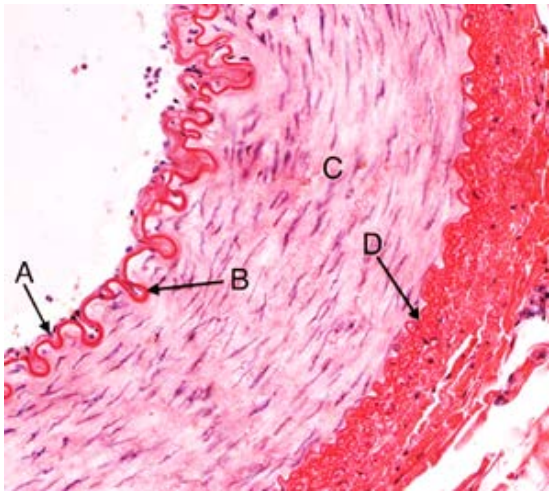

Figure 2 - Cross section of an artery A= EC, B= Elastin, C= SMC, D = Adventitia

While it is known that EC are especially sensitive to flow, the focus in these studies lacked the sophistication to truly replicate the physiologic environment of the vasculature. Over the last decades, biomedical engineers, in collaboration with physicians, biologists, chemists, physicists and mathematicians, have developed models to explain how the impact of vascular interventions on blood flow predicts subsequent vascular repair and other biological responses[2]. These models have become increasingly sophisticated and precise, propelling us toward optimization of cardiovascular therapeutics in general and personalizing treatments for patients with cardiovascular disease and its most common cause: atherosclerosis. In this thesis, vessel-like bench-top constructs were designed to evaluate the underlying relationships between flow disruptions and local expressions of atherogenic and thrombotic markers.

1.1 – Effects of flow disruptions

Blood vessels are constantly exposed to various types of hemodynamic forces, such as hydrostatic pressure, cyclic stretch and fluid shear stress, all induced by the pulsatile blood pressure and flow. Endothelial cells bear most of the wall's shear stress, which is the component of frictional forces arising from blood flow and acting parallel to the vessel luminal surface[3]. These cells are very sensitive to such hemodynamic forces, which can be significantly altered in regions with disturbed flow. Disturbed flow may occur in the vascular system for a number of reasons[4]. Flow disturbances that naturally occur in certain regions like vessel bifurcations or curves, flow alterations generated in arteries through surgical interventions such as bypass grafts and stent deployments, flow disturbances as a consequence of disease, such as reflux through dysfunctional venous valves, among other causes.

Alternatively, when the compensating artery enlargement is excessive, vessel can become patulous and aneurismal. Compensatory hemodynamic forces attempt to maintain arterial flow by constantly remodeling the vessel that often sacrifices luminal patency, stress and/or geometry. EC exposed to disturbed flow with a low and reciprocating shear stress and EC exposed to a laminar flow with a relatively high shear stress show different responses in terms of molecular signaling, gene expression, structure and function. For example, endothelial cells exposed to disturbed flow are round in shape, with short and randomly distributed actin filaments located mainly at the periphery of the cells[5], while endothelial cells exposed to laminar flow with high shear stress are aligned in the direction of the flow, with parallel actin stress fibers in the central regions. EC exposed to disturbed flow also have a higher DNA synthesis rate, which enhances proliferation[6]. Furthermore, disturbed flow increases permeability to macromolecules such as albumin or low-density lipoproteins (LDL)[7] and increases the degree of heterogeneity in gene expression in EC[8]. This heterogeneity leads to an intensification in the levels of certain transcription factors (such as NF-κB or EGF-1)[9], cell adhesion molecules (like ICAM-1, VCAM-1 or E-selectin[10]) and other receptors such as the LDL receptor[11]. Flow alterations also regulate platelet aggregation[12] and enhancement of fibronectin deposition[13]. The described biological effects of disturbed flow are summarized in Table 1.

Many of these effects are directly related to vascular disease and atherosclerosis. The formation of atherosclerotic plaques is enhanced in dysfunctional endothelium, where the greater permeability to macromolecules such as lipoproteins, the increased expression of

adhesion molecules and the enhanced recruitment of monocytes/macrophages in the intima - among other effects - favor the progression and development of the disease. Therefore, the disturbed and laminar flow patterns induce differential molecular responses in endothelial cells, which results in a preferential localization of atherosclerotic lesions. Two different combined mechanisms[14] explain the differential impact of atherosclerosis and thrombosis in arterial bifurcations. On the one hand, non-idealities in flow, "the shear stress theory" modify the endothelial response to flow by activating the NF-kB pathway and consequently trigger the expression of cell adhesion molecules and other inflammation markers. On the other hand, the "mass-transfer theory" states that the cell uptake kinetics of lipids and other solutes are concentration- and time-dependent so cells in low shear stress recirculating areas such as those in the bifurcations are more prone to uptake solutes such as Ox-LDL or sTF and to recruit monocytes.

BIOMARKER	Uniform flow 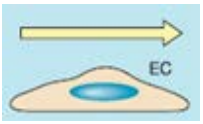	Disturbed flow 
Vasoactivity	Vasodilation	Vasoconstriction
Turnover rate	Low	High
Macromolecular permeability & LDL Uptake	Low	High
DNA synthesis	Low	High
Morphology	Elongated	Polygonal
Expression of CAMs genes	Low	High
Expression of antioxidant genes	High	Low
WBC adhesion and platelet genes	Inhibition	Promotion
Oxidative stress	Low	High (sustained)
SMC activation	Low	High
Endothelialization after wound repair	Promotion	Retardation
Heterogeneity	Low	High
Fibronectin and fibrinogen deposition	Low	High
Atherosclerosis and thrombosis	Prevention	Promotion

Table 1 - Effects of disturbed flow on EC[4]

1.2 – Atherosclerosis

Atherosclerosis is a major cause of concern throughout the world leading to millions of deaths annually[15]. Atherosclerosis affects all arterial beds but atherosclerotic lesions form more prominently in the vicinity of branch points and areas of curvature, which are more vulnerable than unbranched tubular arterial segments[4, 16, 17]. In these areas, fluid mechanic disturbances such as non-uniform laminar flow associated with boundary layer separation, recirculation and stagnation produce severe temporal and spatial gradients in wall shear stress distributions. These hemodynamic forces are powerful regulators of vascular function on a molecular, cellular and tissue level[18].

Atherosclerosis is a slow and complex cardiovascular disease that usually affects large and medium-sized arteries and is characterized by a thickening of the portion of the arterial vessel wall closest to the lumen (Figure 3). Atheromas are not merely filled with lipid, but contain cells whose functions critically influence atherogenesis[19]. Oxidized low density lipoprotein (Ox-LDL) activates inflammatory processes at the level of gene transcription by upregulation of nuclear factor kappa-b (NF-κB), expression of adhesion molecules (CAMs, such as VCAM-1 or ICAM-1), and recruitment of monocytes[20, 21]. As they continue to ingest chemically modified lipids and lipoproteins, monocytes become macrophages, which become foam cells and initiate fatty streaks. These activated macrophages produce numerous factors that are injurious to the endothelium[22, 23]. The inflammatory process leads to the formation of a fibrous plaque which consists of a mass of lipid-engorged monocytes[24] covered by a fibrous cap and being pushed out into the vessel lumen by smooth muscle cells[25] (Figure 4). Atheromatous plaques progressively encroach on the lumen to produce luminal narrowing and reduce flow to the end-organ. In adverse scenarios, localized plaques may rupture and migrate distally to entirely obstruct vascular perfusion and cause severe medical complications or even death.

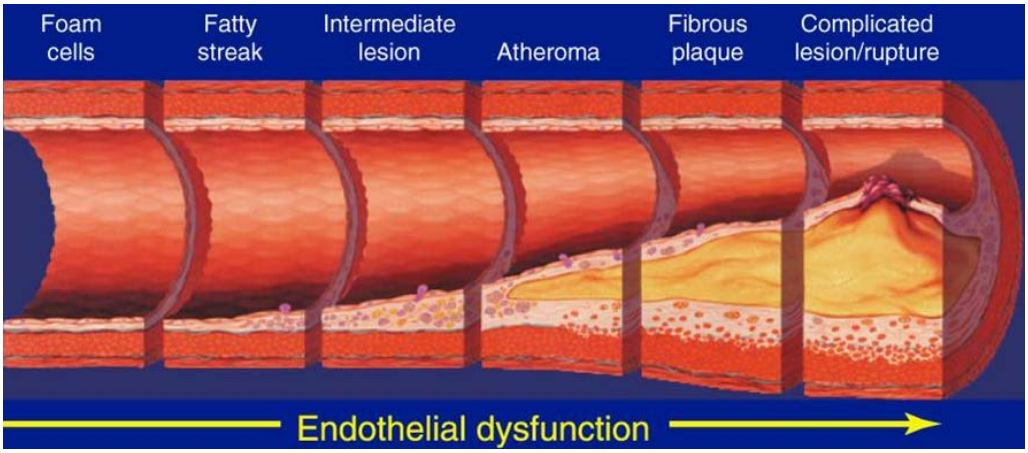

Figure 3 - Atherosclerosis evolution[26]

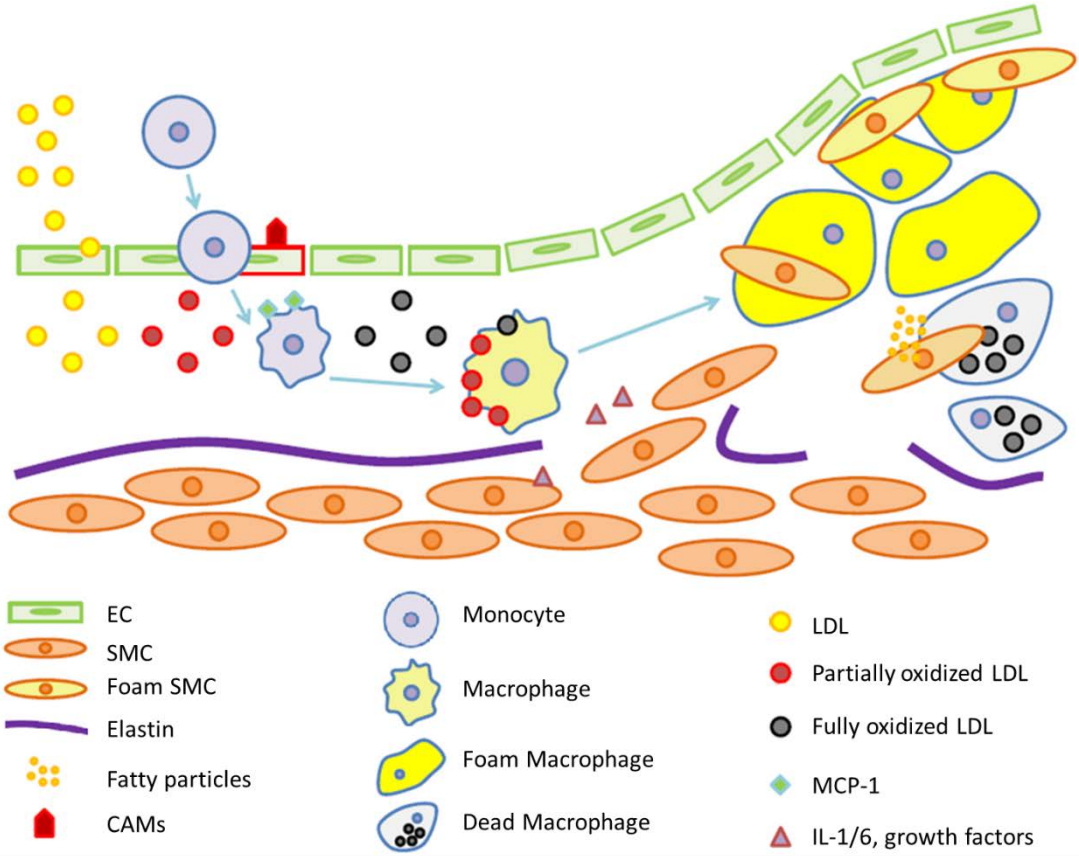

Figure 4 - Atherosclerotic mechanisms[27]

1.3 – Stents and grafts, the medical treatments against developed atherosclerosis

Clinical treatment for atherosclerosis has evolved tremendously over many decades and in the current generation, percutaneous interventions such as stents and grafts have assumed the main stage for many reasons, like their ease of use.

Since Voorhees et al. replaced diseased blood vessels with tubes of synthetic fabric[28] in 1952, there have been numerous attempts to design a vascular graft that not only matches the mechanical properties of the native vasculature, but also promotes cell growth, facilitates extracellular matrix production and inhibits thrombogenicity. Approximately 1.4 million US patients per year require arterial prostheses[29]. Synthetic polymer materials, especially expanded polytetrafluoroethylene (ePTFE) and polyethylene terephtalate (Dacron), are the dominant materials used for applications requiring large-diameter (>6mm) vessels[30].

In smaller diameter grafts, however, thrombogenicity and compliance mismatch re-occlude the bypassed vessel[31, 32], limiting the use of synthetic grafts in applications such as coronary artery bypass surgeries (one third of the arterial prosthesis procedures performed each year). In these cases, autologous vasculature is used unless precluded by disease, trauma or anatomic abnormalities[29]. The high occlusion rates of synthetic polymer materials has motivated further strategies to functionalize the luminal surface of graft materials such as coatings, chemical and protein modifications and endothelial cell seeding. Although there have been some promising results, synthetic grafts still induce chronic inflammation and thrombogenicity[33].

More recently, tissue-engineered vascular grafts (TEVG) have emerged to overcome the limitations of synthetic grafts. In TEVG, a synthetic or natural biodegradable material acts as a scaffold where vascular cells are seeded. The extracellular matrix produced by the cells gradually replaces the degrading scaffold. The matrix created, decellularized or not, is then implanted to the patient[30]. This technology provides more favorable hemodynamics, mechanical properties and suture force retention than previous synthetic grafts[34]. Polyglycolic acid (PGA) is the preferred scaffold material as it is biocompatible and safely degrades through hydrolysis. Biomaterials engineers may adapt the hydrolysis kinetics to the specific patient needs by copolymerization with other polymers. Although tissue-engineered vascular grafts have yielded promising results; the long culture periods required, the low proliferative

capacity of cells isolated from elderly patients and the mechanical immaturity of the vessels at the time of *in vivo* implantation remain major drawbacks.

Stents are metal mesh tubes that are expanded within diseased arteries in order to push the obstructive atherosclerotic plaque and return the vessel to a form that re-establishes blood flow. Bare metal stents (BMS) were invented and implanted for the first time in the early 1990's patients suffering arterial obstructive diseases. The balloon angioplasty and stent deployment accomplished an instantaneous recovery of flow in the arteries but the device's presence inside the lumen could lead to hypersensitive reactions that re-occluded (restenosis) the arterial vessel and limited its functional lifetime to months[35-37].

Adding drugs to coatings on the stents allowed for the direct elution of lesion modifying agents from the struts to the vessel. Such modified devices showed promising results by significantly reducing the rates of restenosis[38]. In consequence, different drugs have been added to the stents in order to inhibit restenosis pathways, and the first drug-eluting stents (DES) were approved by the FDA in 2003. Although the initial results were very encouraging, with a reduction from 25.5% to 8.3% in restenosis risk[39], the prolonged presence of the drug in the arterial wall delayed arterial healing and led to fatal complications such as stent thrombosis in 2-3%[40, 41] of cases (although some authors consider this an underestimation[42]), with a mortality of 50%[43]. Impaired re-endothelialization[44], excessive fibrin deposition and induction of tissue factor expression[40] are some of the suggested causes of failure of drug eluting stents. To avoid those, practitioners introduced dual anti-platelet therapy for at least 12 months[40].

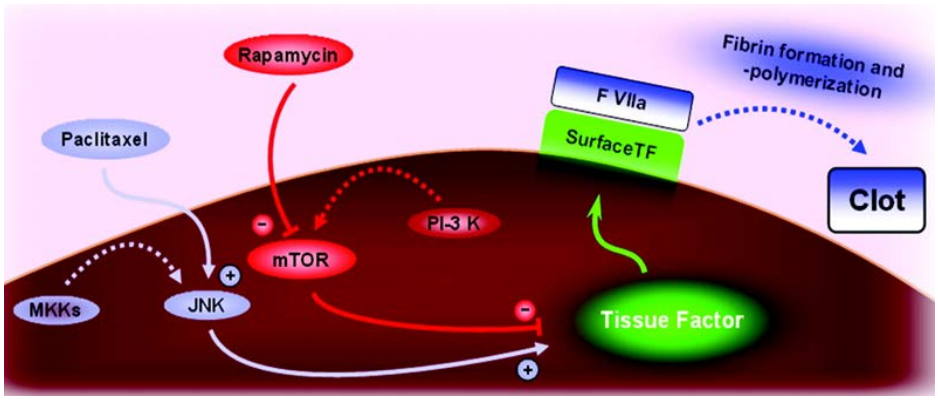

Figure 5 - Sirolimus and paclitaxel increase TF transcription[40]

Despite technological improvements, restenosis and stent and graft thrombosis continue to hamper the success of vascular implants applied to treat the diseased vessel. Implanting

vascular devices affects the vessel in different ways. It causes flow disruptions[45], which add up to the already complex flow regimes present in atherosclerotic regions[4, 16, 17]. Flow disruptions are a parameter to consider while aiming drug delivery to these regions. Device design must integrate the influence of flow and drug impact[46]. In addition, DES and drug eluting balloons locally add high doses of anti-proliferative drugs[47] to the unhealthy vessel which can impair the normal cellular behavior. Sirolimus and paclitaxel were the first drugs employed in DES. These have been shown to increase[40, 48] (Figure 5) the Tissue Factor (TF) transcription by two different pathways. While paclitaxel upregulates the JNK pathway, which directly upregulates TF transcription, Sirolimus inhibits mTOR pathway[48], which is an inhibitor of the TF transcription. How mTOR inhibits TF transcription remains elusive.

1.4 – Tissue factor biology and stent thrombosis

After percutaneous intervention, balloon angioplasty or stent implantation being the most common ones, the device deployed creates an injury[36], denudating the vessel from the already damaged endothelial monolayer and exposing smooth muscle cells to flow. In the absence of anticoagulant therapy, this injury initiates the coagulation cascade (Figure 6). When the vessel is injured, collagen and TF are released, starting the intrinsic and extrinsic pathways[49]. Both lead to create a blood clot that covers the injury and allows endothelial cells to proliferate and migrate to reconstruct the vessel. While the intrinsic pathway releases the intercellular collagen, the extrinsic pathway exposes the TF from the activated endothelium and from the sub-endothelial smooth muscle cells and fibroblasts (in case of deep injury) to blood. Both pathways, arbitrarily named extrinsic and intrinsic due to previous *in vitro* work, arrive to the common activation of Factor X[50]. Although both pathways initiate after an injury, the TF pathway seems to be the most relevant *in vivo*[51].

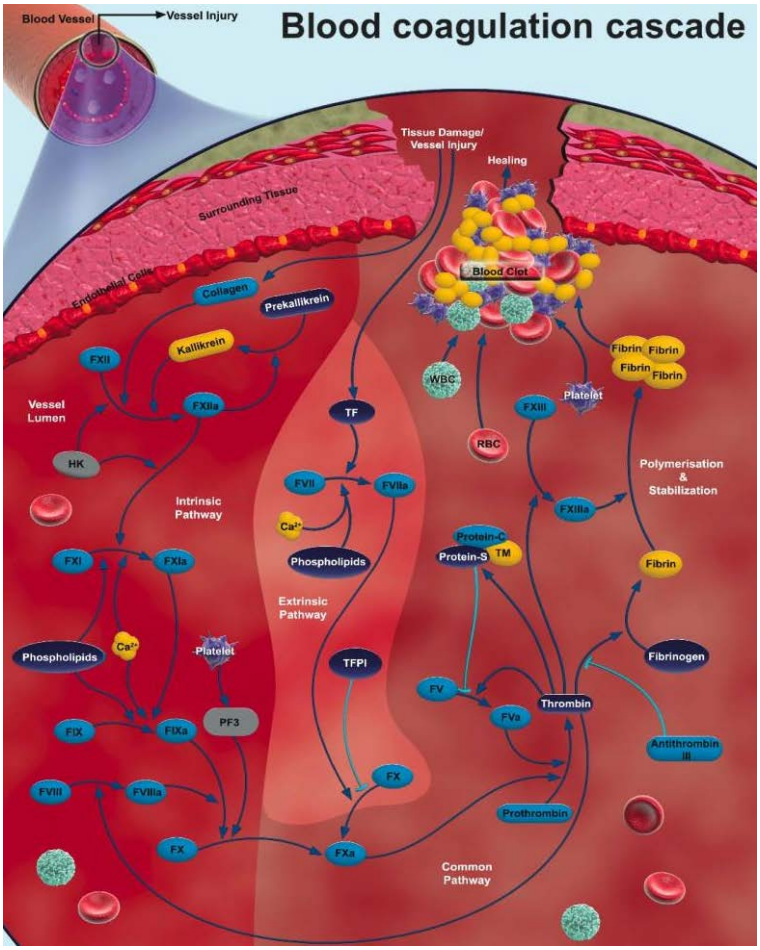

Figure 6 - The coagulation cascade[52]

Thrombosis is the formation of a blood clot inside a blood vessel, obstructing the flow of blood through the circulatory system[53]. Depending on the affected vessel and the degree of occlusion, thrombosis can lead to hypoxia, anoxia or even death. As seen in Figure 6, TF initiates the extrinsic pathway of the coagulation cascade. TF is a 47 kDa glycoprotein, a cytokine receptor class II, present in five pools (cellular and blood) (Figure 7). The protein transcription is activated by several cytokines; once transcribed from mRNA, the protein is buffered in pools inside the cytoplasm[54]. This buffer feeds the membrane with surface (active) and encrypted (inactive) TF[55, 56]. The active TF is monomeric, while the encrypted consists of a chain of TF monomers. It has been debated whether the formation of a disulfide bond Cys186-Cys 209 triggers the pro-coagulant activity and protein disulfide isomerase regulates the activation[55]. On the other hand, TF is released into the blood stream in two separate ways, as soluble TF (sTF)[57], being the external tail of the membrane protein that is released and the recently discovered TF-bearing microparticles. No methods have been solidly validated yet to quantify TF-bearing microparticles *in vitro* so they will remain out of the scope of this thesis.

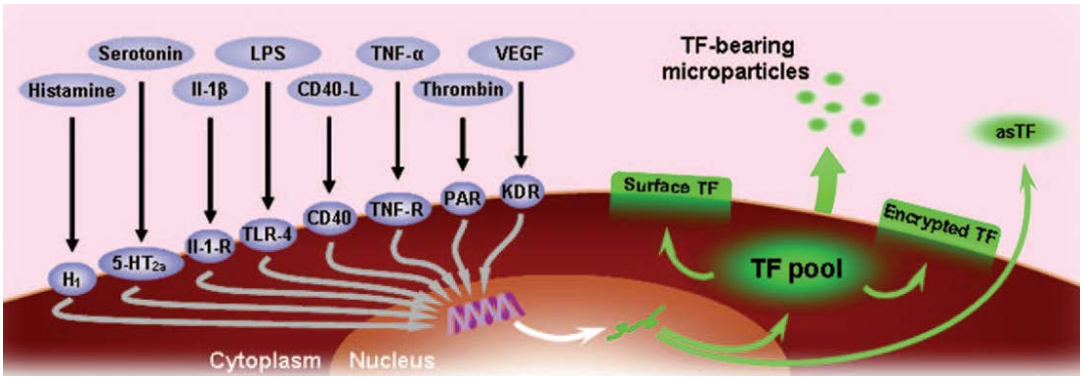

Figure 7 - TF transcription and distribution inside and outside the cells[56]

TF exposed on the denuded SMC surface serves as a key precipitant of injury-related local clot formation and can lead to stent thrombosis (ST), a potentially lethal event that kills up to half of patients. ST risk is particularly amplified in patients with chronic renal failure and end-stage renal disease. One-year cardiac mortality after coronary intervention risk can rise up to 6.5-fold from 1.9% to 15.2% and uremia predisposes to early, late and very late ST[58-63]. Multiple studies in CRF patients have shown increased circulating levels of regulators of thrombosis such as soluble TF, activated factor VIII, von Willebrand factor, TF pathway inhibitor, and fibrinogen[64-67]. The effects of uremia on local TF activity in various vascular cell types remain however scant. Although uremic serum is known to increase TF expression in EC[66], its effect on exposed SMC, the key driver of ST, remained undefined. The effect of the uremic serum and solutes on SMC TF expression, activity and SMC thrombogenicity will be examined[43] since

the published data suggested correlation between uremic milieu and hypercoagulability. Several studies have shown shear stress dependence on tissue factor expression and other coagulation cascade actors[68-70], but the results are sparse, and the literature is not clear about what the exact effect of flow on tissue factor expression is. Literature is divided in studying TF at pre-transcriptional, transcriptional or post-transcription level. This thesis will emphasize on cellular TF, which is responsible for coagulation, and soluble TF release, which can be internalized by- or signal to EC, always at post-transcriptional level.

1.5 – Vessel-like models

Atherosclerotic plaques preferentially form in certain regions of the vascular tree, such as bifurcations and curves, where the disturbed flow enhances a pro-atherosclerotic phenotype on endothelial cells. New vascular models must be able to reproduce these flow-dependent characteristics, as well as provide new tools to study and characterize the relationship between flow patterns and the endothelial function. Several *in vitro* and *ex vivo* models have been developed to explain partially the molecular mechanisms of atherogenesis, thrombosis and restenosis. It is now possible to tailor these models to include patient-specific characteristics in the search for personalized solutions. As the vascular system can be considered as a closed system, the interaction between flow and the endothelium can be studied using *in vitro* and *ex vivo* model systems or flow chambers.

In 1986, Badimon *et al*. designed the first *ex vivo* chamber[71], using de-endothelialized swine arteries to prove the relevance of shear rates on platelet deposition. In 2002, Blackman, García-Cardeña and Gimbrone, introduced the dynamic flow system (DFS)[72] as a culmination of decades of research about the effects of flow on endothelial cell biology[8, 73]. The DFS consists of tissue culture wells seeded with functional endothelial cells under controlled humidity, temperature and CO_2 levels, coupled to a conical device that generates a controlled flow over the cultured cells. Also in 2002, Kolandaivelu and Edelman designed and *ex vivo* system to study stent thrombogenicity[74, 75]; where a rotor provides a customizable inertial flow, so the waveforms are totally controlled. This model has been used to study and optimize stent designs and enlighten different aspects of stent thrombosis[76], among other uses.

EC are not only in direct contact with blood flow but also interact with their underlying cellular neighbors (typically, smooth muscle cells). It is then relevant to consider more than one cell type in these models. Balcells *et al*. proved that some flow-dependent endothelial pathways are less affected by flow when intact vascular smooth muscle cells are present in the system[44]. These findings, together with other relevant studies, suggest that the optimal strategy to create a physiologically relevant *in vitro* model depends on the cell types considered and the *in vivo* micro and macro environment simulated.

Finally, computational models have gained increasing acceptance as valuable tools to predict physical, chemical and biological phenomena in arteries. Computational fluid dynamics (CFD) simulations can predict with micrometric precision several physical and biological variables,

such as velocity, shear stress and drug distribution profiles. Recent studies[47] couple the computational results with *in vivo* experience, but this is only possible when classic mass transport equations and molecule-specific uptake kinetics are considered together and with accurate input parameters derived and validated from *in vivo* conditions[77]. CFD simulations are limited by their input validity, but when validated, they offer a platform for repeatable and quantifiable assays, across a spectrum of dependent parameters and environmental conditions – a feature unachievable with biological and animal testing.

Despite all the efforts made over the last decades, new approaches are needed to obtain more precise and informative models, capable of answering biological and clinically relevant questions, and focusing on patient-specific characteristics. Considering the uniqueness of each patient's vascular architecture and knowing how each particular geometry determines the hemodynamic characteristics and, subsequently, the biological response remain the major challenges for present and future vascular models.

1.6 – Fluid mechanics in arterial environments

The conservation of mass, momentum and energy laws provide the basic controls to understand fluid behavior in any system. Complex continuum equations derived from the conservation laws define the three-dimensional behavior of fluid flows. If one wants to fully describe a system, the strategy is dividing the volume to study into n infinitesimal control volumes and apply the Navier-Stokes equations to each infinitesimal control volume.

In CFD, the software divides the volume of interest into a finite number of volumes and applies Navier-Stokes to each volume. The refinement in size of the mesh of volumes created is critical to determine the quality of the solutions. There are very few analytical solutions to the Navier-Stokes equations and hence assumptions are made to numerically solve them for each control volume. In the case of arterial flow, models differ as a function of the assumptions that are made. The models can go from the simple laminar, Newtonian fluid flow model to extremely complex pseudo-turbulent, shear-rate dependent viscosity models. It is challenging to choose the most appropriate model since the comparisons between real and estimated flows are hard to obtain empirically. It is important to clarify the limits of refinement of the equations used and variables and parameters evaluated to define the scope of study in arterial flow mechanics.

The Navier-Stokes equations were discovered after deriving the fundamental conservation laws for an infinitesimal control volume (CV) and its control surfaces (CS)[78]. The conservation of mass, where ρ is the fluid density, Vel is the fluid's velocity, t is time, $\hat{n}$ is a normal vector to the surface, A is the area and V the volume, reads:

$$\int_{CV} \frac{\partial \rho}{\partial t} dV + \int_{CS} \rho \cdot \overrightarrow{Vel} \cdot \hat{n} \cdot dA = 0$$

Equation 1 - Conservation of mass

In the case of steady flow, the partial derivatives versus time of every variable are 0. The equation of continuity derives from the conservation of mass law, where u, v and w are the x, y and z components of the velocity, and states:

$$\frac{\partial u}{\partial x} + \frac{\partial v}{\partial y} + \frac{\partial w}{\partial z} = \nabla \overrightarrow{Vel} = 0$$

Equation 2 - Equation of continuity

After deriving the second law of Newton for the infinitesimal control volume of a fluid one can observe that the vector sum of all external forces (F) acting on the control volume is equal to the sum of the total rate of change of momentum of mass within the control volume and the rate of flux of momentum through the control surface. This relationship is known as the conservation of momentum law:

$$\vec{F} = \int_{CV} \frac{\partial(\rho\overrightarrow{Vel})}{\partial t} dV + \int_{CS} \left(\rho \cdot \overrightarrow{Vel}\right) \cdot \overrightarrow{Vel} \cdot \hat{n} \cdot dA$$

Equation 3 - Conservation of momentum

Finally, the conservation of energy law reveals that the rate of heat (Q) added to the control volume minus the rate at which shaft work (Ws) is done is equal to the rate of change of energy within the control volume. In the conservation of energy equation, e is the energy level, U is the internal energy, p is pressure, g is the gravity and z is height.

$$\frac{\partial}{\partial t} \int_{CV} e \cdot \rho \cdot dV + \int_{CS} \rho \cdot \left(U + \frac{p}{\rho} + \frac{Vel^2}{2} + g \cdot z\right) \cdot \overrightarrow{Vel} \cdot \hat{n} \cdot dA = \frac{dQ}{dt} - \frac{dWs}{dt}$$

Equation 4 - Conservation of energy

It is generally assumed that the state of a given mass of fluid in the control volume in an equilibrium state is uniquely specified by two parameters, such as the mass density ρ and the pressure p. All other quantities, such as the temperature T in this case, are functions of these two state parameters. The conservation laws contain all the unknown variables (velocity, pressure, density and temperature) and are enough to determine the system. Derived from the conservation of momentum, applying the equation of continuity and assuming newtonian fluid (constant viscosity μ) and pressure as only force term, the Navier-Stokes equations read, for each direction x, y and z and their respective velocities u, v and w:

$$\rho \cdot g_x - \frac{\partial p}{\partial x} + \mu \cdot \left(\frac{\partial^2 u}{\partial x^2} + \frac{\partial^2 u}{\partial y^2} + \frac{\partial^2 u}{\partial z^2}\right) = \rho \cdot \left(\frac{\partial u}{\partial t} + u \cdot \frac{\partial u}{\partial x} + v \cdot \frac{\partial u}{\partial y} + w \cdot \frac{\partial u}{\partial z}\right)$$

$$\rho \cdot g_y - \frac{\partial p}{\partial y} + \mu \cdot \left(\frac{\partial^2 v}{\partial x^2} + \frac{\partial^2 v}{\partial y^2} + \frac{\partial^2 v}{\partial z^2}\right) = \rho \cdot \left(\frac{\partial v}{\partial t} + u \cdot \frac{\partial v}{\partial x} + v \cdot \frac{\partial v}{\partial y} + w \cdot \frac{\partial v}{\partial z}\right)$$

$$\rho \cdot g_z - \frac{\partial p}{\partial z} + \mu \cdot \left(\frac{\partial^2 w}{\partial x^2} + \frac{\partial^2 w}{\partial y^2} + \frac{\partial^2 w}{\partial z^2}\right) = \rho \cdot \left(\frac{\partial w}{\partial t} + u \cdot \frac{\partial w}{\partial x} + v \cdot \frac{\partial w}{\partial y} + w \cdot \frac{\partial w}{\partial z}\right)$$

Equation 5 - Navier-Stokes equations

Or, in its vector and most commonly cited form:

$$\rho \cdot \vec{g} - \nabla p + \mu \cdot \nabla^2 \overrightarrow{Vel} = \rho \cdot \left(\frac{\partial \overrightarrow{Vel}}{\partial t} + \overrightarrow{Vel} \cdot \nabla \overrightarrow{Vel}\right)$$

Equation 6 - Navier-Stokes equations in vector form

The Navier-Stokes system and its derivative equations will be used by CFD software to solve the system using the Finite Elements Method (cf. Introduction 1.7). However, Navier-Stokes only solves velocity components in flow. If one want to solve mass transfer problems, the advection and diffusion equations will be added. This equation is called the material derivative, where θ is the concentration of the studied solute and D the operator "material derivative".

$$\frac{\delta \theta_i}{\delta t} + u_j \frac{\delta \theta_i}{\delta x_j} = D \frac{\delta^2 \theta_i}{\delta x_j^2}$$

Equation 7 - Material derivative of the concentration

Finally, Equation 8 allows the CFD software to evaluate the mass transfer problems in parallel with the velocity, pressure and related mechanic unknowns. In this equation, θ is the concentration of the species, $\underline{u}$ is the fluid velocity, D is the diffusivity.

$$\left[\frac{\partial \theta}{\partial t} + \left(\underline{u} \cdot \nabla \theta\right)\right] - \nabla(D \nabla \theta) = 0$$

Equation 8 - Mass transport scheme used by Tdyn®

The viscosity of a fluid is crucial to define its velocity profile through a pipe. Considering blood vessels perfect cylindrical pipes and deriving the conservation of energy laws for horizontal cylindrical pipes with null shaft, the Hagen-Poiseuille law states that the difference of pressure along the length L of a vessel follows Equation 9. The adimensional Reynolds number gives information on the regime of a flow in a pipe with diameter d. Only flows through pipes with Reynolds number higher than 2300 are considered turbulent.

$$P1 - P2 = u \cdot (8 \cdot L \cdot \mu)/(\pi \cdot r^4)$$

Equation 9 - Hagen-Poiseuille law

$$Re = \rho \cdot Vel \cdot d/\mu$$

Equation 10 - Reynolds number

One obtains a parabolic equation after integrating the Hagen-Poiseuille expression. Blood flow velocity generally has a parabolic profile, with maximum speed in the center of the vessel and gradually decreasing symmetrically toward the walls (Figure 8). The velocity profile is not only a function of space but also a function of time. Arterial pulse is different for each artery, and is a complex function of the arterial network upstream and downstream of the studied artery. However, healthy arteries close to the aorta should ideally show a perfect peak, similar to a narrowed Gaussian distribution. Equation 11 describes parabolic flow through a pipe and the Gaussian distribution function for velocity in arteries is show in Equation 12. In those equations, x_0, y_0 and z_0 are the coordinates of the center of the inlet, r is the radius of the pipe, t_{pulse} is the time of the pulse and σ is the width of the pulse.

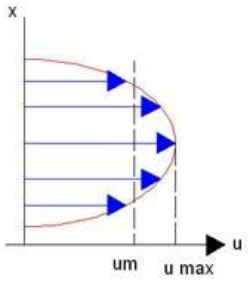

Figure 8 - Parabolic velocity profile

$$v = v_0 \cdot (1 - \frac{(x - x_0)^2 + (y - y_0)^2 + (z - z_0)^2}{r^2})$$

Equation 11 - Parabolic velocity profile

$$v_0 = v_{max} \cdot \mathrm{e}^{-\frac{(\mathrm{t}-\mathrm{t}_{\mathrm{pulse}})^2}{\sigma^2}}$$

Equation 12 - Gaussian distribution for a pulse

The existence of a stenosis involves, according to the Hagen-Poiseuille law, two main hemodynamic effects: an increase of speed at its center point and a decrease in the immediate post-stenosis region. The velocity increase is manifested by an increase in flow acceleration and a decrease in pressure. Both effects have been correlated with the parietal lesion progression. Predicted by Paterson and demonstrated by Burton, the atheroma growth and embolization is favored when multiple channels or intraplaque fissures generate a terminal pressure gradient higher than the central stream. Burton showed that the maximum risk of plaque rupture and secondary thrombus formation is associated with hypertension, since the increased pressure gradient promotes intraplaque vibration. Furthermore, and helped by the Venturi effect, the increase in acceleration would favor the expansion of the plate[79]. In the segment immediately to the stenosis, velocity near the wall dramatically decreases leading to lower shear stress and even recirculating regimes (Figure 9).

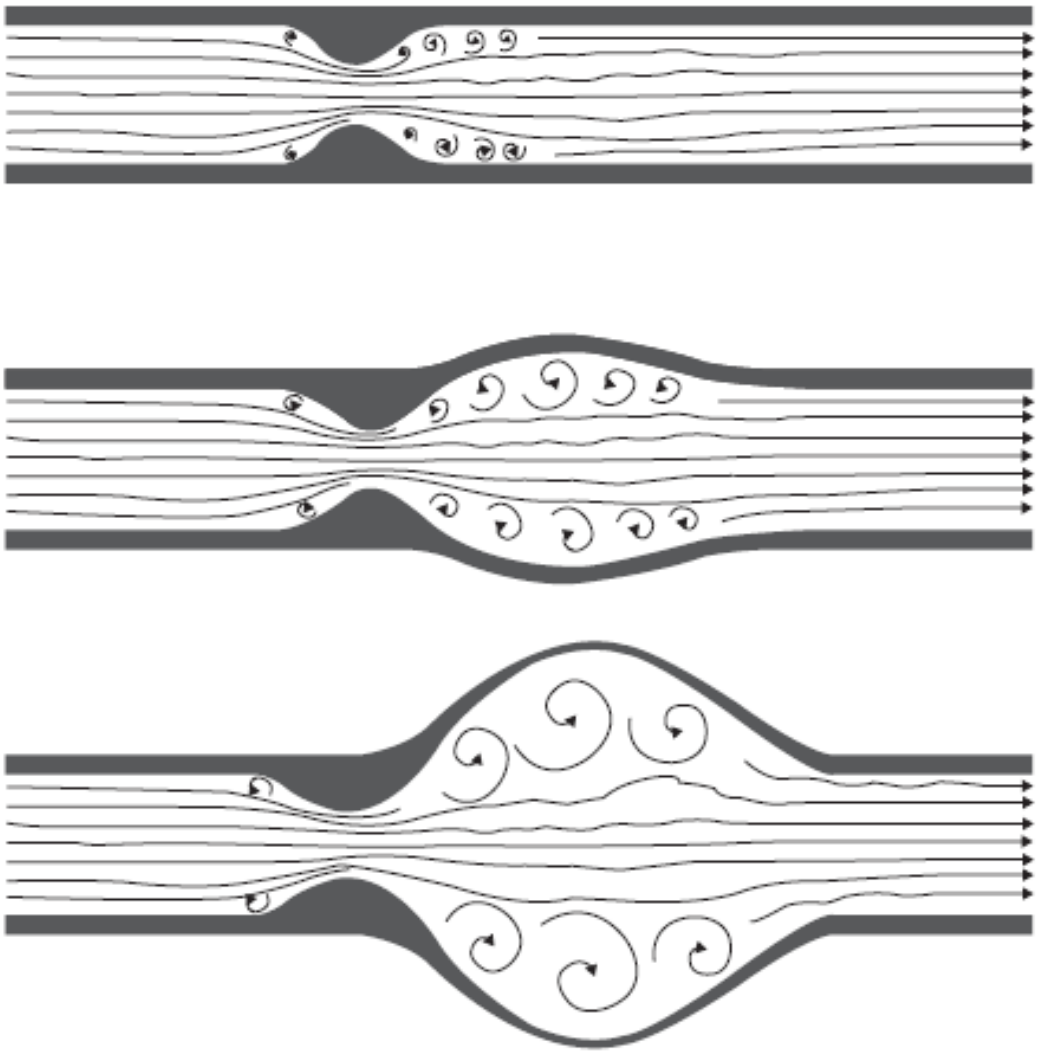

Figure 9 - Post-stenosis dilatation of the artery[79]

1.7 – Finite element method

Systems of differential equations model all the physical phenomena[80]. These systems are very hard or most of the times impossible to solve analytically, so a numerical approach is generally the best solution. The finite element method allows for a finite division of the control volume into n control volumes that are small enough to be considered infinitesimal. The equations defining the fluid properties will be solved for each control volume and integrated along the studied geometry. The network of finite elements is called mesh, and it is generally assumed that the variables vary in a linear manner over each element[81]. Given certain initial values and boundary conditions, the differential equations governing the system are individually calculated for each element and then patched together for the overall geometry following certain rules.

The mesh sizing is critical for several reasons. On the one hand, a coarse mesh might lead to divergence of the solution since the solver might not be able to patch together the individual results for the whole geometry. If convergence of the system were achieved, the result could be inaccurate, with low spatial resolution so eventually useless for the engineer. On the other hand, over-meshing the geometry would exponentially increase the calculation times for two reasons. First, the solver would require more time since it has more control volumes to calculate yet more equations to solve. Second, the time increment for each iteration would have to be reduced in order to converge a solution. Time increment is the other critical parameter in simulations using the finite element method. Again, a compromise between accuracy of the solution and resources requirement is necessary. Large increment times will result in divergence of the computation but tiny increments will make the computation too long, and might at the same time, in certain geometries, affect the stability of the initial steps of the calculation, leading again to a loss of convergence.

Two different iterative integration schemes are used to solve any finite element method problem. One scheme involves the calculation of the properties of each element and the other one involves the congruence of the whole system. The Navier-Stokes system of equations is solved for every element using a monolithic implicit solver. Once every element is solved, the system of equations with all the particular solutions is solved together using a numerical method to solve partial differential equations. The two most common methods to solve these systems are Backward-Euler method (1.6.1) and Crank-Nicolson method[81] (1.6.2).

$$\frac{u_i^{n+1} - u_i^n}{\Delta t} = F_i^{n+1}(u, x, t, \frac{\partial u}{\partial x}, \frac{\delta u^2}{\delta x^2})$$

Equation 13 - Backward-Euler method

$$\frac{u_i^{n+1} - u_i^n}{\Delta t} = \frac{1}{2}(F_i^{n+1}\left(u, x, t, \frac{\partial u}{\partial x}, \frac{\delta u^2}{\delta x^2}\right) + F_i^n\left(u, x, t, \frac{\partial u}{\partial x}, \frac{\delta u^2}{\delta x^2}\right))$$

Equation 14 - Crank-Nicolson method

The software used to import geometries, mesh them and simulate fluid dynamics and mass transfer is the CompassFem v12.1.2 that includes the pre and post-processor GID and the CFD module Tdyn® [82]. GID is able to create geometries or preferably import them from several file formats. It is preferable to import these geometries in format IGES when created with CATIA®. GID also allows setting the boundary conditions of the problem in a user-friendly manner. Tdyn calculates the solutions and GID reads the solutions file and presents the results in the post-process module.

1.8 – Hypothesis and objectives

The phenotype of vascular cells is strongly linked to flow characteristics inside blood vessels. In parallel, hemodynamics and flow patterns depend upon the geometry of blood vessels and biochemical characteristics of blood, which are unique for every patient. This biochemical and physical milieu is particularly critical in patients undergoing percutaneous vascular interventions.

This thesis hypothesizes that there is a quantifiable correlation between geometry-imposed flow disruptions and inflammatory and thrombogenic phenotype in vascular cells. Furthermore, this thesis aims to understand some of the mechanisms by which stents, the state-of-the-art solution to atherosclerosis, keep hampering vascular health by increasing the risk of thrombosis, in particular in stents carrying anti-proliferative drugs and in patients with chronic renal failure. To verify these hypothesis, the objectives are:

1. Developing an *in silico* framework that enables reproducing any bifurcated artery from patient data to:
    a. Simulate blood flow.
    b. Localize and quantify geometry-dependent flow disruptions.
    c. Track soluble tissue factor traffic along the walls of the studied bifurcations.
    d. Manufacture vessel-like polymeric scaffolds that mimic geometries of interest.
2. Applying the vessel-like polymeric scaffolds to study, *in vitro*, the correlation between:
    a. Flow disruptions and atherosclerotic progression biomarkers in vascular cells.
    b. Inflammatory milieu and atherosclerotic progression biomarkers in vascular cells.
    c. Flow disruptions and thrombosis biomarkers in vascular cells.
    d. Sirolimus and tissue factor expression in vascular cells.
    e. Uremic serum and solutes and tissue factor expression in smooth muscle cells.

2 – ARTERIAL REPLICATION PLATFORM AND COMPUTATIONAL MODELING

A Visual Basic® 2010-based engineered arterial model provides a personalized platform for cardiovascular architecture and lesion morphology. Three-dimensional images of patient arterial structures are reproduced using CATIA®, a computer aided design (CAD) commercial software, and saved as IGS, CAM or STL files, providing the precise coordinates of a given arterial bifurcation. CAM image files are used to create Teflon® molds to manufacture polydimethylsiloxane (PDMS) scaffolds that mimic the specific vascular bed. The PDMS scaffolds are coated with fibronectin as extracellular matrix protein and subsequently, layer-by-layer assembled with all three cellular components of the arterial wall: fibroblasts, smooth muscle cells, and endothelial cells. Using the STL files, a support is 3D printed so the PDMS scaffolds may be fit in their tridimensional physiological position and the full architecture of the vessel recapitulated. Tdyn®, a commercial computational fluid flow simulator imports the IGS files, and performs CFD simulations to predict the map of velocities and shear stresses along the bifurcations.

2.1 – Visual Basic Interface

The original C code from Kolachalama[83] was created to run only simulation using Gambit® meshing software. The code was initially adapted to a Visual Basic® 2008 formulary[84]. It was expanded (Figure 10) in order to incorporate the vessel's curvature both for the simulations and for the physical bench model. It also incorporated the option to evaluate the amount of recirculation for each region of the bifurcation, to save the current geometry or to load previous models.

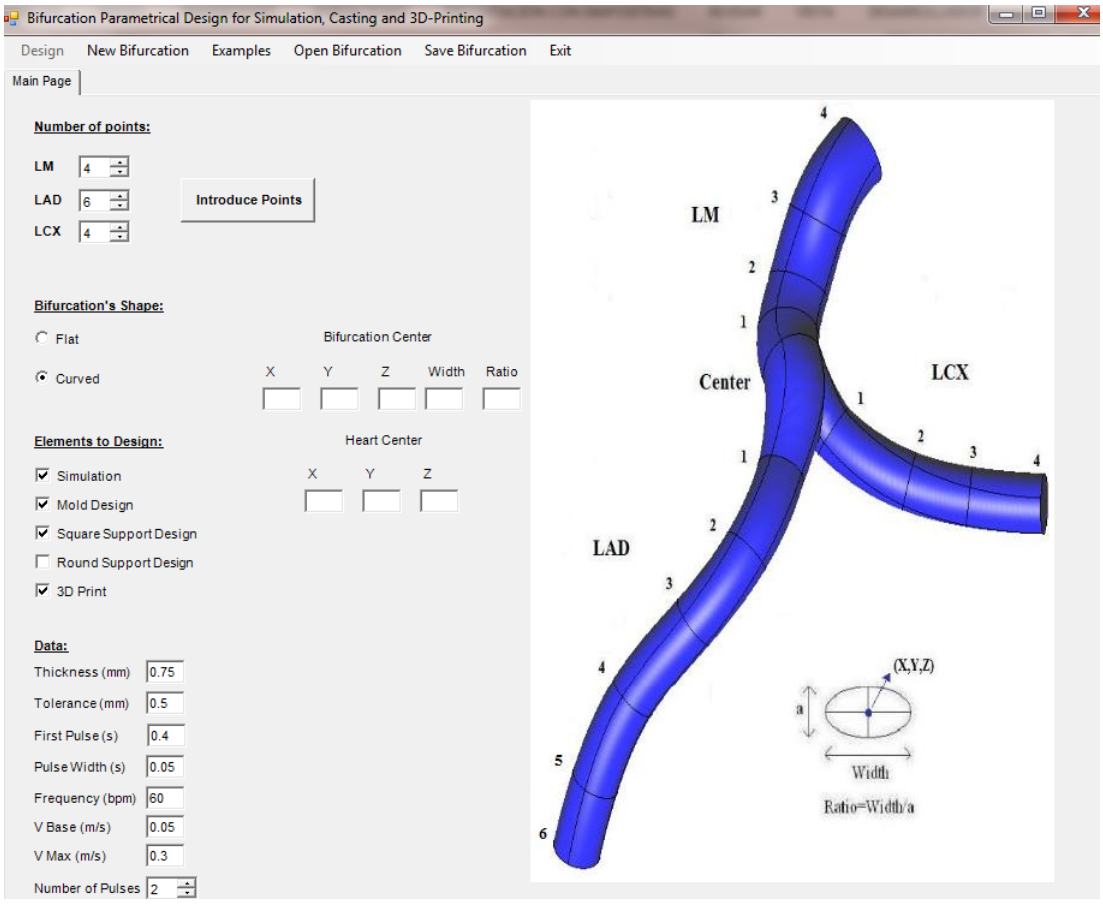

Figure 10 - Visual Basic 2010 interface

The program worked for four different applications: CFD, mold design, vessel's 3D-print and support 3D-print. The applications shared the exact same dimensions, obtained through 2D angiography, Doppler echography, 3D MRI or 3D Laser Scanning and identified by physicians or pathologists as regions of interest for assessment of risk. Two models of bifurcations were analyzed, the carotid artery bifurcation and the left main coronary artery. The carotid model accounted for the division of the central carotid artery (CCA) into the internal carotid artery (ICA) and the external carotid artery (ECA). The coronary model described the left main coronary artery (LM) dividing into the left anterior descending artery (LAD) and the left circumflex artery (LCX).

For the carotid artery, the data from Kolachalama[83] were used, but the data obtained at the ICC Sant Pau of Barcelona using Eco-Doppler (Figure 11) could also have been applied. For the coronary artery, coronary geometries from angiograms of ten different patients at risk of cardiovascular disease recruited at the Cardiovascular Section of St. Elizabeth's Hospital (Boston, MA) were retrieved. The protocol was approved by the Institutional Review Board of Tufts University Medical Center. Informed consent was obtained and patients' names were deleted previous to the 3D reconstruction. An average of the patients' data was used to design an idealized left coronary bifurcation. In addition, two swine hearts (Figure 12) were scanned using a Roland Active Piezo Sensor 3D laser scanner and their coordinates were used to establish the curvature of the bifurcation.

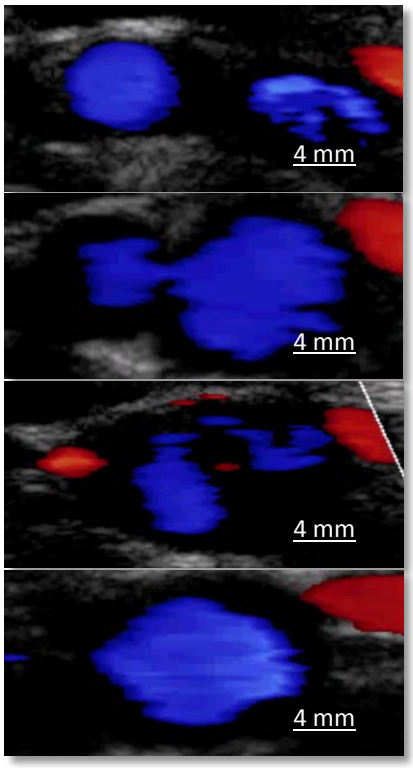

Figure 11 - Doppler echography of a carotid artery

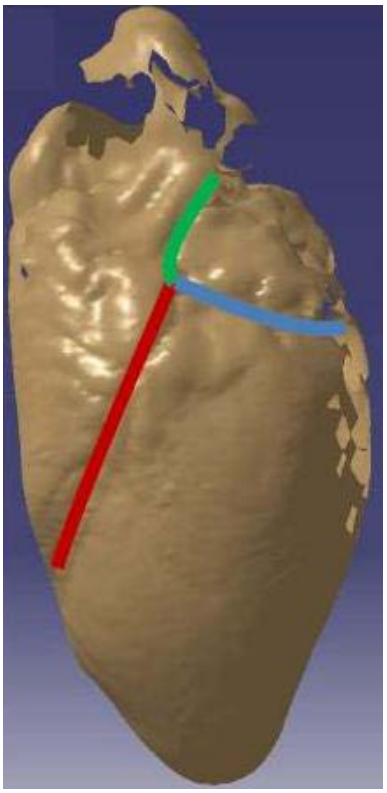

Figure 12 - Reconstruction of a swine heart and outline of the artery of interest

The interface encoded up to four different macro files for CATIA®, which produced IGES, STL and CAM files. Each file was used for a different aspect of reconstruction. The IGES file (Figure 13) was the bridge to CFD simulations in Tdyn®. CAM files (Figure 14) drove the computer numerical control mechanization of Teflon® molds that would lead to the fabrication of PDMS scaffolds. STL files allowed for 3D printing of the selected arterial architecture as a flexible polymeric structure (Figure 15) and their curved polycarbonate support that mimicked the contour established by the underlying myocardium (Figure 16).

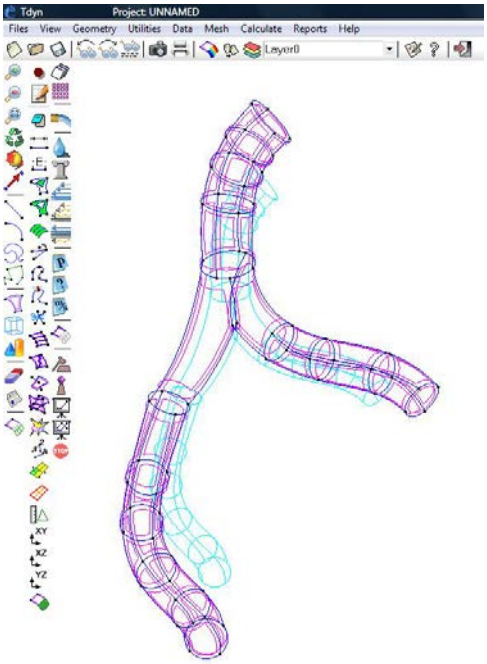

Figure 13 - IGES file for CFD

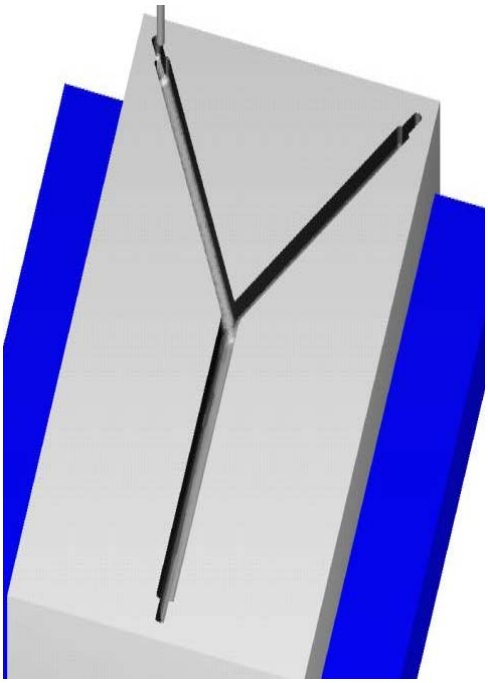

Figure 14 - CAM file for Teflon® machining

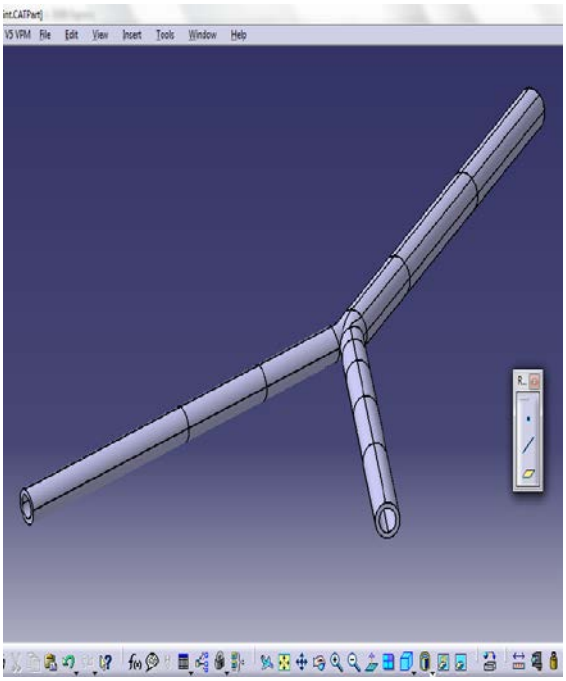

Figure 15 - STL file for arterial 3D printing

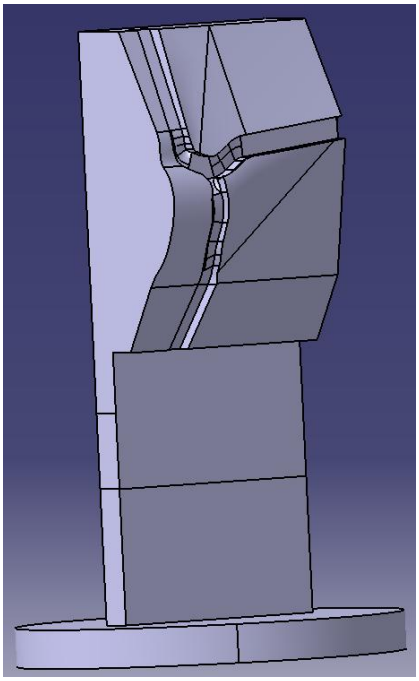

Figure 16 - STL file for support 3D printing

2.2 – Computational fluid dynamics

Blood flow simulations were performed in order to study the physical effects of different critical parameters of the most relevant arterial bifurcations. The tangential velocity (vTan) was the local variable defined to measure the velocity of the fluid flow. The orientation of each node of the mesh was determined by the spline (Figure 17) that generated the arterial branch. vTan (Figure 18) was calculated as the dot product of its local velocity vector and the direction imposed by the spline. This strategy is optimal in curved geometries such as those seen in the coronary arteries since it always accounts for local recirculation. CFD calculations predicted recirculation downstream of bifurcation and the platform calculated NVV (Equation 18) to quantify local recirculation for each branch. In further *in vitro* experiments described in section 3.2, NVV was the metric found to better correlate flow recirculations with Ox-LDL uptake. Other parameters such as the total volume of recirculation (VolRec) and the percentage of volume of recirculation (%VolRec) at the peak of recirculation and their integrals along the pulse (Int VolRec, Int %VolRec) correlated worse than NVV. Furthermore, the residence time of a particle in a recirculating streamline and the minimal tangential velocity on each branch correlated even worse (Figure 19).

By coupling the mass transfer module to the flow dynamics module in Tdyn®, the soluble Tissue Factor (sTF) distribution was tracked along the arteries. A stent placed in the vicinity of the vertex of each bifurcation separation was simulated. The initial data for sTF concentrations was given by the experiment in chapter 4.1.2. The adimensional approach to increase the time of experiment is described in chapter 5.9, along with the general equations and particular conditions used to resolve the mass transfer problem.

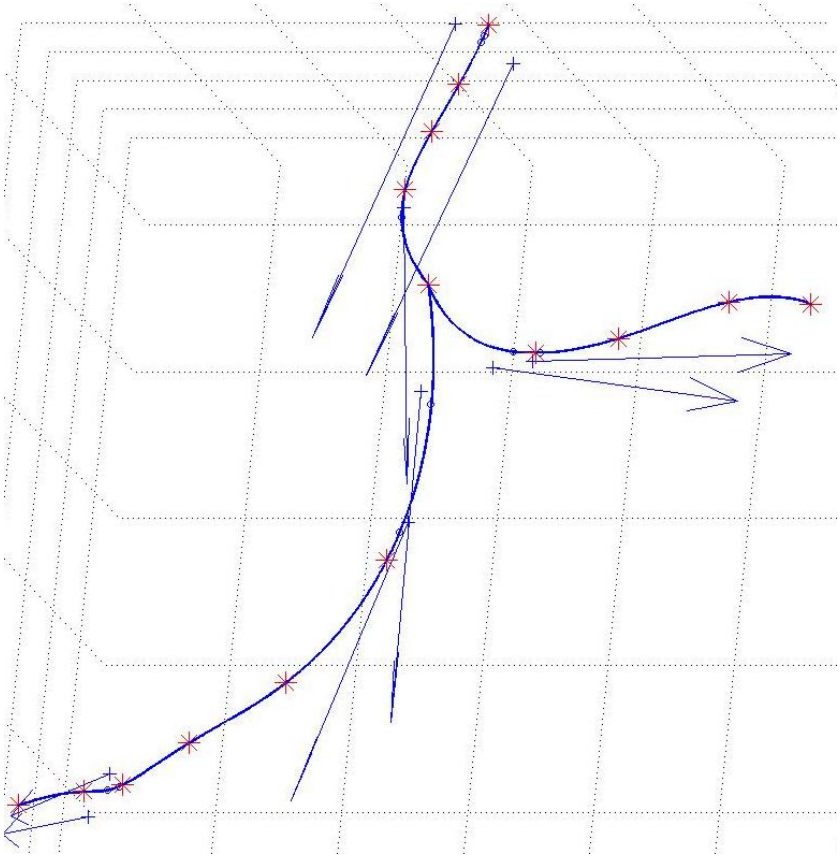

Figure 17 - Splines that generated the arterial branch

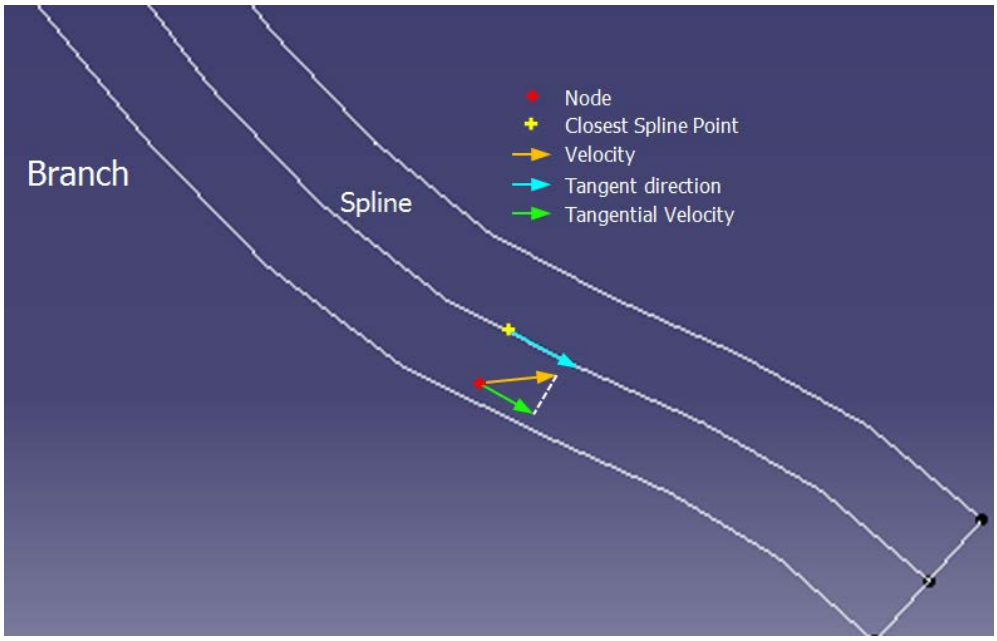

Figure 18 - Tangential velocity (vTan) calculation scheme

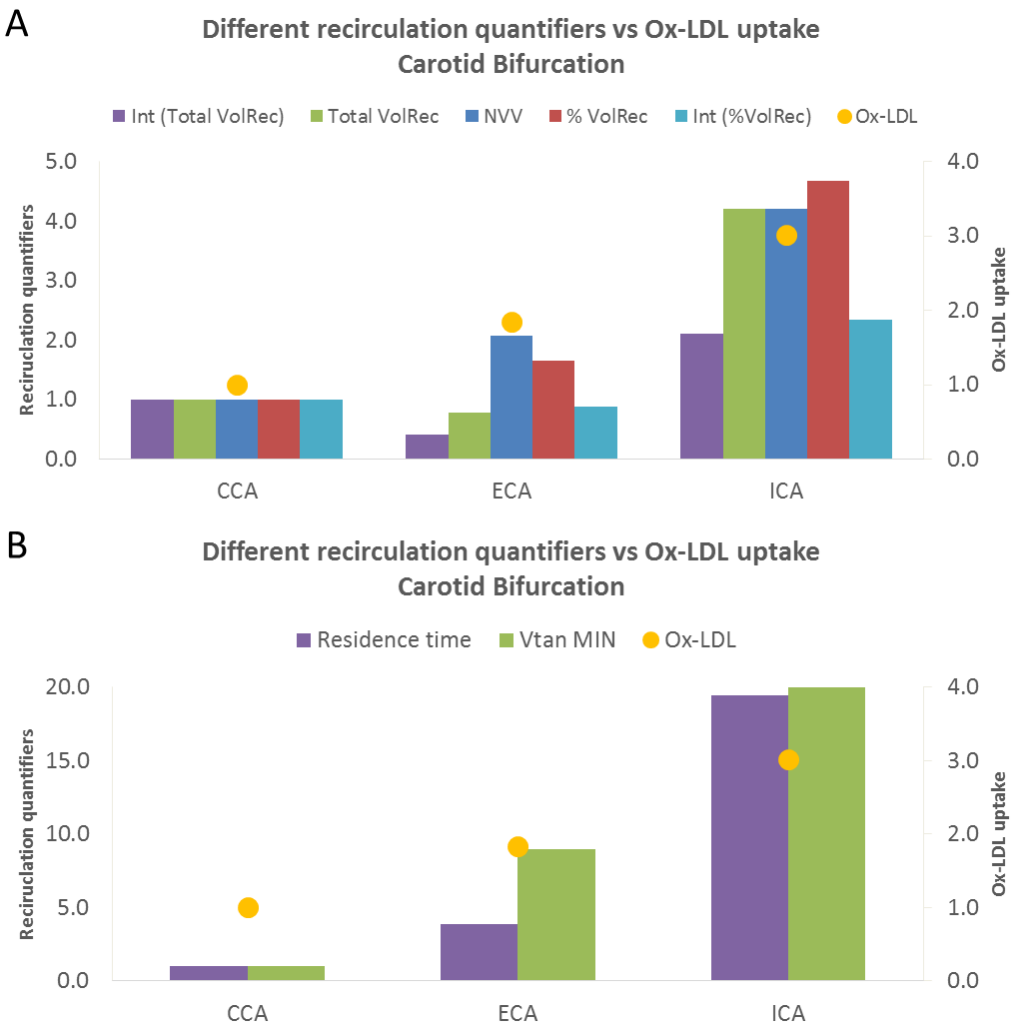

Figure 19 - Correlation between Ox-LDL uptake by EC and different recirculation quantifiers

2.2.1 – Carotid artery

The carotid artery is an excellent model of an arterial bifurcation with recirculation areas. The CCA bifurcates into the ECA and the ICA, irrigating the brain and all the organs above the neck (Figure 20 and Figure 21). Naturally, this bifurcation has certain areas of recirculation that increase with age and trigger plaque deposition. The fracture of an unstable plaque can lead to an ictus, which is the clotting of a capillary inside the brain, leading to a possible death or apoplexy. Also, significant plaque formation within the carotid restricts flow to the brain causing symptoms like dizziness, drowsiness, loss of balance. These symptoms occur generally in the elderly due to long-term plaque accumulation, but the death rate is significantly lower than that attributed to coronary artery disease.

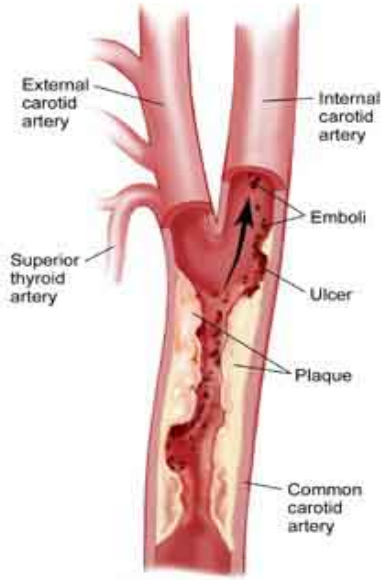

Figure 20 - Carotid bifurcation representation[85]

Figure 21 - Dissected swine carotid bifurcation

The author's blood flow velocity profiles were measured using Doppler echography (Figure 22) and adjusted to a pulse following a Gaussian distribution (Figure 23). One can observe a good adjustment for the first peak and the omission of the second peak in the model. This second peak is a very mild asymptomatic carotid murmur[86], and it was decided that only the ideal healthy situation would be simulated.

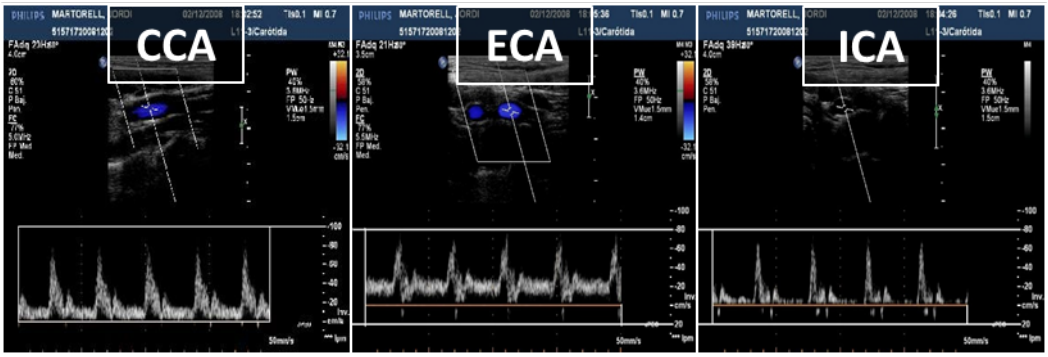

Figure 22 - Velocity profiles in the carotid bifurcation using Doppler echography

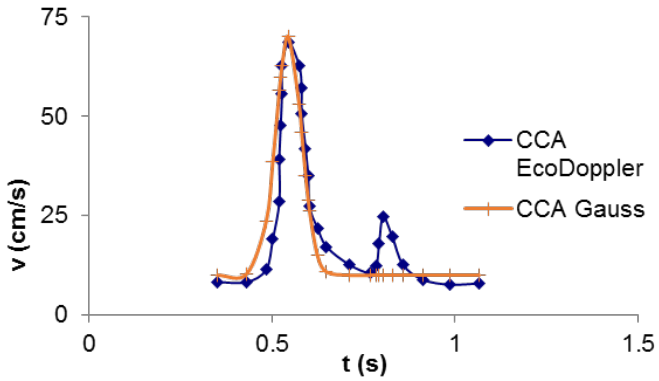

Figure 23 - Comparison between Doppler echography data and the Gaussian adjustment in the CCA

The inlet velocity profile followed the Gaussian approximation to the real profile: a parabolic flow (Equation 16) with a base velocity of 0.1 m/s, a maximal velocity of 0.7 m/s, a Gaussian pulse width of 0.05 s and frequency of 60 bpm. The mesh density is shown in Figure 129 and the CFD conditions are detailed in Table 4 and Table 5. The recirculation quantification methodology is described in chapter 5.9. Recirculation was observed in the two derivative branches of the carotid artery (Figure 24 and Figure 25), with severe recirculations in the ICA ($vTan_{MIN}$ = -190 mm/s) and mild recirculations in the ECA ($vTan_{MIN}$ = -95 mm/s). The amount of recirculation in each branch followed a similar trend (Figure 26). These disrupted flow regimes should affect thrombosis and atherosclerosis biomarkers levels. Hence, the sTF distribution from a stented region was simulated 30 minutes after stent implantation (Figure 27 and Figure 28). The sTF concentration in the vicinity of the arterial wall (stationary sTF) in the recirculating regions of the ICA and the ECA increased up to 53% when compared to the initial values. Flow elutes the sTF from the injured area and redistributes it along the artery. Most of the protein gets washed off downstream the circulatory system, but stationary sTF can signal apoptosis[87], or contrarily promote proliferation[88], enhance inflammation[89] and in any case becomes coagulant in the presence of phospholipids[90].

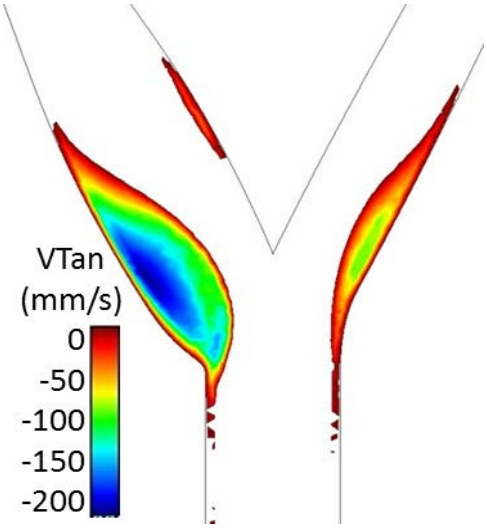

Figure 24 - Recirculation after forward pulse in the carotid bifurcation

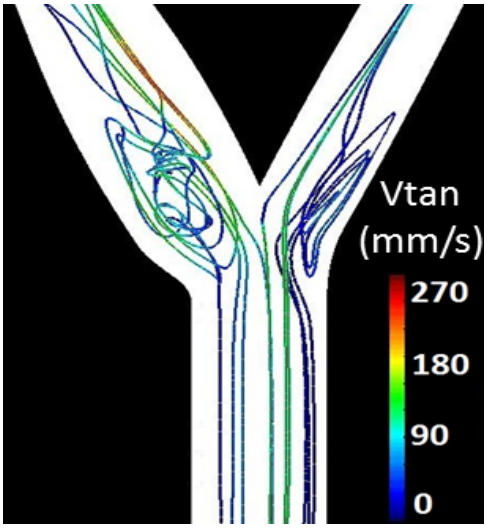

Figure 25 - Streamlines in the carotid bifurcation

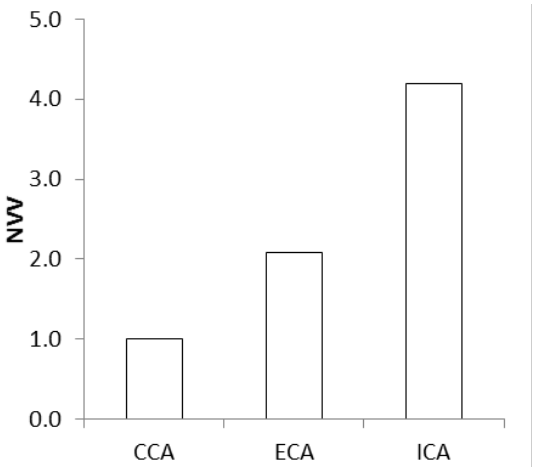

Figure 26 - Recirculation quantification in the carotid bifurcation

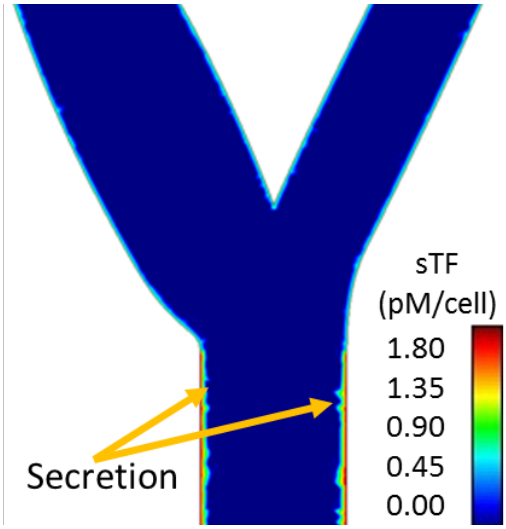

Figure 27 - sTF distribution at time 0 in the carotid bifurcation

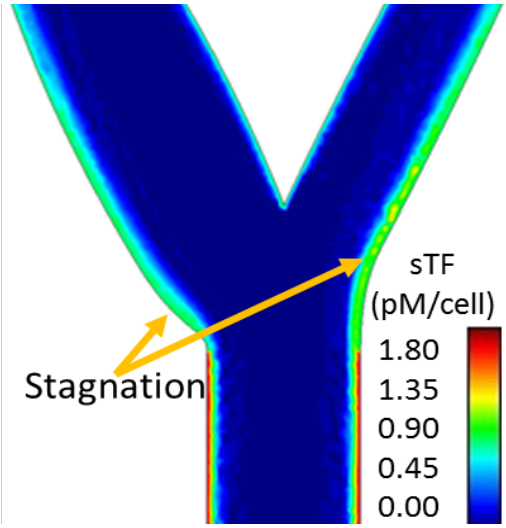

Figure 28 - sTF distribution after 30 minutes in the carotid bifurcation

2.2.2 – Coronary Arteries

Coronary arterial bifurcations (Figure 29) are the vessels where fatty plaque genesis is accompanied with the highest risk of death; disease on those vessels leads to malfunction of the heart. More than 70% of coronary stents are placed within those vessels[91], with the left coronary artery vascular tree being the one more prone to suffer cardiovascular diseases[92]. The LM bifurcation (Figure 30 and Figure 31) is the bifurcation studied in this thesis.

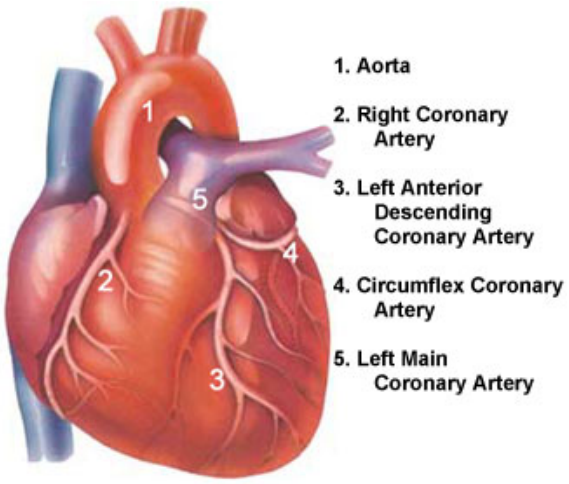

Figure 29 - Coronary arteries representation[93]

Figure 30 - Angiogram of a human LM bifurcation

Figure 31 - Dissection of a swine LM bifurcation

The bifurcation LM-LAD-LCX was simulated in healthy and diseased conditions, flat and with a curvature mimicking the underlying pericardium. The mesh density is shown in Figure 130 and Figure 131 and the CFD conditions are detailed in Table 6, Table 7, Table 8 and Table 9. The inlet velocity profile followed the Gaussian approximation shown in chapter 2.2.1. In the healthy scenario, a parabolic inlet (Equation 16) with base velocity of 0.05 m/s, a maximal velocity of 0.35 m/s, a pulse width of 0.05 s and frequency of 60 bpm[94] were taken as input values. The disease case simulated stenosis[95] before the LM with a corresponding maximal velocity at the inlet of 0.9 m/s. The recirculation quantification methodology is described in chapter 5.9.

2.2.2.1 – Flat bifurcation

The healthy case did not show relevant recirculations. In the diseased case, recirculation was observed in the two derivative branches of the coronary artery (Figure 32 and Figure 33), with mild recirculations in the LAD ($vTan_{MIN}$ = -66 mm/s) and the LCX ($vTan_{MIN}$ = -62 mm/s). The amount of recirculation in each branch followed a similar trend (Figure 34). These mildly disrupted flow regimes might affect thrombosis and atherosclerosis biomarkers levels. Hence, the sTF distribution from a stented region was simulated 30 minutes after stent implantation (Figure 35 and Figure 36). sTF concentration increased an 18% in the proximity of the walls of the LAD and the LCX when compared to the initial values. Similarly to the carotid example but to a lesser extent, flow drags sTF from the injured area and redistributes it along the artery walls and downstream the circulatory system. The stationary sTF in the recirculation zone signals vascular injury up to 2 cm away from the injured region.

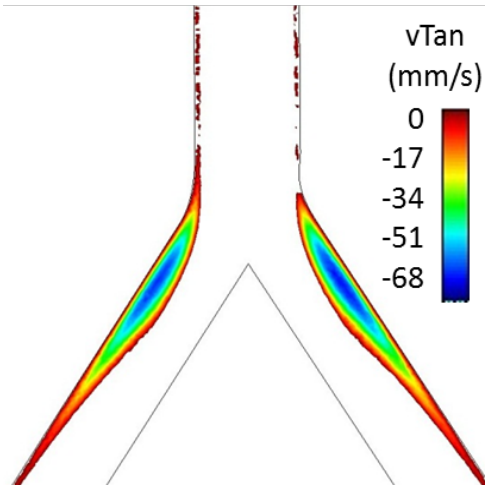

Figure 32 - Recirculation after forward pulse in the idealized coronary bifurcation

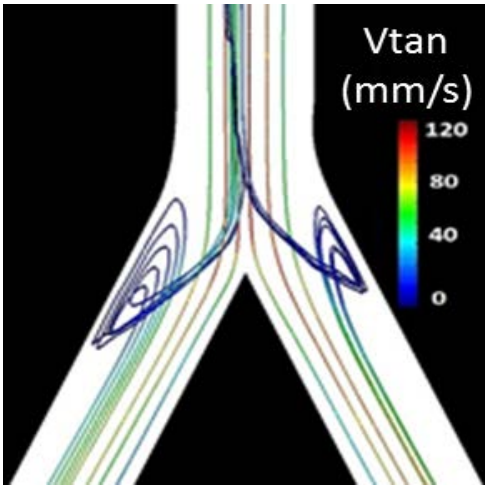

Figure 33 - Streamlines in the idealized coronary bifurcation

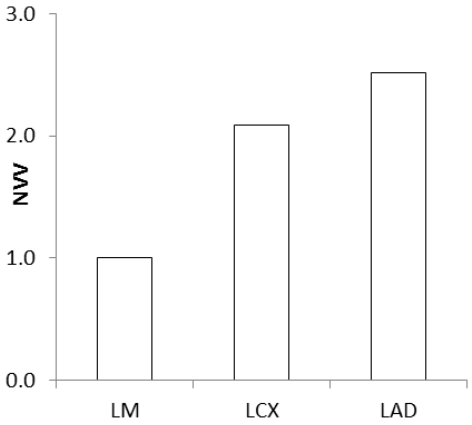

Figure 34 - Recirculation quantification in the flat, diseased coronary bifurcation

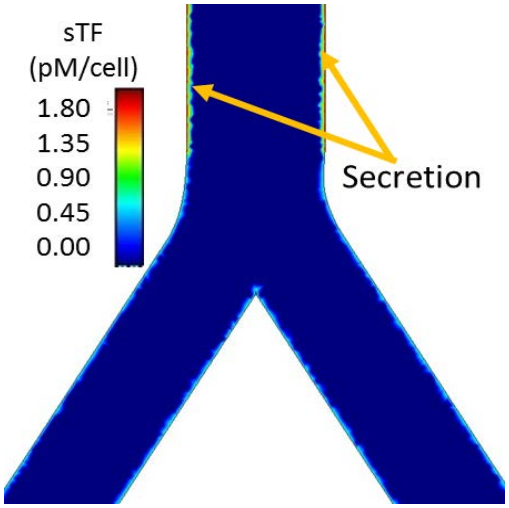

Figure 35 - sTF distribution at time 0 in the idealized coronary bifurcation

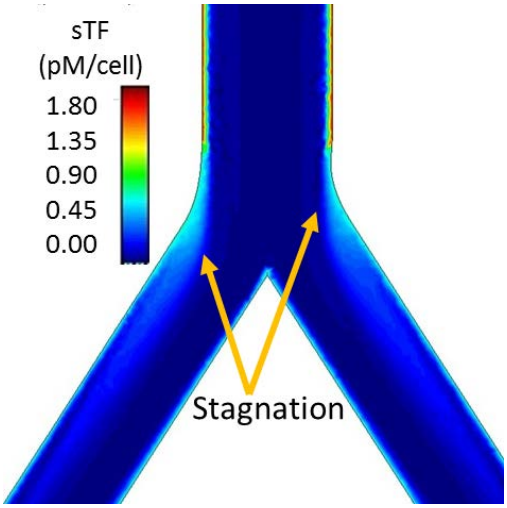

Figure 36 - sTF distribution after 30 minutes in the idealized coronary bifurcation

2.2.2.2 – Curved bifurcation

The healthy case did not show relevant recirculations. In the diseased case, recirculation was observed in the two derivative branches of the coronary artery, but also in the main branch, especially very close to the separation area (Figure 37 and Figure 38) with mild recirculations in the LAD ($vTan_{MIN}$ = -18 mm/s) and negligible recirculations in the LCX ($vTan_{MIN}$ = -6 mm/s). The amount of recirculation in each branch followed a similar trend (Figure 39). These mildly disrupted flow regimes might affect thrombosis and atherosclerosis biomarkers levels. The sTF distribution was not studied in that particular case.

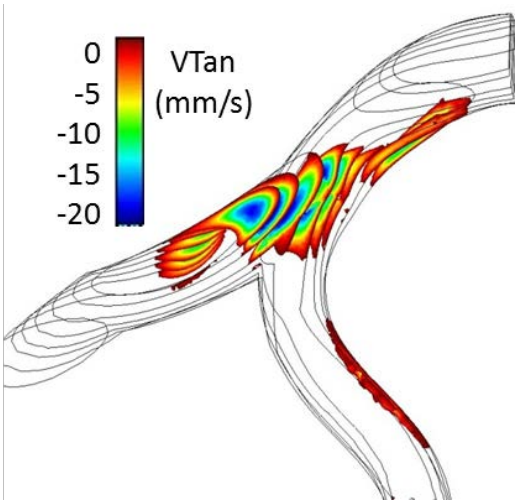

Figure 37 - Recirculation after forward pulse in the curved, diseased, coronary bifurcation

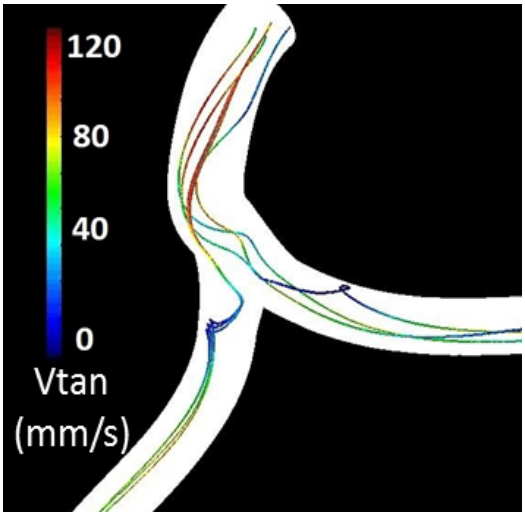

Figure 38 - Streamlines in the curved, diseased, coronary bifurcation

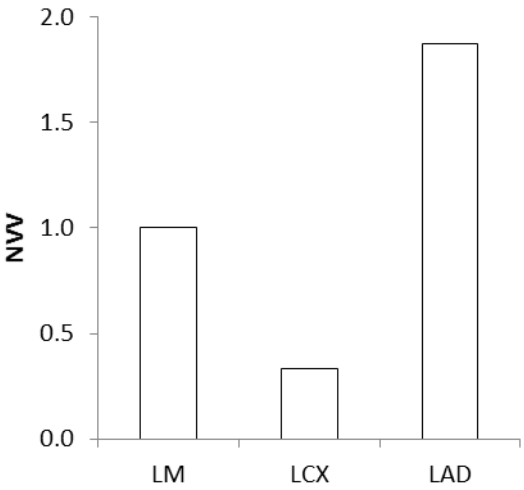

Figure 39 - Recirculation quantification in the curved, diseased coronary bifurcation

2.3 – Vessel-like scaffolds

The platform was designed to correlate the flow patterns observed in the CFD simulations with expression of cardiovascular disease biomarkers along arterial bifurcations. Hence, an automated, reproducible and time-effective method to reproduce physiologically realistic geometries had to be developed. The Visual Basic® 2010 interface compiled computer numerical control (CNC) files that allowed the manufacture of Teflon® molds to achieve PDMS polymerization on their surface. PDMS is a cheap, friendly and biologically inert material that polymerizes in a wide range of conditions so it was a potential candidate as polymeric material to manufacture the scaffolds. On the other hand, the 3D-Print module generated STL files that could directly print the scaffold using photo-polymeric layer-by-layer techniques. Those scaffolds would eventually be seeded with vascular cells and be connected to a perfusion bioreactor.

2.3.1 – PDMS (Teflon® molds, polyurethane molds and soluble wax core)

In a first step, two positive Teflon® molds (Figure 40) of the bifurcation were machined using a CNC machine Fagor® 8055. Consequently, liquid polyurethane (PU) was poured on the top of the two molds to obtain two flexible negative molds after 16 hours curing. The PU molds (Figure 42) were assembled to create a cavity identical to the desired bifurcation. A pre-warmed (70^0C) optical soluble wax was injected through the cavity and cooled down until room temperature to obtain the solid core that would allow generation of the bifurcation lumen. To polymerize PDMS from its liquid form, parts A (monomer) and B (curing agent) of Dow Corning® Sylgard 164 Silicone Elastomer Kit were mixed in a 10:1 relation and degassed using vacuum. The degassed mixture was poured on a negative Teflon® mold that was already holding the inner wax cast (Figure 41). The PDMS slowly polymerized following both the core and the mold shape. Finally, the solid wax core was dissolved in hot water (80^0C) for 2 hours. After 20 minutes cleaning with a 0.2% sodium dodecyl sulfate solution in distilled water and two consecutive rinses with distilled water, the hollow bifurcated scaffold molds (Figure 43) were autoclaved at 120^0C and 2 bar. In the case of curved coronary bifurcations, the PDMS scaffold could be held by the polycarbonate support (Figure 44).

Figure 40 - Positive Teflon® mold

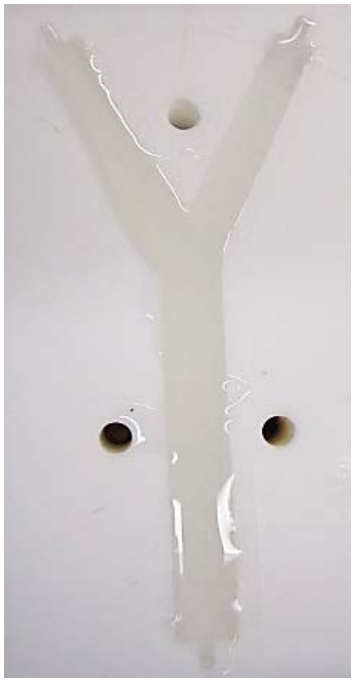

Figure 41 - Negative Teflon® mold with inner cast and liquid PDMS

Figure 42 - PU mold and inner wax cast

Figure 43 - PDMS scaffold of the carotid bifurcation

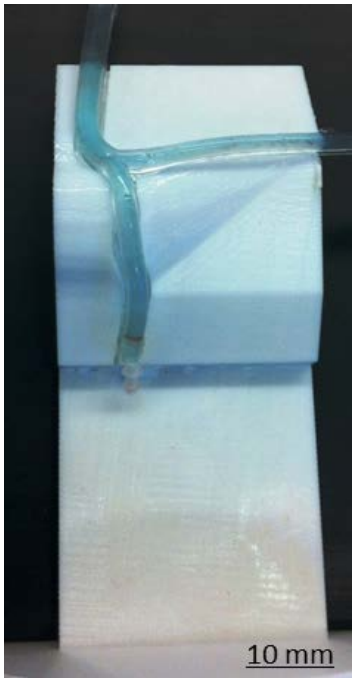

Figure 44 - PDMS scaffold of the coronary bifurcation and its polycarbonate support

Arterial mimics were constructed from human coronary artery endothelial cells (EC) and/or human aortic smooth muscle cells (SMC) under computational guidance built on physiologic geometries and flow patterns. Their integrity, viability and functionality was assessed using immunofluorescence (IF), scanning electron microscopy (SEM) and Hematoxylin & Elastin (H&E) staining. These methods are detailed in chapter 5.5. The constructs were coated with 100 (coronary) to 150µg/ml (carotid) of fibronectin in phosphate buffer saline (PBS) overnight at 4^0C and washed once to remove loosely adsorbed fibronectin. SMC and EC cultures were maintained as detailed in chapter 5.1.3 and sequentially layered as follows. SMC ($1{\cdot}10^6$cells/mL) were seeded first on the fibronectin-coated constructs forming a multi-layer. After 48h adhesion under axial rotation constructs were filled with an EC suspension ($1{\cdot}10^6$cells/mL) and incubated for additional 48h, under identical conditions. Experiments were run 48h after this last seeding step. The trilaminate architecture of the vasculature was attempted, seeding human aortic adventitial fibroblasts (FB) prior to SMC on the fibronectin-coated PDMS constructs. Unfortunately, the FB migrated towards the surface up to the EC level, detaching from the PDMS surface and peeling off the whole tissue. Individual cell types were identified by immunofluorescence (IF). Fibroblasts fluoresced as they were infected with a retrovirus containing an eGFP transgene (Figure 45 A), SMC were confirmed via α-SMC-actin staining (Figure 45 B) and EC were identified using CD31 marking (Figure 45 C). SEM revealed complete cellular coverage along the length and the width of the constructs (Figure 45 D-F) and standard histology confirmed the multilayer structure (Figure 45 G).

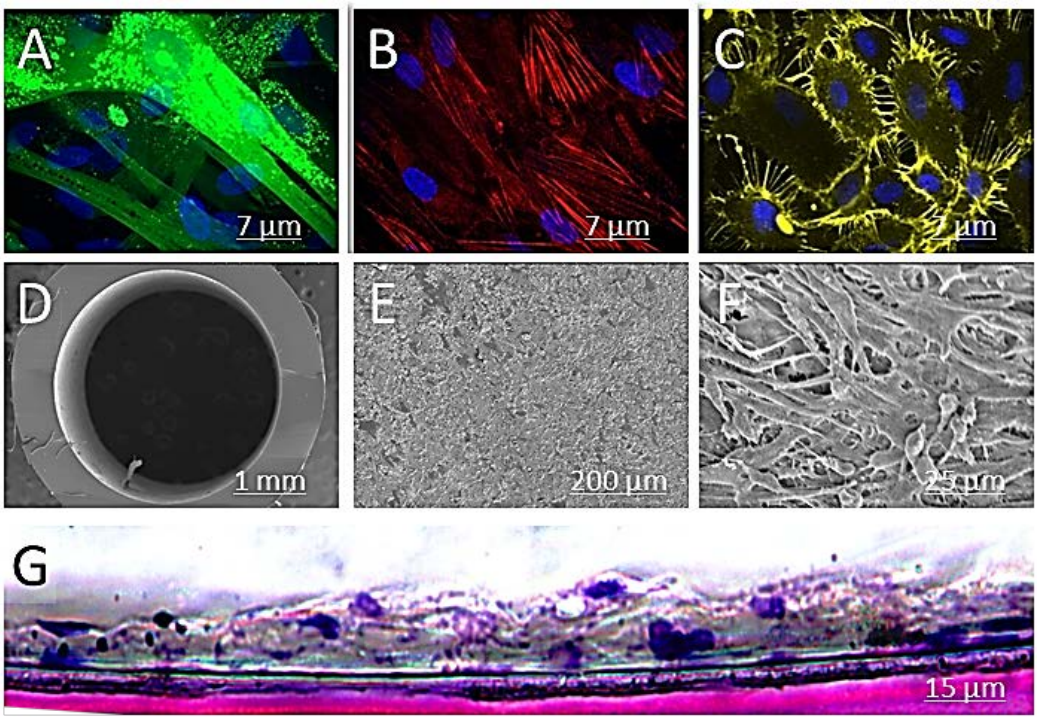

Figure 45 - FB, SMC and EC within PDMS constructs

Functional assays confirmed the biological integrity of each cell type. Fibroblasts functionality was resolved by evaluating the cytoglobin levels in mono- and co-culture with SMC and EC[96]. Cytoglobin levels were stable independent of the adjacent seeding of other cells. SMC should show a proliferative phenotype when depleted of the overlying endothelium, but remain untreated when covered from blood flow by endothelial cells[44]. Indeed, Ki67-positive SMC were 6±1 fold ($p<0.05$) more abundant when cultured alone (Figure 46 A-C) than those co-cultured in a trilaminate fashion (Figure 46 D-F). Basal ICAM-1 levels in EC (Figure 47 A-C) rose 7±1 fold ($p<0.05$) after stimulation with TNF-α (Figure 47 D-F) as expected when subjected to cytokine stimulation[18]. EC (Figure 48 A) and SMC (Figure 48 B) retained their cytoskeletal immunostaining (alpha-tubulin) and alignment with flow.

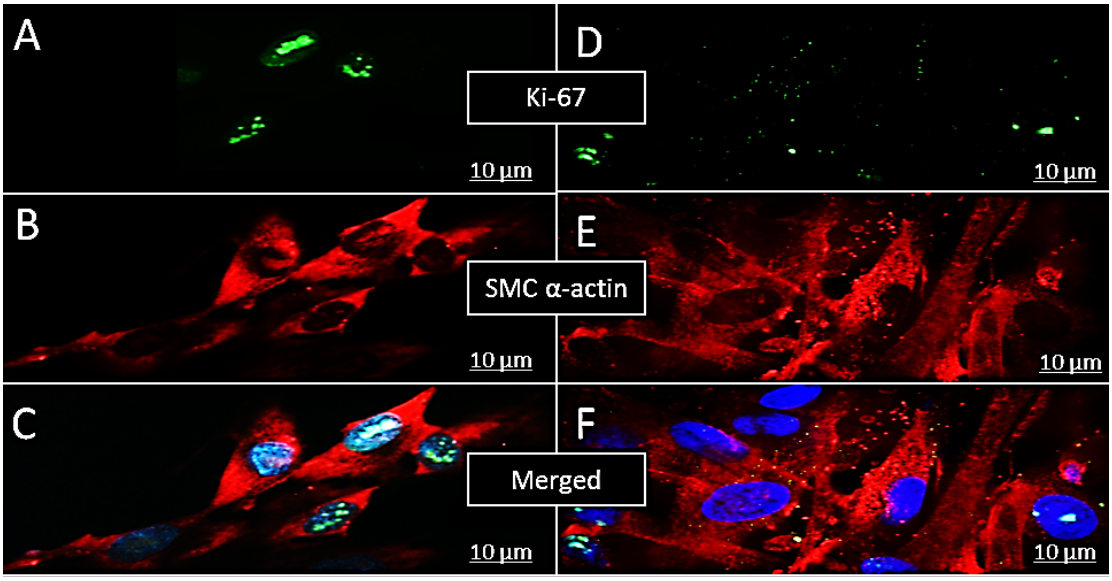

Figure 46 - Ki-67 expression in SMC alone or in trilaminate culture

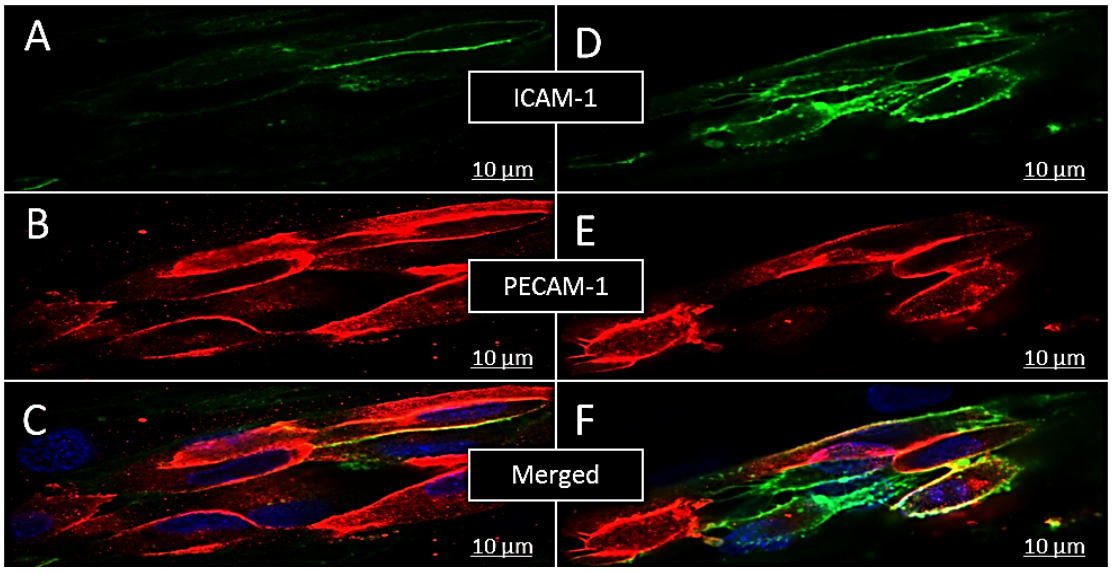

Figure 47 - ICAM-1 expression in EC with (right) or without (left) TNF-α

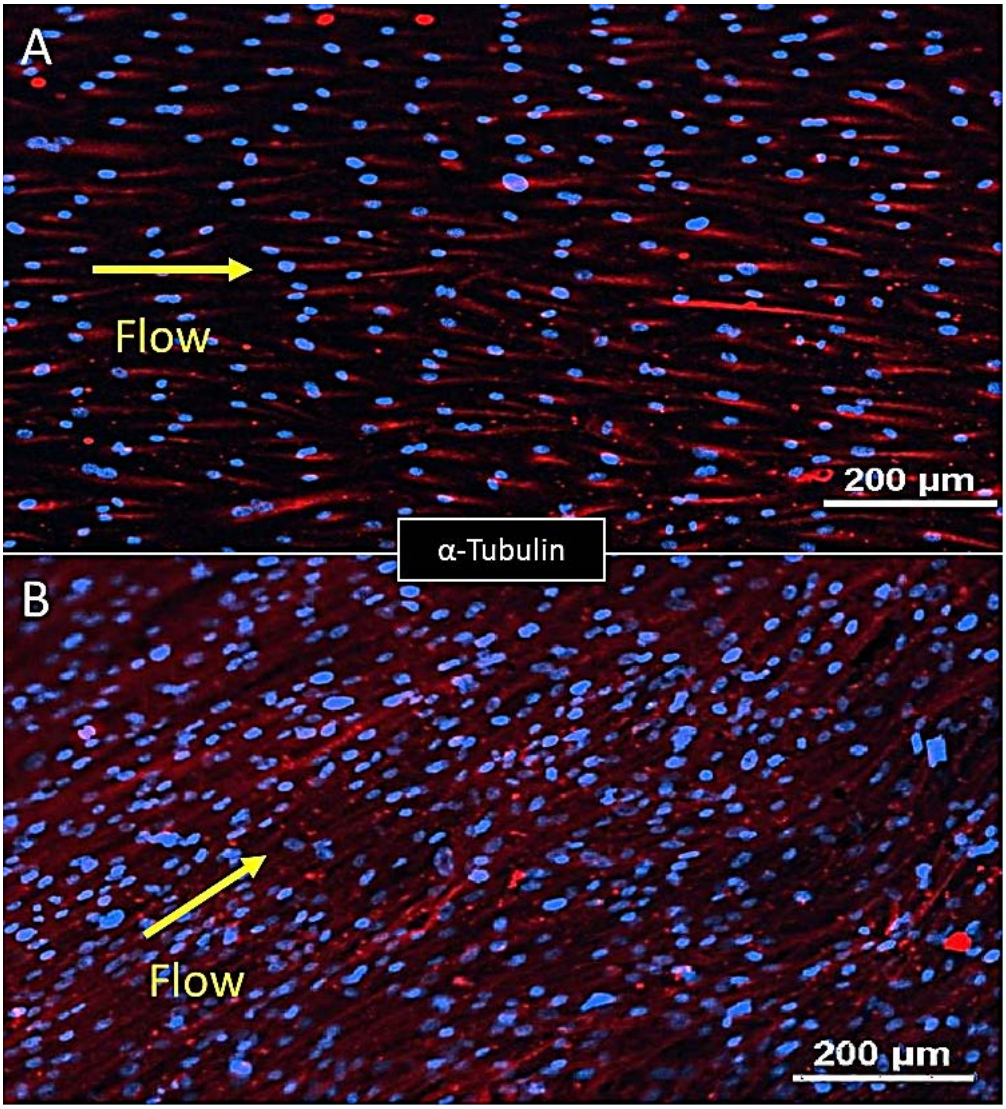

Figure 48 - Flow alignment of EC (A) and SMC (B)

2.3.2 – Photo-polymeric 3D Print

The only method able to generate the scaffold in one piece, without burs and with homogeneous wall thickness was 3D-Printing the scaffold in a polymer. Moreover, this polymer had to be flexible, transparent and more importantly compatible with vascular cells. As described in chapter 5.10.2, a 3D Printer Objet Eden 500V printing with Fullcure 930 Tangoplus polymer was the only possible combination in terms of feasibility and price on one hand, and flexibility and transparency of the material on the other. The resultant 3D-printed arterial bifurcation can be observed in Figure 49.

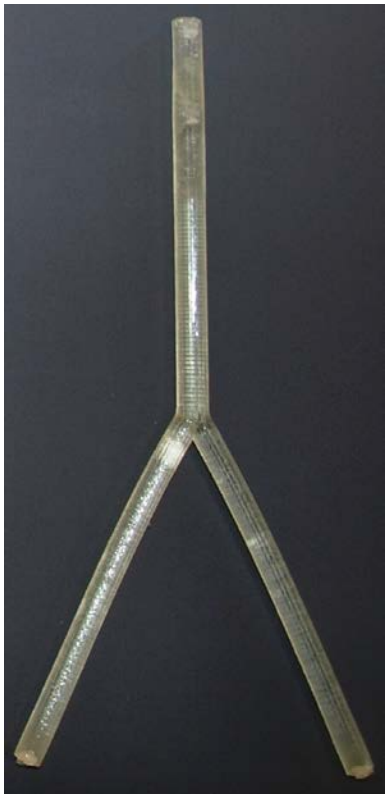

Figure 49 - 3D-Printed scaffold of the LM-LAD-LCX bifurcation

The toxicity of the material was initially evaluated by a live/dead assay of cells seeded in tissue culture plates and placed in contact with the material for 24 hours. The assay revealed a high toxicity of the material if untreated since cell population decreased around 90% (Figure 50).

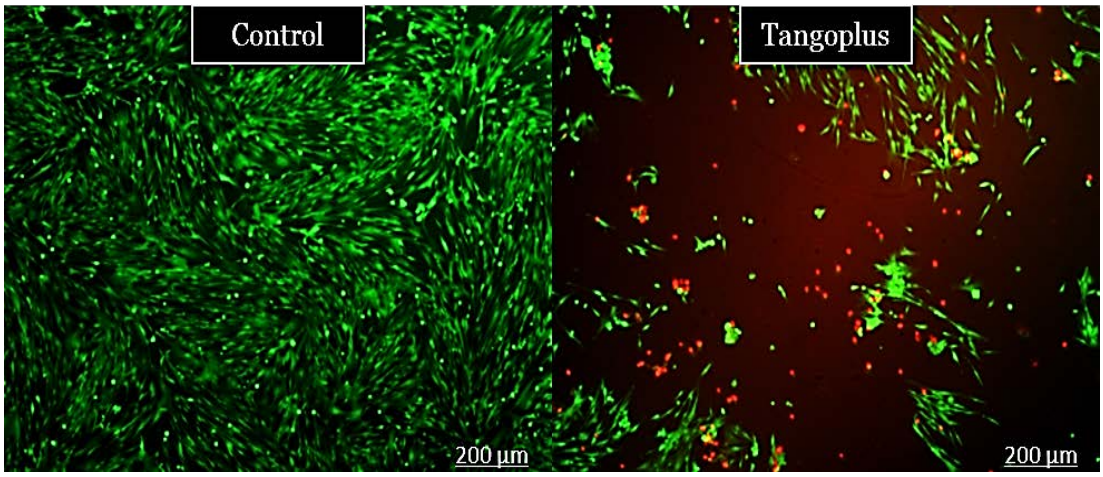

Figure 50 - Toxicity of the untreated 3D material in direct contact with smooth muscle cells

In order to reduce the toxicity of the material, non-polymerized urethane acrylate and methacrylate oligomers (main components of FullCure 930 Tangoplus) were extracted in several solvents. Additionally, the material was exposed overnight to UV to help polymerization of unreacted monomers. Fibroblasts were exposed for 24 hours to medium conditioned with the "clean" material and tested in a live/dead assay. Toluene seemed to properly extract the toxic components as cells properly attached to the material as seen in Figure 51, despite auto-fluorescence of the polymer. Unfortunately, the process weakened the material in a way that it was not flexible nor autoclavable so it could not serve this project's purpose.

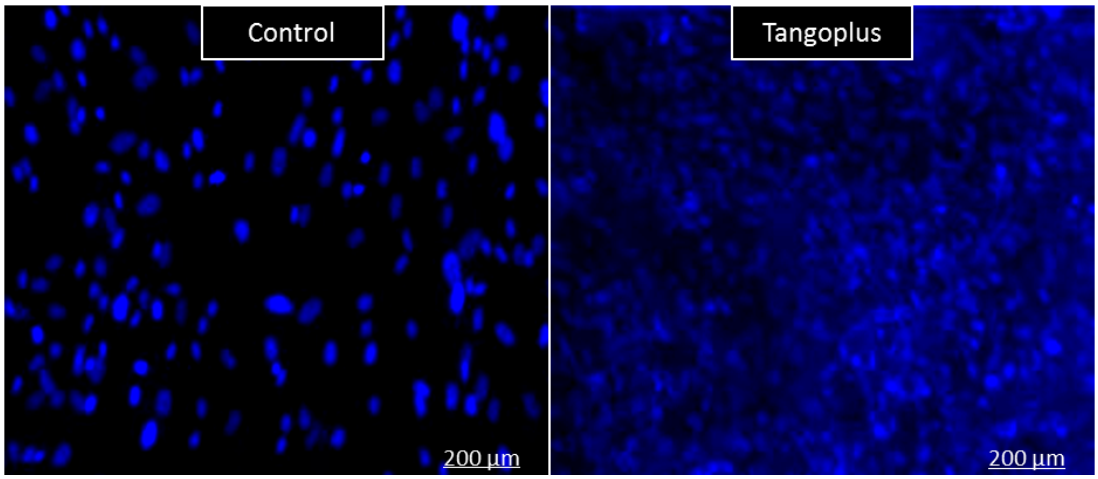

Figure 51 - Toluene extraction allowed fibroblasts (DAPI, blue) attachment

2.3.3 – Collagen-based 3D Print

The Swiss company RegenHu® has developed a 3D printer that allows high precision printing using collagen-based materials. The printer is installed inside a flow chamber so the printing process is already sterile and the material does not require autoclaving. The company was able to accurately print a sample of the coronary bifurcation (Figure 52). Further work would be required to confirm the biocompatibility and utility of the material. This is a first step to implantable arteries based on the platform designed.

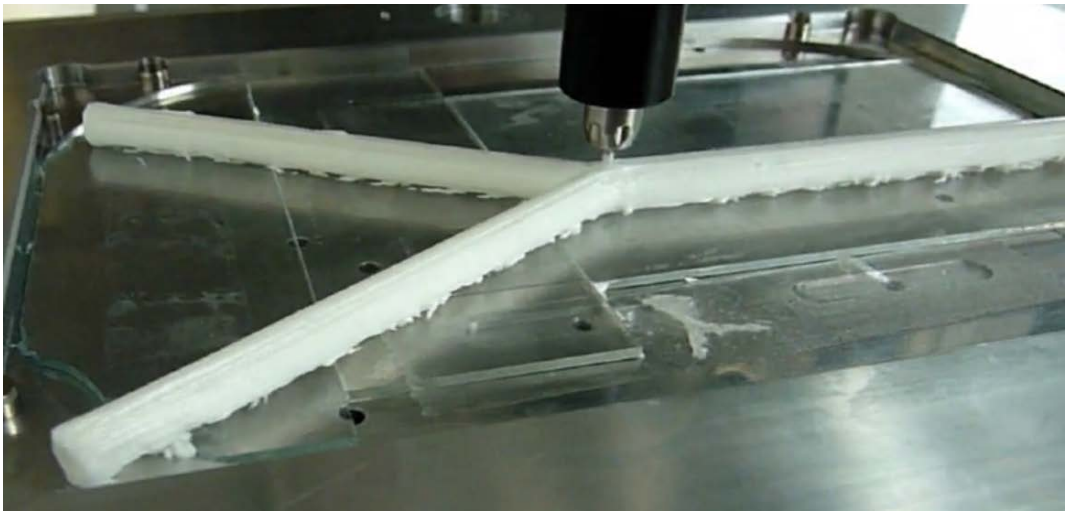

Figure 52 - Collagen-based 3D printed bifurcation

2.4 – Microparticle tracking

Simulation results were validated by tracking circulating injected latex microparticles[2]. The trajectory of blue polyethylene microparticles was tracked in the carotid and the flat coronary arterial PDMS scaffolds following the methodology described in chapter 5.11. As the microparticles had the same density as the fluid (1000 kg/m^3), the trajectories followed were considered analogue to the simulated fluid's streamlines. Dextran increased the fluid's viscosity without significantly altering its density up to physiological levels. The experiments had a few inherent limitations. Flow was driven by gravity so a continuous flow was imposed instead of pulsatile. The maximal velocities in the bifurcations were never reached due to a lack of height in the laboratory used. Also, the pump's vibrations affected the readings and interpretation of the data. These limitations may cause divergences between the computer simulations and the experimental testing since lower velocities imply smaller recirculation areas. A great recirculating pattern was observed in the low shear stress area of the ICA branch, the branch with greater recirculations according to the simulations (Figure 24 and Figure 26). These data were confirmed experimentally, as observed in Figure 53. As a control, particles tracked in the CCA did not experiment any recirculation (Figure 54).

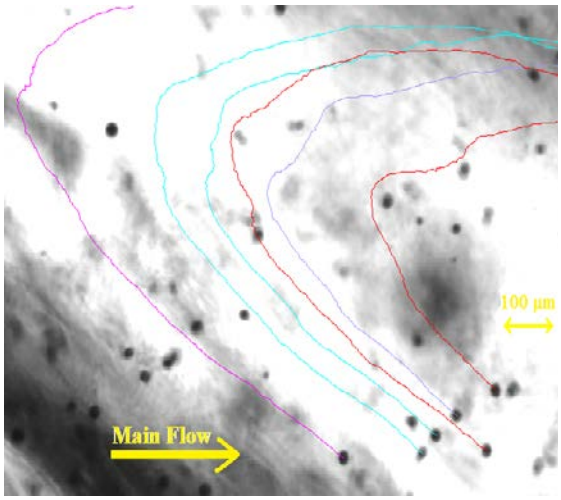

Figure 53 - Microparticles recirculating in the ICA

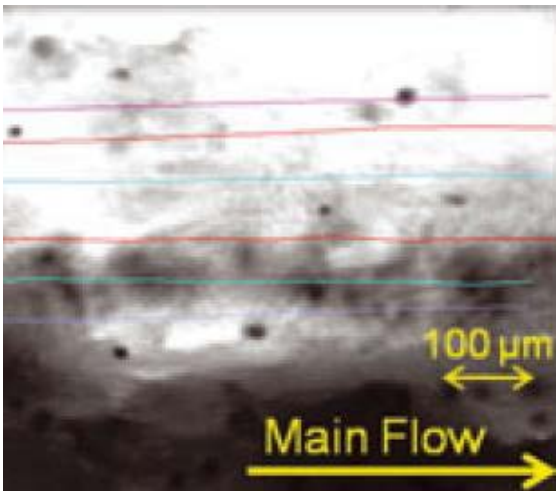

Figure 54 - Microparticles in the CCA

3 – ENVIRONMENT-DEPENDENT ATHEROSCLEROSIS BIOMARKERS IN EC

Intercellular cell adhesion molecule 1 (ICAM-1) and vascular cell adhesion molecule 1 (VCAM-1) expression by EC, the uptake of oxidized low density lipoprotein (Ox-LDL) by EC and the adhesion of monocytes to EC were used as biomarkers for atherosclerosis progression. Vascular cells were stimulated in several scenarios mimicking vessels that were healthy, injured, under inflammatory conditions or exposed to different flow regimes. The main objective of these studies was to map thrombosis risk as a function of the cells' environment.

The cascade of atherogenesis is evaluated along the section. Chapter 3.1 studies the toxicity of TNF-α in EC; chapter 3.2, the Ox-LDL uptake; chapter 3.3 and 3.4, the CAMs expression, and 3.5, the monocyte adhesion in tissue culture plates, straight tubes and bifurcations. In the experiments with exposure to flow, it will be discussed which mechanism explains the observed results, whether the shear stress mechanism or the mass transfer mechanisms discussed in chapter 1.1.

3.1. – Toxicity of tumor necrosis factor α in EC

The inflammatory cytokine tumor necrosis factor α (TNF-α) triggerss the inflammatory response through activation of the nuclear factor kappa-light-chain-enhancer of activated B cells (nf-κB) pathway but also kills vascular cells by triggering apoptosis. The cell survival is a function of exposure time to the cytokine and concentration of the cytokine. EC were cultured in TCP and exposed during 6, 12 or 24 hours to 5, 15 or 25 ng/mL of TNF-α. Cells exposed to 0 ng/mL of TNF-α during 24 hours served as negative control. After exposure, viability was evaluated using a live/dead assay. Results are presented as percentage of viable cells, which is a function of exposure time and TNF-α concentration (Figure 55). From this experiment on, the concentration used for every experiment requiring inflammatory activation was 3 ng/mL of TNF-α, concentration able to activate VCAM-1 expression (Figure 66) and not lethal to EC.

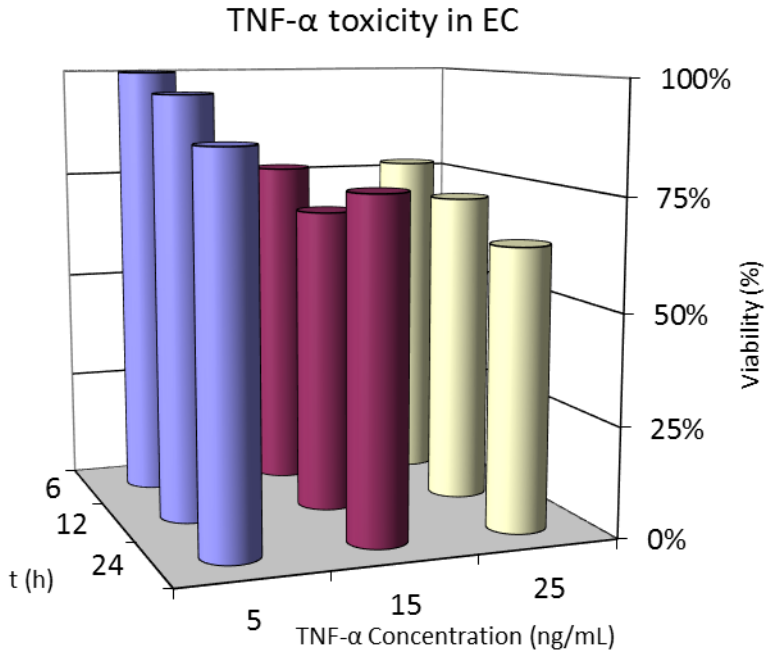

Figure 55 - TNF-α toxicity in EC

3.2 – Ox-LDL uptake

Ox-LDL is a crucial player in the progression of atherosclerosis (see chapter 1.2). A commercial derivate of Ox-LDL, Dil-Ox-LDL was used to estimate Ox-LDL uptake by activated EC. 1,1'-Dioctadecyl-3,3,3',3'-Tetramethylindocarbocyanine Perchlorate (Dil) is a fluorescent marker that emits at a wavelength of 580 nm and its presence in the samples was directly correlated to Ox-LDL absorption. This absorption was evaluated by immunofluorescence. The dose-response curve of Ox-LDL by EC was obtained. Cells grown on multiple well plates were exposed to 0, 5, 7.5 and 10 µg/mL for 48 hours, all within physiological values. Ox-LDL absorption was significant after the threshold of 7.5 µg/mL (Figure 56 and Figure 57). At 10 µg/mL (Figure 56), EC started to lose confluence as they detached and agglomerated. Interestingly, the Ox-LDL uptake was not affected by the presence of TNF-α (Figure 58). From these experiments on, the concentration of Ox-LDL was set to 7.5 µg/mL in EGM-2, without TNF-α activation.

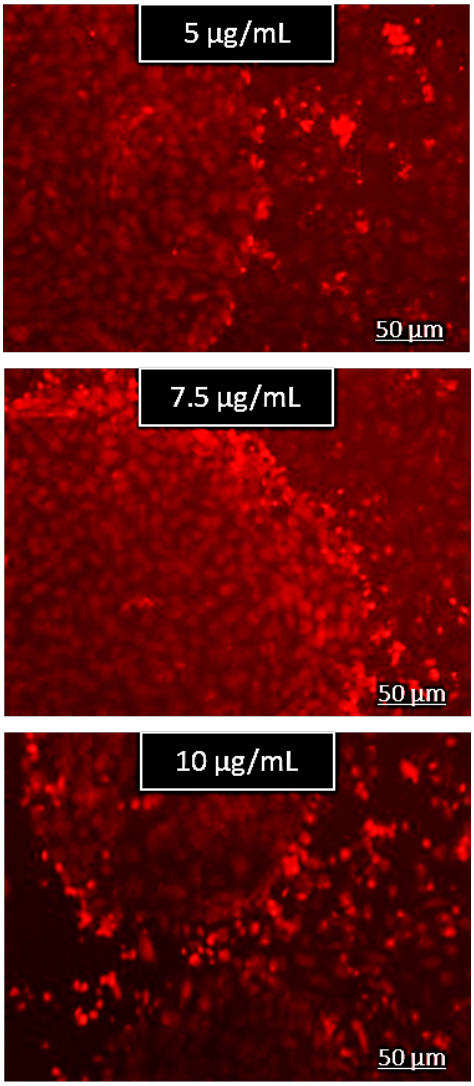

Figure 56 - Evolution of EC morphology as a function of Ox-LDL concentration

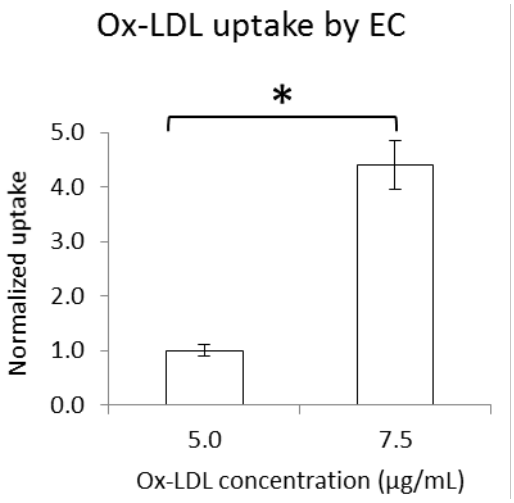

Figure 57 - Ox-LDL uptake by EC as a function of Ox-LDL concentration

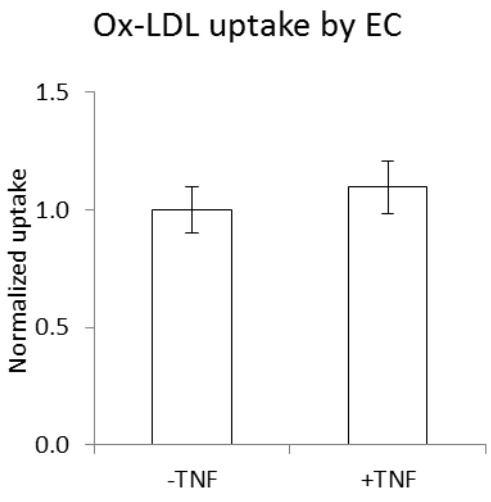

Figure 58 - Ox-LDL uptake by EC in the presence or absence of TNF-α

An initial test was run (Figure 59) to determine the homogeneity of the uptake along a tube. Untreated EC were exposed to arterial flow or static control for 24 hours. The tube was cut in four 2 cm-long sections (A, B, C, D) and the Ox-LDL content was evaluated for each section. The absorption was homogeneous along the tube. A second set of experiments was run in straight tubes seeded with EC, exposed to 24 hours of arterial flow, oscillatory flow and static control. As seen in Figure 60, oxidized LDL uptake rose 2.3-fold when EC were exposed to oscillatory flow and under static conditions. One may hypothesize that the mass transfer component is predominant since the oscillatory case and the static case have both null net flow.

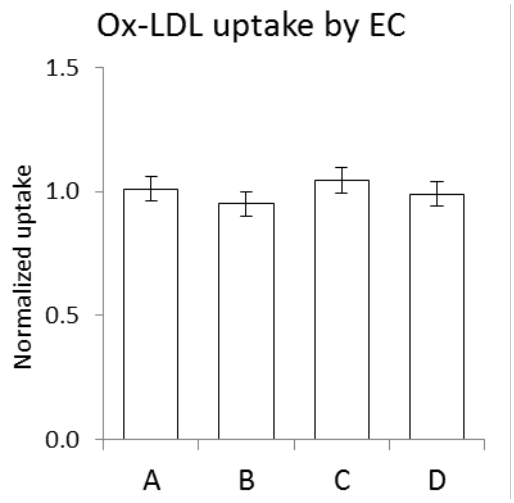

Figure 59 - Ox-LDL uptake by EC along a tube

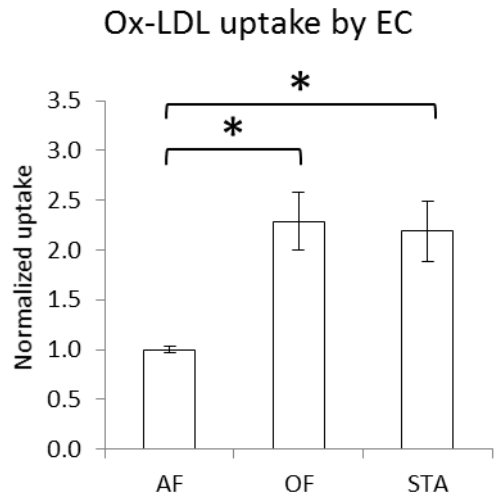

Figure 60 - Ox-LDL uptake by EC exposed to arterial flow, oscillatory flow and static control

In the bifurcated models, the Ox-LDL uptake increased linearly with the intensity of recirculations, up to 3-fold higher than upstream of the bifurcation divider in the internal carotid artery. As seen in Figure 61, the uptake perfectly correlated with the amount of recirculation in each branch of the carotid bifurcation. In Figure 62, one can observe that the increase in Ox-LDL is slightly lower than the increase in recirculations. Nevertheless, the Ox-LDL uptake still rose about 50% in the LCX and LAD.

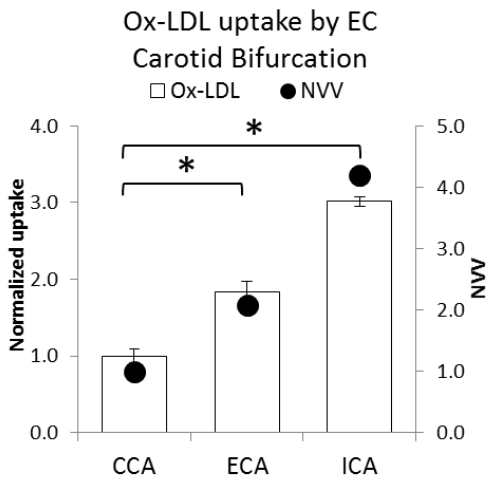

Figure 61 - Ox-LDL uptake by activated EC in the carotid bifurcation model

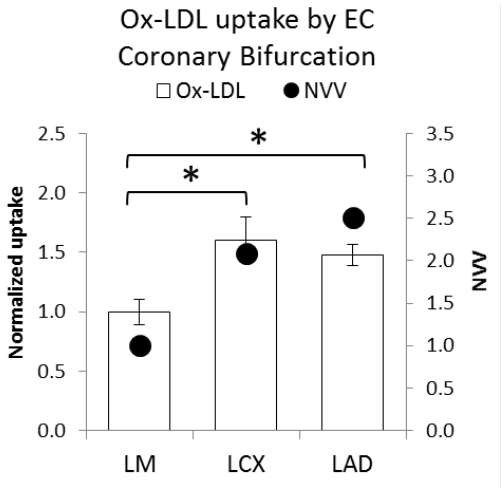

Figure 62 - Ox-LDL uptake by activated EC in the coronary bifurcation model

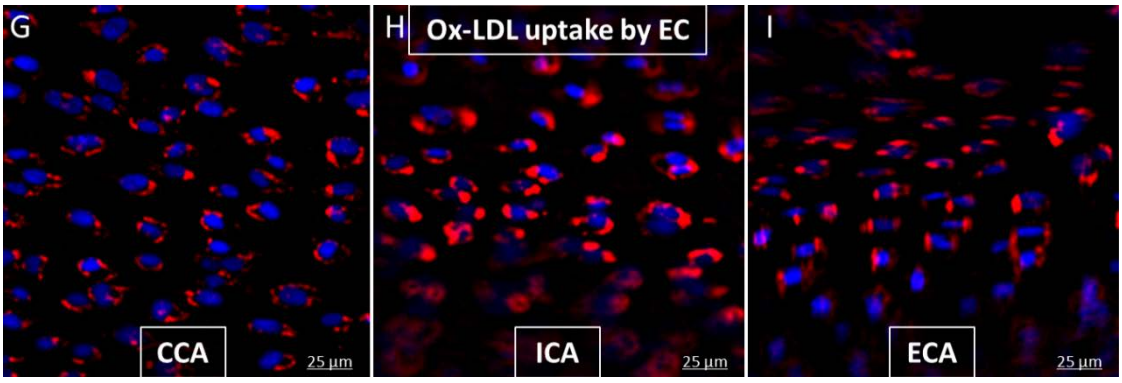

Figure 63 - Images of the Ox-LDL uptake by activated EC in each branch of the carotid bifurcation model

3.3 – ICAM-1 expression

ICAM-1 is a marker of activation of the intercellular NF-κB pathway, and its expression is triggered by inflammatory stimuli. There is a disparity in the literature regarding differential expression of ICAM-1 as a function of flow. While some authors determine that ICAM-1 levels are homogeneously increased in diseased vasculature in the presence of flow[18, 97], others affirm that ICAM-1 expression is stimulated by oscillatory shear stress[98, 99]. Endothelial cells were stimulated overnight with 3ng/mL of TNF-α and/or 7.5 µg/mL of Ox-LDL, and ICAM-1 levels measured by immunofluorescence. As seen in Figure 64, while the addition of Ox-LDL did not affect the ICAM-1 levels, exposure to 3 ng/mL of TNF-α was enough to increase ICAM-1 expression 2.5-fold. In EC and SMC seeded on straight tubes exposed to 24 hours of arterial flow, oscillatory flow and static control, ICAM-1 was almost undetectable without TNF-α activation. In Figure 65, the vascular cells were activated with 3ng/mL but the relative levels remained very similar both for EC and SMC. These results and the discrepancies observed in the literature prompted to discard ICAM-1 as biomarker of flow disruptions.

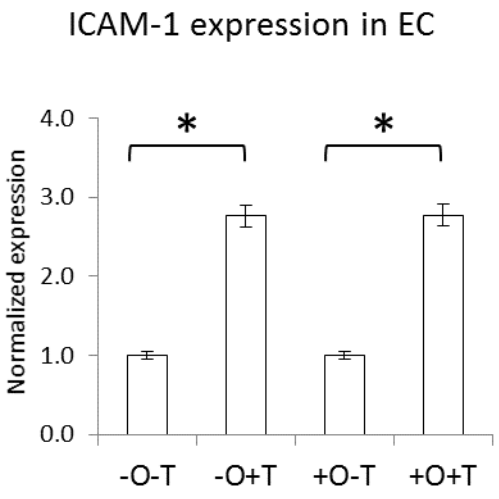

Figure 64 - ICAM-1 expression as a function of time and presence of TNF-α and Ox-LDL

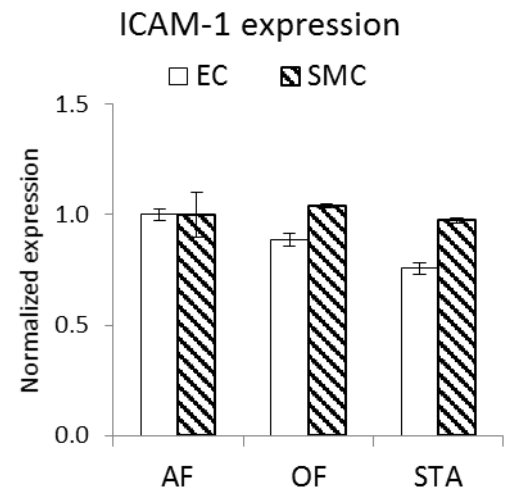

Figure 65 - ICAM-1 expression in EC and SMC exposed to arterial flow, oscillatory flow and static controls

3.4 – VCAM-1 expression

VCAM-1 is the protein that signals for monocytes recruitment and LDL uptake. Its expression reveals activation of the NF-κB pathway and is triggered by inflammatory stimuli. To confirm the data from the literature, endothelial cells were exposed for 12 hours to 3ng/mL of TNF-α. VCAM-1 expression was evaluated by western blot. As seen in Figure 66, the addition of TNF-α increased VCAM-1 expression 10-fold.

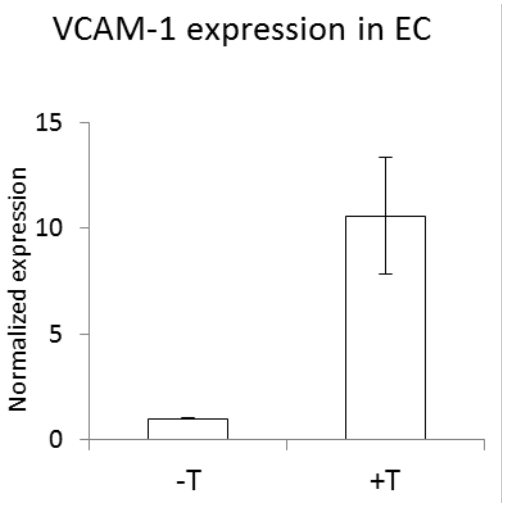

Figure 66 - VCAM-1 expression as a function of presence or absence of TNF-α

After confirming the increase in VCAM-1 expression under inflammatory conditions, EC seeded on straight tubes were exposed for 24 hours to arterial flow, oscillatory flow or static control, with and without TNF-α activation. As seen in Figure 67, EC exposed for 24 hours to low shear oscillatory flow (OF) increased a significant 60% their expression of VCAM-1 versus those exposed to coronary artery-like flow (AF). Arterial flow, unlike oscillatory flow offers seemingly protective effects on EC. Figure 68 shows how the difference in expression of VCAM-1 was muted when EC were activated by TNF-α. The same observations were made in the carotid (Figure 69) and coronary bifurcation (Figure 70) models, where VCAM-1 expression in activated EC remained not flow-sensitive. Thus, not only can disrupted flow exacerbate arterial injury but the integrity of intact arterial flow may play an important protective role as well.

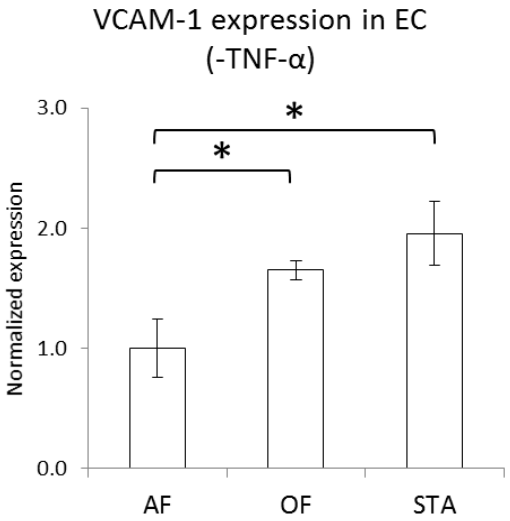

Figure 67 - VCAM-1 expression in untreated EC

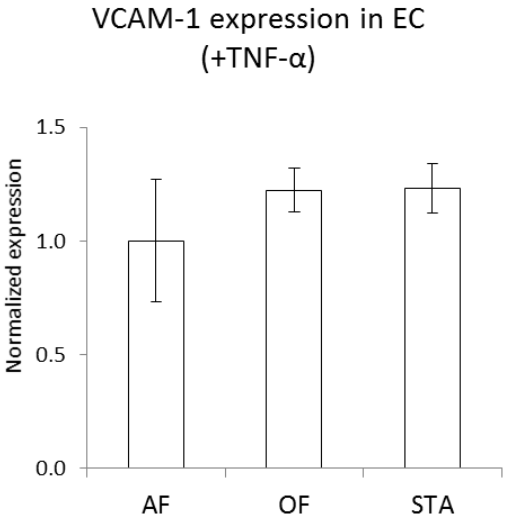

Figure 68 - VCAM-1 expression in activated EC

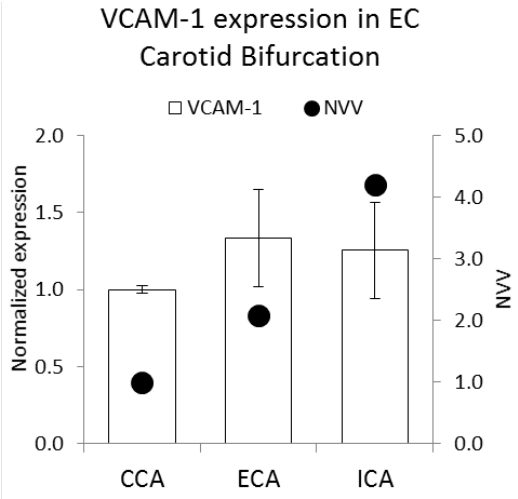

Figure 69 - VCAM-1 expression in activated EC in the carotid bifurcation model

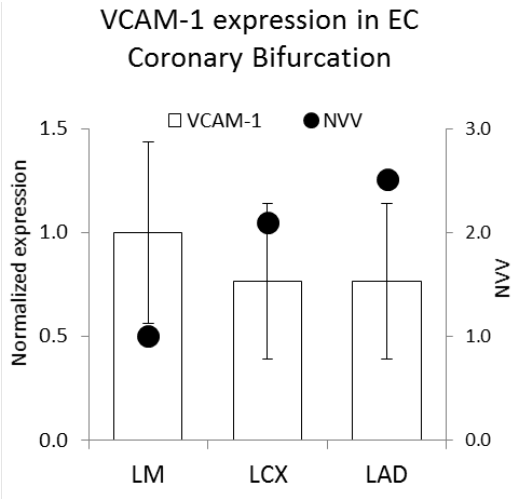

Figure 70 - VCAM-1 expression in activated EC in the coronary bifurcation model

3.5 – Monocyte adhesion to EC

Monocytes recruited by EC into the sub-endothelial matrix play a key role in the progression of atherosclerotic plaques. Blood from different healthy donors was used to evaluate monocyte adhesion. Recruitment was evaluated after fixing the samples and immunostaining them against α-tubulin and using DAPI to reveal nuclei. DAPI and tubulin signal intensities were significantly higher in monocytes than in EC, while monocyte size was significantly smaller than EC's size (1:100). These parameters were used to isolate monocytes from the EC matrix and count them using the image analysis software ImageJ. In preliminary assays, adhesion of monocytes was tested on confluent EC on TCP to estimate the amount of monocytes needed to pursue the perfusion bioreactor experiments. The isolated monocytes (see chapter 5.4) were incubated for 2 hours at 37ºC on activated EC in monocyte/EC ratios 0, 0.25, 0.5 and 1. As seen in Figure 71, the optimal ratio for quantification and signal to noise ratio was 1 monocyte/EC, and this was the ratio used in further experiments.

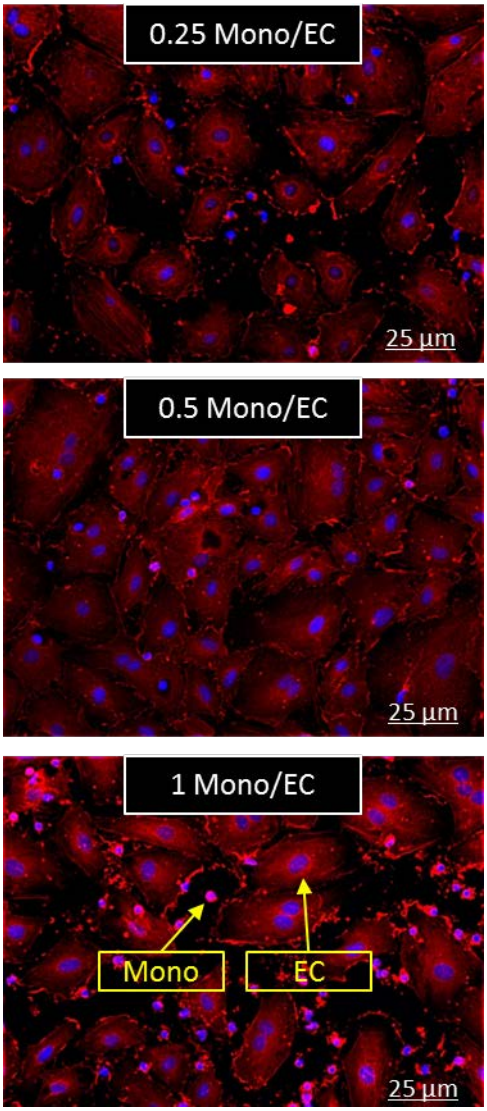

Figure 71 - Monocyte adhesion to EC on TCP as a function of monocytes concentration

The adhesion was analyzed in straight tubes seeded with EC exposed to 24 hours of arterial flow, oscillatory flow or static control and activated with TNF-α. After exposure to the different flow regimes, constructs were extracted from the flow loop and rotated at 37ºC and 5%CO_2 with previously isolated monocytes. This technique allows only studying the shear stress mechanism. This technique was used because monocytes died when pulsed with a peristaltic pump. As seen in Figure 72, in the presence of null net flow (oscillatory and static scenarios), the monocyte recruitment by activated EC doubled when compared to the arterial flow recruitment.

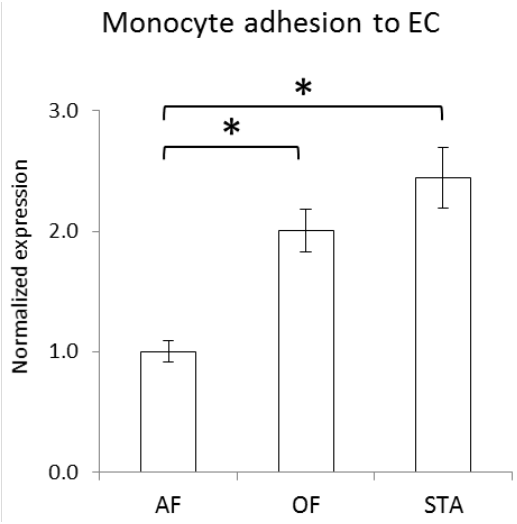

Figure 72 - Monocyte adhesion to activated EC exposed to arterial flow, oscillatory flow or static controls

In the bifurcated models, the monocyte attachment increased linearly with the intensity of recirculations, up to 2-fold higher than upstream of the bifurcation divider in the internal carotid artery. As seen in Figure 73 and Figure 74, there was a fair correlation between monocyte adhesion and with the amount of recirculation in each branch of the carotid and the coronary bifurcation. In both figures one can observe that the difference between adhesion levels between the upstream branches (LM and CCA) and the recirculating branches is lower than expected from values predicted by NVV. Nevertheless, the increases observed in every recirculation branch (50 to 100% increase) suggest that disrupted flow regimes differentially activate endothelial cells and hence monocyte recruitment. The mass transfer mechanism, which is omitted due to the procedure used, cannot be neglected due to the size and weight of monocytes. It is predictable that the model underestimates the total recruitment and that the actual *in vivo* values are much higher than those observed *in vitro.*

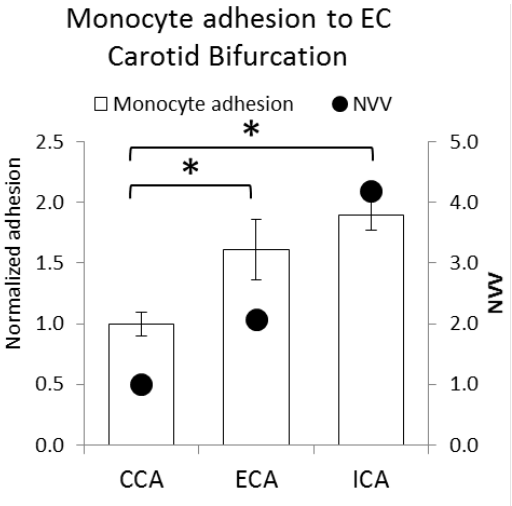

Figure 73 - Monocyte adhesion to activated EC in the carotid bifurcation model

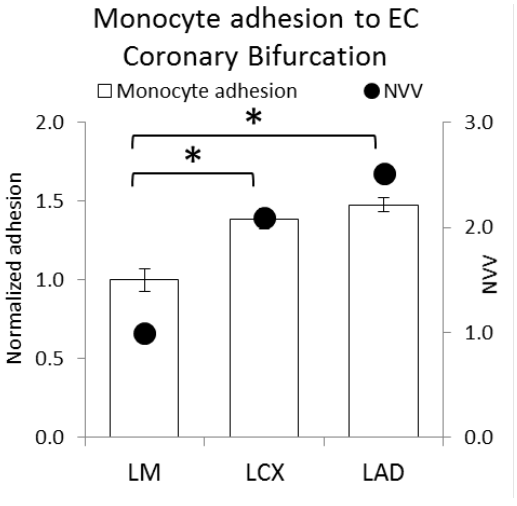

Figure 74 - Monocyte adhesion to activated EC in the coronary bifurcation model

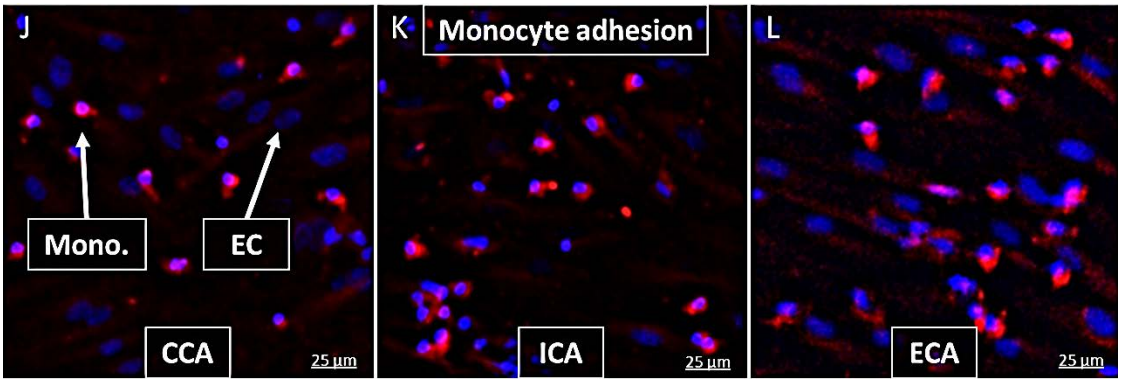

Figure 75 - Images of the monocyte adhesion to activated EC in each branch of the carotid bifurcation model

4 – ENVIRONMENT-DEPENDENT THROMBOSIS BIOMARKERS IN EC AND SMC

Tissue factor (TF) expression and activity in EC and SMC, thrombogenicity and re-endothelialization after injury were used as biomarkers for thrombosis. Vascular cells were stimulated in several scenarios mimicking vessels that were healthy, injured, under inflammatory conditions, stented, under anti-proliferative drug effects, exposed to different flow regimes and exposed to uremic solutes or serum. The main objective of this section of the thesis was to map thrombosis risk as a function of the cells' environment.

Chapter 4.1 studies cardiovascular disease biochemical and physical milieu, analyzing characteristics such as injury, flow and anti-proliferative drugs and chapter 4.2 studies uremic biochemical milieu. In chapters 4.1.1 and 4.2.1, whole cell TF expression is examined. Although, as seen in chapter 1.4, only monomeric membrane TF triggers coagulation by activating Factor VII and subsequently activating Factor X, the whole cell TF is a good indicator of thrombotic risk. In chapter 4.1.2, the intra- and inter-cellular trafficking of TF and sTF is evaluated. As seen in chapter 1.4, TF is not only expressed in the cellular membrane, but is also secreted to the blood stream as soluble tissue factor (sTF). Soluble TF released from an injured region, a given drug eluted from a drug eluting stent, and other inflammatory cytokines remain in the recirculation areas instead of being drained downstream and diluted systemically in the circulatory system. These solutes' trafficking depend upon the geometry of the stented artery and upon the stent positioning along the artery. The released solutes from the injured stented area are expected to increase TF levels downstream of the stented regions, especially in recirculating areas. In chapters 4.1.3 and 4.2.2, TF activity is studied, using two different approaches. One method evaluates the amount of activated Factor X and the other method evaluates total thrombogenicity of the sample. The Factor X assay does not necessarily correlate with the final thrombogenicity *in vivo* because other molecules like TFPI can disrupt the coagulation cascade. The thrombogenicity assay cannot fully correlate thrombus with TF activity since other biomolecules such as collagen can lead to blood coagulation. Nevertheless, the combination of both methods leads to reliable results in terms of correlation between TF content and activity, and vessel thrombogenicity. TF ability to initiate coagulation can be suppressed when applying anti-TF antibodies to the samples prior to the thrombogenicity assay. Chapter 4.1.4 will study re-endothelialization as a function of flow and correlate it to thrombogenicity in stents.

-

4.1. – Cardiovascular disease related risk factors

4.1.1 – TF expression

TF expression in basal conditions was evaluated in SMC and EC by immunofluorescence (Figure 76). TF expression in EC was below detectable levels but SMC expressed TF constitutively. EC and SMC exposed for 24 hours to 3 ng/mL of TNF-α and/or injured with cell scrappers to map TF expression as a function of cell type, TNF-α presence and proximity to the injury (Figure 77). TF intensity (green) in SMC did not react to TNF-α presence but increased in the edge (50-100µm away) of the injury.

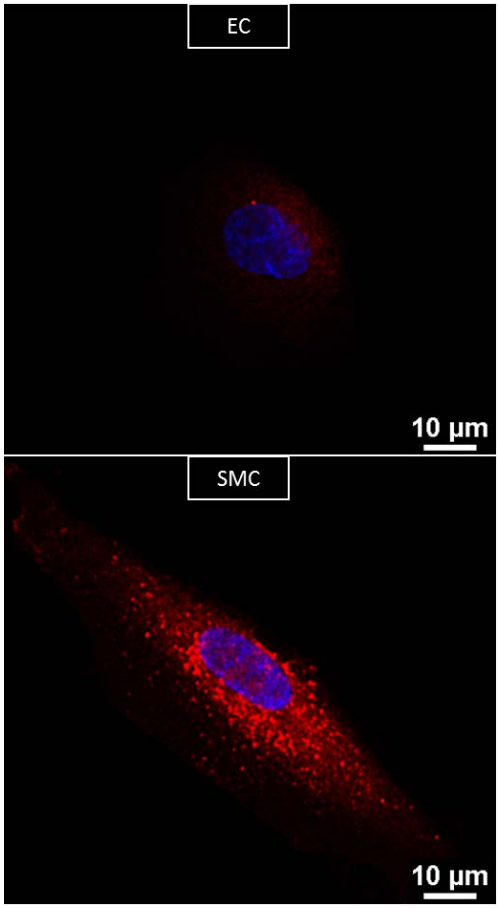

Figure 76 - Basal TF expression (red) in EC (top) and SMC (bottom)

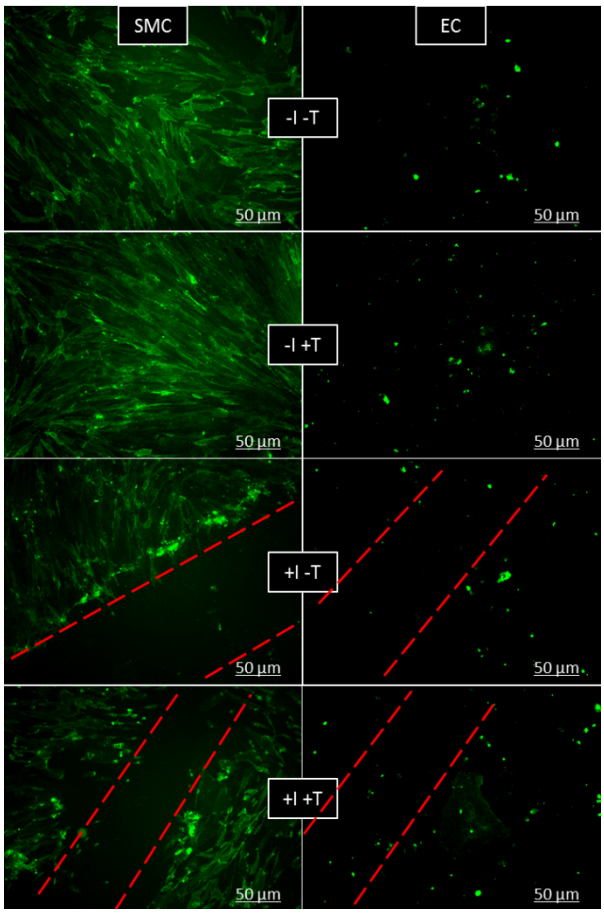

Figure 77 - SMC (left) and EC (right) TF (green) in presence of injury (I, red mark) and TNF-α (T)

Mono-cultures of SMC and co-cultures of SMC underlying EC were cultured and exposed for 24 hours to 0 or 10 nM sirolimus and/or injured with cell scrappers to map TF expression as a function of cell type, sirolimus presence and proximity to the injury. In Figure 78 and Figure 79, TF (red) and PECAM-1 (green) were labelled. Relative fluorescence was analyzed using ImageJ.

In both experiments (SMC alone and SMC/EC co-culture), cells on the edge of the injury showed higher levels of surface TF than intact controls. The TF expression in co-cultures and mono-cultures exposed to sirolimus increased to a similar extent than cells injured. In the case of double stimulation (injury + sirolimus), sirolimus synergistically increased TF expression in SMC healing the injury. Samples were not permeabilized during the immunostaining procedure. This way, the diffusion of the antibody anti-TF through the endothelial shield mimicked the molecules binding to TF present in the blood torrent (Factor VII and Factor X). TF expression evaluated by immunofluorescence was indeed tuned down by the presence of EC shielding the SMC.

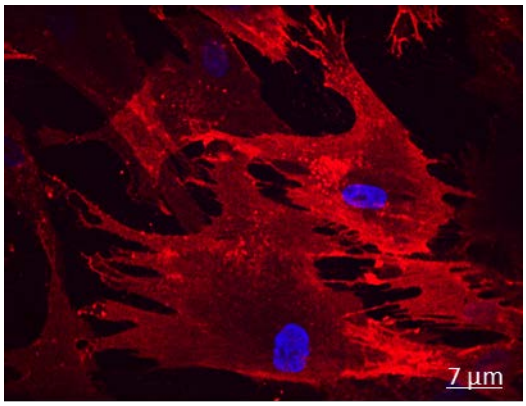

Figure 78 - TF expression (red) in SMC healing an injury

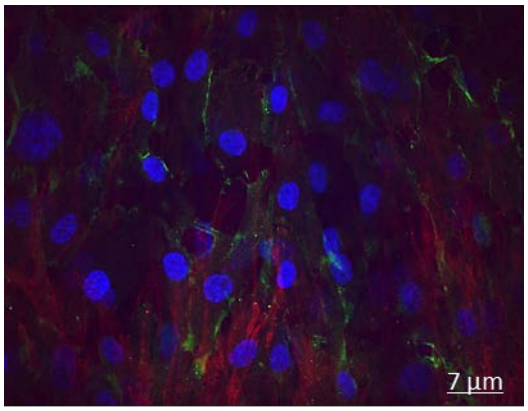

Figure 79 - TF expression (red) in SMC shielded by EC (CD31, green)

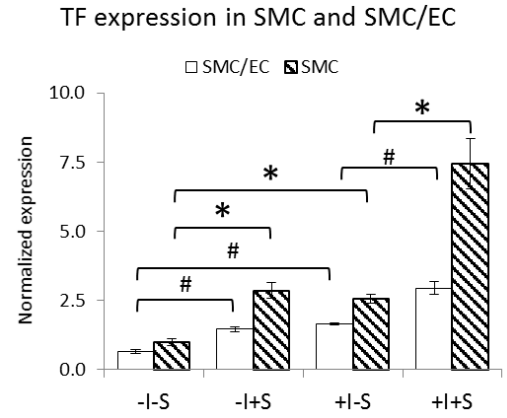

Figure 80 - TF expression as a function of presence or absence of injury (I) and sirolimus (S) in EC overlying SMC and SMC

The effect of 24 hours exposure to arterial flow (AF) on TF expression was evaluated in SMC, EC and SMC underlying EC. TF was immunostained and the TF concentration evaluated using ImageJ on the confocal microscope images (Figure 81). TF levels in EC were below the detection threshold. TF expression was 1.5 to 2-fold lower in SMC exposed to AF versus the static control (Figure 82). This result was confirmed in the co-cultures, where, as previously seen, EC shielded SMC. The fact that null shear cells expressed twice the amount of TF suggests that in areas with low shear flow disruptions, TF expression would be higher than in arterial flow regimes.

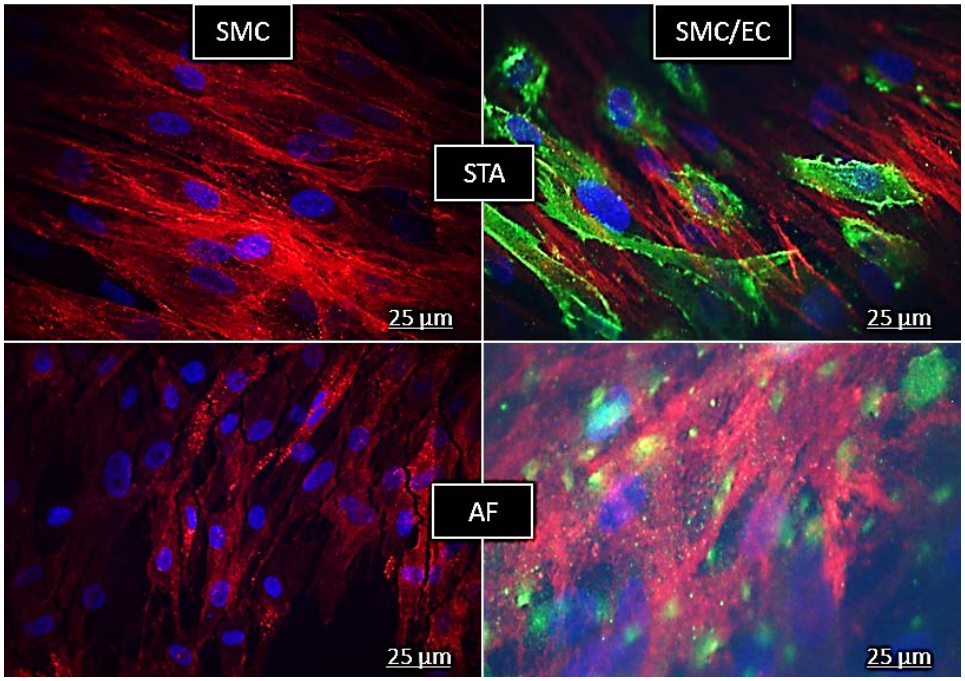

Figure 81 - Images of TF expression (red) in SMC alone (left) or underlying (right) EC (CD31, green) when exposed to arterial flow (AF) or static control (STA)

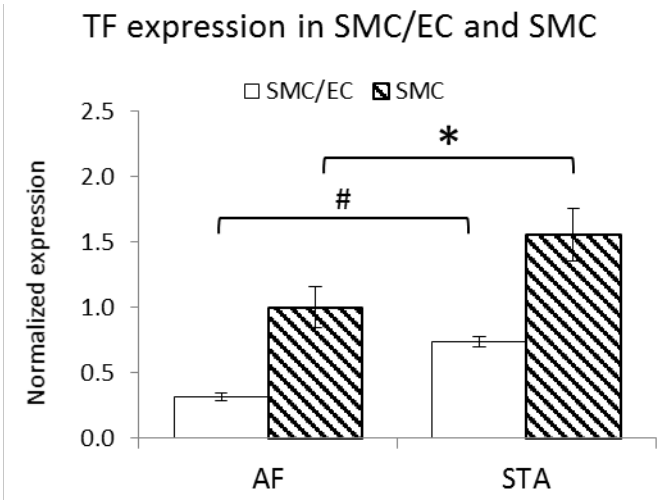

Figure 82 - TF expression in SMC and EC overlying SMC exposed to arterial flow (AF) or static control (STA)

TF expression was evaluated in mono-cultures of activated EC (before intervention) and in untreated SMC (after intervention) after exposure to 24 hours of arterial flow, low shear oscillatory flow and static controls. TF expression by SMC was evaluated using immunofluorescence and TF expression by EC was measured using western blot. Preliminary experiments suggested activation of EC with 3 ng/mL of TNF-α to detect TF in EC using western blot. AF decreased SMC's TF expression compared to static conditions (1.75-fold decrease). More interestingly, oscillatory flow enhanced TF levels exceeding the static control, 2.5-fold higher than the AF results (Figure 83 and Figure 85). Oscillatory flow is a model of flow disruptions, and literature[100] has proved that flow regime around stent struts is oscillatory. The TF expression data on oscillatory flow is very interesting since it implies that oscillatory flow around the stent strut increases the TF expression in SMC and hence its thrombogenicity. In activated EC, the oscillatory flow caused a tremendous 4.5-fold increase in TF expression but the static control remained similar to the arterial levels (Figure 84 and Figure 86). These data suggest that only the combination of strict oscillatory flow combined with inflammatory conditions increases thrombogenicity in intact EC. It also suggests that thrombogenicity in the stent strut surroundings can be due not only to flow-exposed SMC, but also to injured EC in inflamed regions exposed to oscillatory flow regimes.

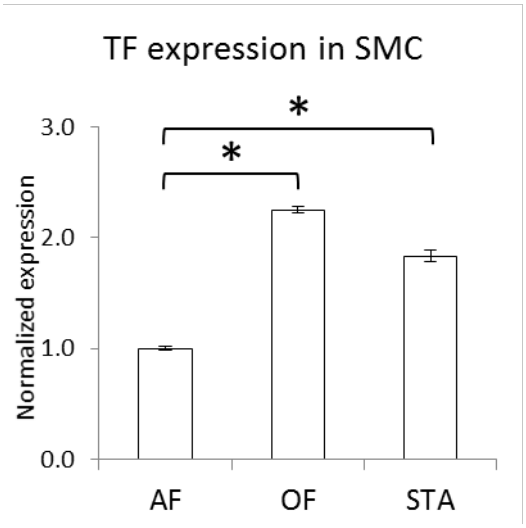

Figure 83 - TF expression in untreated SMC exposed to arterial flow, oscillatory flow or static controls

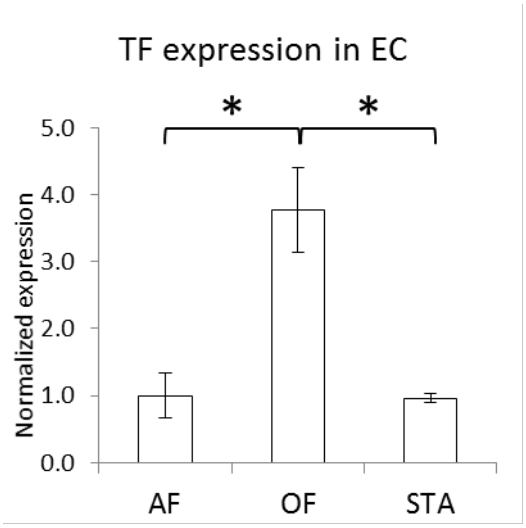

Figure 84 - TF expression in activated EC exposed to arterial flow, oscillatory flow or static controls

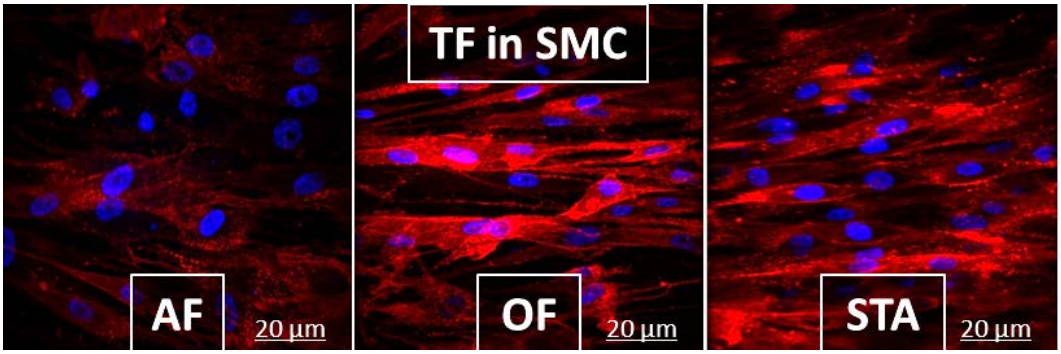

Figure 85 - TF expression in untreated SMC exposed to arterial flow, oscillatory flow or static controls, evaluated by immunofluorescence

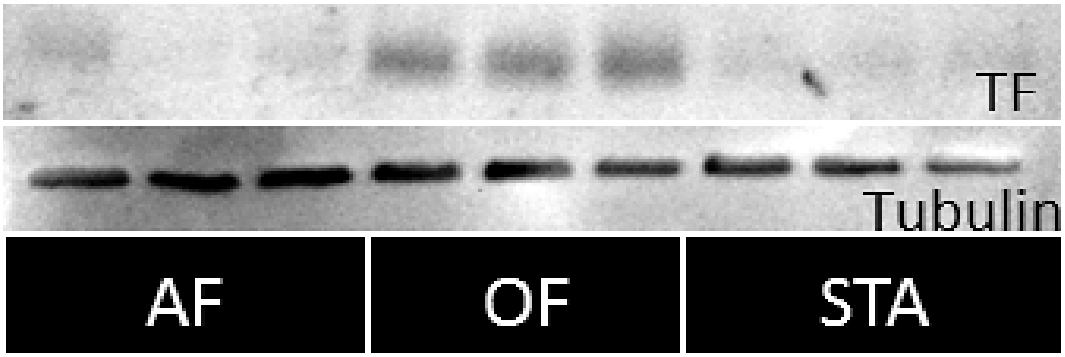

Figure 86 - TF expression in activated EC exposed to arterial flow, oscillatory flow or static controls evaluated by western blot

The deployment of a stent in an artery injury in the vessel and flow disruptions around the stent strut. These two elements combined with the anti-proliferative drugs coating the drug eluting stents may enhance TF expression. Experiments were performed in order to study the effect of stenting in SMC TF expression. Effects of injury, drug and flow disruptions were examined in parallel. In an initial approach to understand TF distribution downstream of the stented region, straight tubes were sectioned following the scheme in Figure 87 The areas defined were “Stent”, “Proximal”, “Medial” and “Distal”, where “Stent” corresponded to the stented region, “Proximal” extended from 0 to 5 mm after the stent, “Medial” from 5 to 10 mm and “Distal” from 10 to 15 mm.

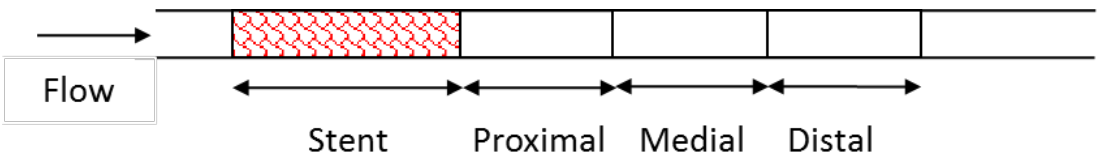

Figure 87 - Regions distribution

Straight constructs were seeded with SMC, stented with NIR Stents (see chapter 5.1.5) and exposed to arterial flow or static controls (Figure 88). There were no significant differences between the proximal, medial and distal zones in the static controls as expected in the absence of flow disruptions. The stented area, however, showed higher TF expression due to the injury caused by the stent. In SMC exposed to AF, the stented area showed a significant 2-fold difference with the medial and distal area. More interestingly, the proximal and stented area presented very similar levels of TF. Two mechanisms potentially took place and resulted in the measured increased TF within the proximal region. On the one hand, flow disruptions caused by the stent should increase TF levels in the vicinity of the stent. On the other hand, the soluble TF released in the stented area might be increasing the TF content in the SMC in the proximal area similarly to what has been published with other proteins[100].

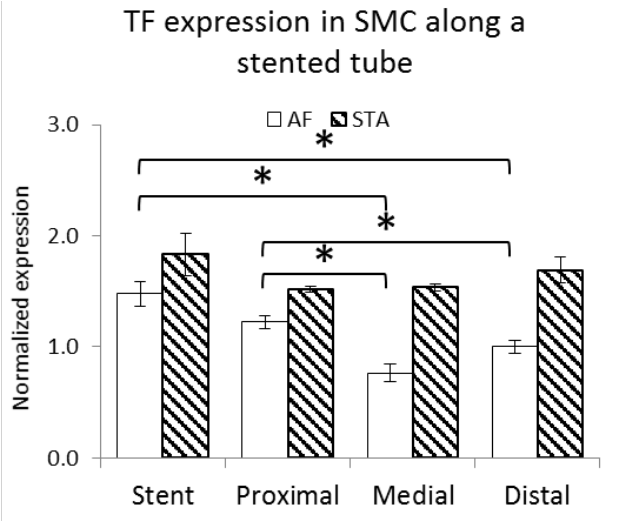

Figure 88 - TF expression in SMC exposed to arterial flow or static controls after stenting

Cordis® bare metal stents and sirolimus eluting stents were expanded in straight constructs seeded with SMC underlying EC. The experiment compared the effects of balloon injury alone, deployment of a bare metal stent and deployment of a sirolimus eluting stent on TF expression after 24 hours of arterial flow or its static control. Results were evaluated by immunofluorescence. Figure 89 shows the matrix of results of this experiment.

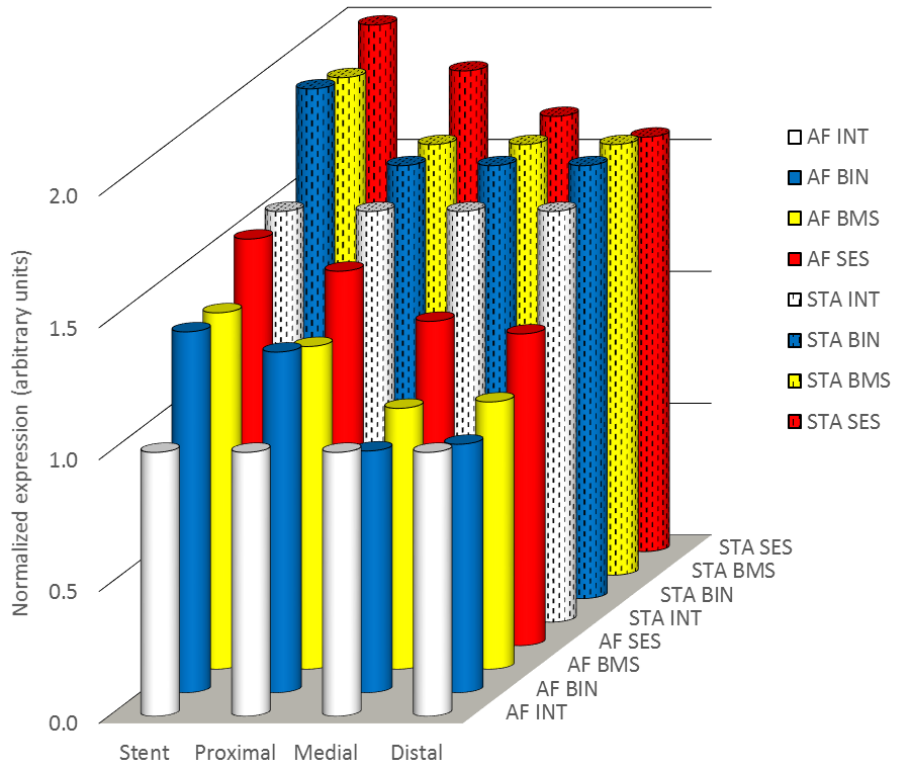

Figure 89 - TF expression in SMC with overlying EC, exposed to arterial flow (AF) or static control (STA) and left intact (INT) or injured with a balloon (BIN),a bare metal stent (BMS) or a sirolimus eluting stent (SES)

A 1.75 to 2.5-fold average decrease in TF values was observed again for cells under arterial flow versus those under static conditions. No significant differences were observed between TF expression in cells injured with a balloon and TF expression in cells injured with a bare metal stent. This suggests that the overexpression of TF due to the injury during stent implantation is mainly caused by the balloon protruding in the inter-strut region In terms of TF upregulation, doing an angioplasty or deploying a stent was equivalent. Both for flow and static conditions, cells injured with drug eluting stents expressed 1.2 to 1.5-fold more TF than those injured with balloon or bare metal stents, in accordance with published data[101]. More interestingly, and particularly in the flow experiments, sirolimus and sTF eluted to the cells downstream the stent, causing an increase of TF expression in the medial and distal areas to the stent, especially in the sirolimus eluting stents.

To mimic the diseased vessel before and after stenting or angioplasty, TF expression was evaluated in mono-cultures of activated EC (before intervention) and in untreated SMC (after intervention) after exposure to 24 hours of arterial-like flow in the bifurcated models. TF expression in SMC had direct correlation with the amount of recirculation in each branch of the studied bifurcations (Figure 90 and Figure 91). It rose up to 2-fold in the ICA but only a

35% in the ECA when compared to the CCA values. In the coronary bifurcation, the increase ranged between 35% and 50% for LAD and LCX vs. LM. Very surprisingly, in apparent discordance with the observations from the simplified model, TF expression in activated EC decreased about 50% in the ICA and ECA compared to the CCA (Figure 92). In the coronary bifurcation, the TF expression did not significantly differ among cases (Figure 93). Globally, high recirculation levels downregulated TF in activated EC and mild recirculation did not affect the values. These results suggest a complex interaction between the different flow fields within the bifurcated region. The complete mechanism remains to be fully understood.

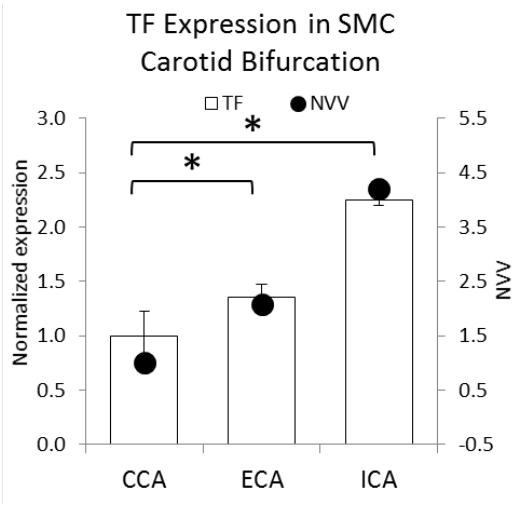

Figure 90 - TF expression in untreated SMC in the carotid bifurcation model

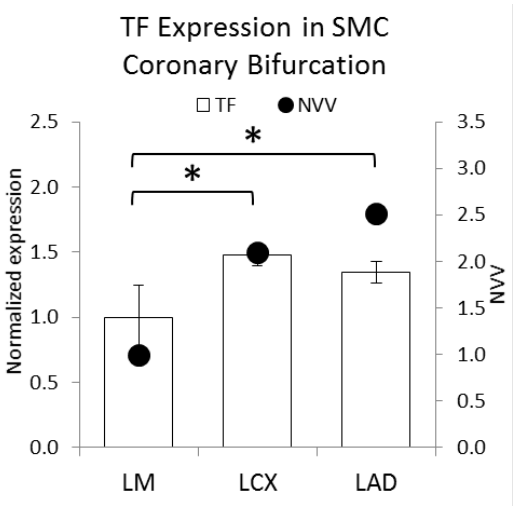

Figure 91 - TF expression untreated SMC in the coronary bifurcation model

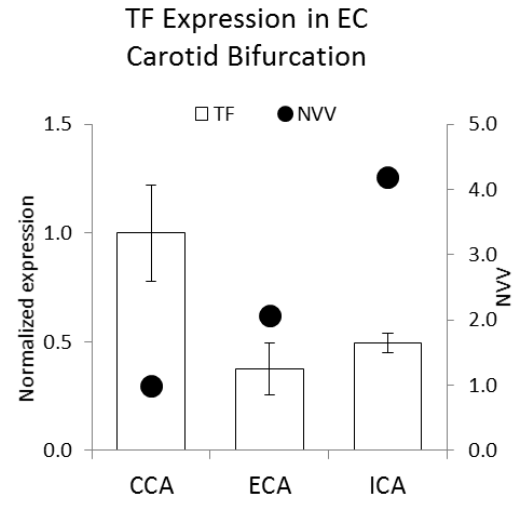

Figure 92 - TF expression in activated EC in the carotid bifurcation model

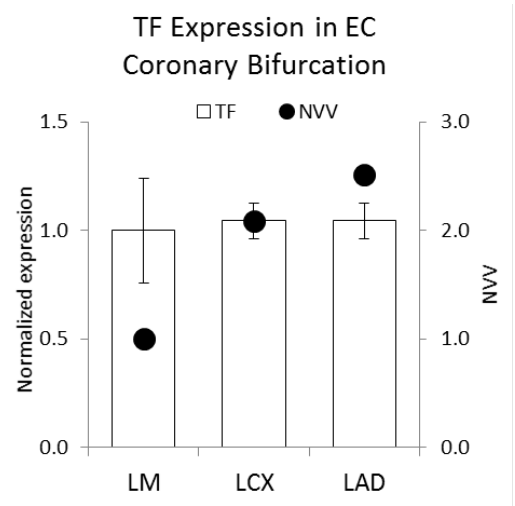

Figure 93 - TF expression in activated EC in the coronary bifurcation model

4.1.2 – TF trafficking

An experiment was performed to evaluate sTF release in vascular cells under conditions simulating a stented region. sTF release was evaluated in EC, SMC and EC overlying SMC cultured on TCP and exposed for 48 hours to 0 or 10 nM sirolimus and/or injured with cell scrappers. Preliminary results (Figure 98) indicated that the activity of TF was higher after 48 hours of exposure to injury and sirolimus. After exposure, supernatant media was collected and sTF content was evaluated by ELISA. The values obtained were used to run sTF distribution simulations (Figure 27, Figure 28, Figure 35 and Figure 36) and to define critical regions in terms of sTF deposition. As seen in Figure 94, sTF release by EC mono-cultures was near the detectability threshold and sTF release by mono-cultured SMC was independent of the stimuli. In co-culture, sTF release by injured cells was higher than sTF released by sirolimus stimulated cells and higher than the intact control. The combination of sirolimus and injury slightly increased the sTF release values from only injured cells.

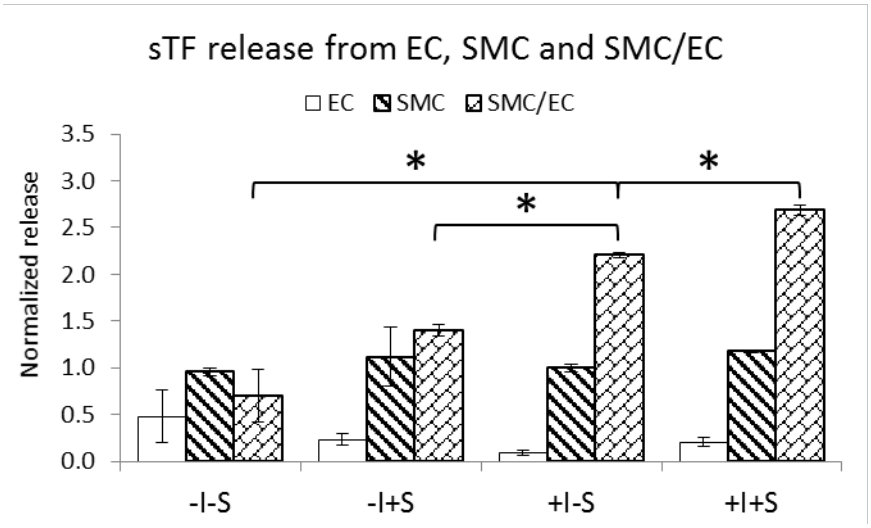

Figure 94 - sTF release in EC, SMC and SMC underlying EC stimulated by injury (I) and/or sirolimus (S)

In a second set of experiments, co-cultures of SMC and EC in TCP were stimulated in conditions mimicking a stented environment. Cells were exposed for 48 hours to 0 or 10 nM sirolimus and/or injured with cell scrappers. After the exposure, the supernatant media was collected and exposed for 48 hours to intact, untreated monocultures of EC and SMC and co-cultures of SMC and EC. This step simulates the exposure of healthy vascular cells downstream a stented vessel to the inflammatory cytokines released by the process of stenting. Cells were exposed to the conditioned medium for 24 hours and TF values were evaluated by western blot of the whole cell lysate (Figure 95).

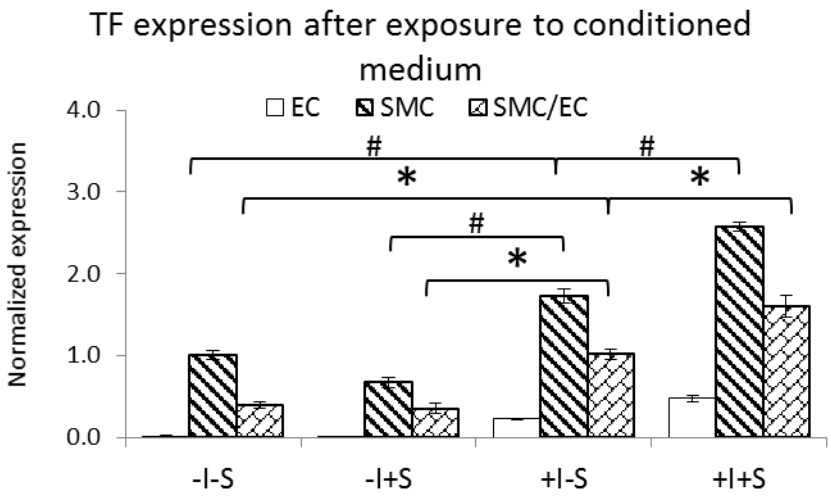

Figure 95 - TF expression by untreated EC, SMC and SMC/EC exposed to conditioned medium from SMC/EC stimulated by injury (I) and/or sirolimus (S)

Total TF in EC, SMC and co-cultures of SMC underlying EC was higher when cells were exposed to conditioned medium from SMC/EC stimulated by injury and sirolimus. Also, conditioned medium from sirolimus-only stimulated SMC/EC did not seem to alter the basal TF levels in any of the three combinations of exposed cells. Although TF expression in EC mono-cultures was generally below detectability limits, EC seemed sensitive to injury and injury plus sirolimus conditioned media. As a final observation, TF expression in SMC/EC co-cultures was approximately half the expression in SMC mono-cultures. These results are in accordance with the 1:1 ratio at which SMC and EC were seeded in the co-culture and confirm that, also in co-culture, SMC are the main source of TF. This is not an affirmation but an assumption because the methodology used (whole cell lysate) cannot separately analyze EC and SMC contribution to TF expression. One can solidly conclude in any case that injury and injury plus sirolimus conditioned media promote TF increase in quiescent SMC/EC co-cultures and that this is relevant to stent design and placement.

A series of mechanisms can be proposed to explain the results previously described. Sirolimus might be promoting TF internalization and preventing downstream expression by not allowing release to the medium. This might be achieved by inhibiting the intracellular TF trafficking pathway. One could also think that the EC shielding in SMC/EC co-cultures affects sirolimus-SMC interaction and/or prevents sTF release from SMC to the medium. EC may however still be able to promote TF activation to underlying SMC through paracrine signaling, even with efficient shielding from molecules promoting TF in the conditioned medium. Also, if EC shielding was not efficient, TF promoters could diffuse through the endothelial monolayer and

induce TF expression to underlying SMC. Finally, another less complicated hypothesis states that sirolimus degrades and loses efficiency along the 96 hours that the experiment lasts. A series of experiments can be proposed to confirm the hypothesis previously stated. The intracellular trafficking of TF and compartmentalization could be studied to understand whether sirolimus enhances TF localization in a certain cellular pool[54]. Ultracentrifugation (Figure 96) confirmed that the cellular membrane allocated most TF, but the cytoplasm and the nucleus contents were not negligible. The effect of sirolimus in TF compartmentalization has not been elucidated yet. Finally, the biochemical mechanistic of sTF in cells downstream the stented region should be evaluated to determine whether sTF gets internalized by untreated cells or promotes TF expression. The approach would be to genetically modify the released sTF to make it fluorescent and determine its presence in downstream cells. In parallel, one should tag TF produced by downstream cells in order to fully differentiate sTF uptake from TF expression engagement.

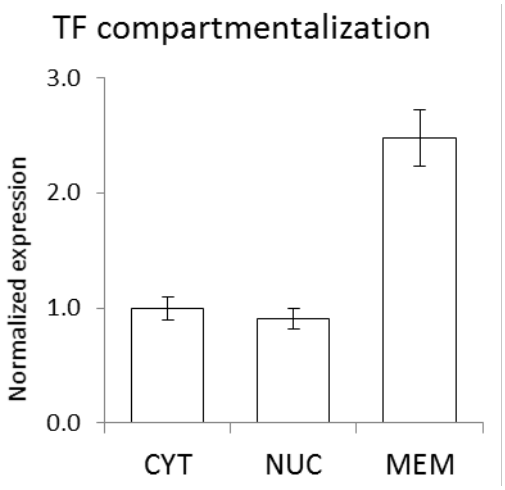

Figure 96 - TF distribution in the cytoplasm (CYT), nucleus (NUC) or membrane (MEM) in SMC

4.1.3 – TF activity

As seen in chapter 1.4, TF is able to bind to Factor VII and trigger coagulation only when it's active. Only membrane TF in monomeric state is able to initiate the coagulation cascade and is hence "active TF". A logical approach would be quantifying monomeric TF in the membrane fraction of whole cell lysate. To do so, whole cell lysate may be lysed using non-reducing lysis buffers to run native western blot and protect the original protein polymerization. Unfortunately, the ultracentrifugation technique required reducing reagents and yet native western blot and ultracentrifugation were not compatible techniques. The method to quantify only monomeric (active) TF was assayed in confluent SMC cultured on tissue culture plates. The method worked but was not applicable to the vessel-like constructs due to the lower cellular concentration present in constructs. Figure 97 shows an example of a native gel where multiple TF polymers can be observed.

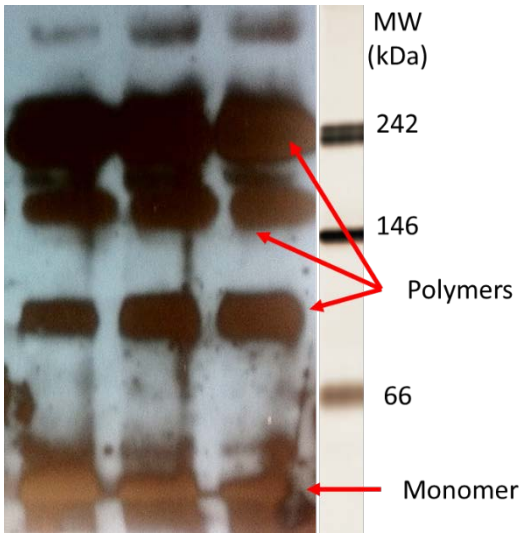

Figure 97 - TF expression by untreated SMC in a native gel

TF activity may be measured by other means. As active TF activates Factor VII and Factor X is activated by Factor VIIa, a measure of Factor Xa concentration would correlate with TF activity. To measure sTF activity, a co-culture of SMC and EC on TCP was injured with cell scrappers and exposed to 10 nM sirolimus for 48 hours (Figure 98). Then, in a consecutive experiment, untreated SMC were exposed to the collected conditioned medium. After 24 hours, activity of sTF present in the medium was measured (Figure 99). In both experiments concentration of Factor Xa in the medium was measured using an activity assay. In the first experiment, the released sTF activity showed a first 2-fold peak after 2 hours, decreased to basal levels, but increased again between 24 and 48 hours to reach an apparent 4-fold plateau. Given the acute nature of TF as trigger of the coagulation cascade after injury, one may hypothesize that the

peak observed after 2 hours is an acute response to injury and the second peak responds to the action of sirolimus. In the second experiment, the sTF activity started peaking after 2 hours, and reached a 2-fold plateau after 4 hours. In this case, sTF is an indistinguishable sum of the original sTF present the original conditioned medium and the sTF released by SMC. In any case, it is always higher than the one observed in Figure 98, indicating extra release by SMC after sensing condition medium. This result is relevant in terms of stenting. It indicates that vascular cells downstream of a sirolimus-stented region sense injury and drug presence upstream and reacts by increasing the activity of soluble TF.

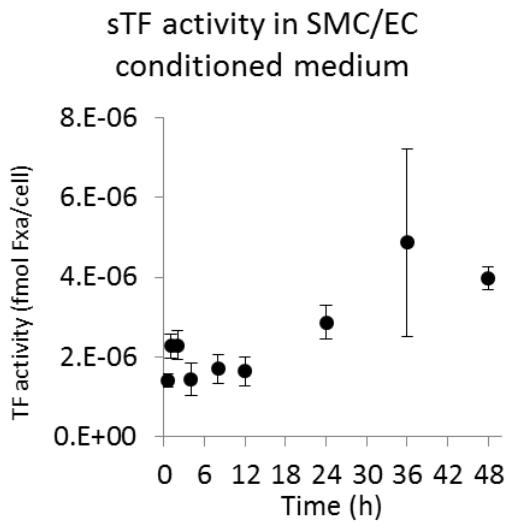

Figure 98 - sTF activity measured in medium released by injured SMC/EC exposed to 10 nM of sirolimus

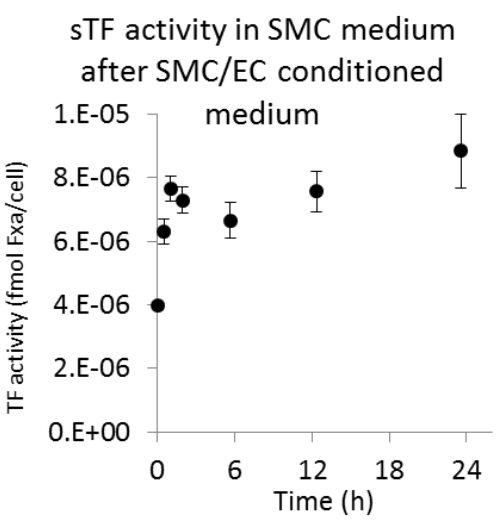

Figure 99 - sTF activity released by SMC exposed to conditioned medium from injured SMC/EC stimulated by 10 nM sirolimus for 48 hours

Another strategy to evaluate TF activity is measuring cellular thrombogenicity. This way, one can correlate increase in TF expression with increase in TF activity without measuring monomeric membrane (active) TF. The flow loop assay described in chapter 5.3 was used to determine thrombogenicity in straight cell-seeded constructs. The prototype needed to be much further developed to assess thrombogenicity in the bifurcated models and hence no experiments were run with bifurcated models. The method had never been used before to estimate TF activity in vascular cells. A slight modification of the method was also applied (Figure 100): first, the heme concentration was linear with blood concentration in the lysate so it could be directly correlated with the amount of thrombus. Second and more interestingly, the direct measure of the absorbance of the sample at 405nm correlated with the measured heme concentration. Thanks to this correlation, a heme quantification assay was not needed

and hemoglobin concentration could be estimated by directly measuring the absorbance of the lysed sample. A preliminary experiment was run to adjust the experimental conditions for cell-seeded constructs (Figure 101). Four straight tube types were tested. The first set was empty, the second had been treated with fibronectin, the third had been seeded with SMC, and the fourth was seeded with EC. The experiment confirmed that SMC denuded from EC are much more thrombogenic than EC. Also, untreated or fibronectin-coated silicon rubber tubes were not thrombogenic.

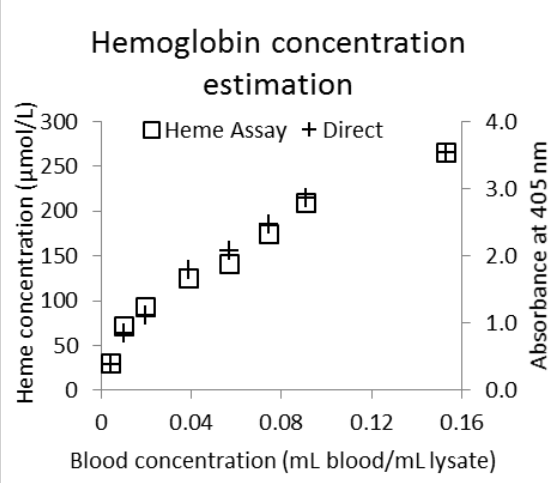

Figure 100 - Hemoglobin concentration in blood measured through heme assay or with direct absorbance

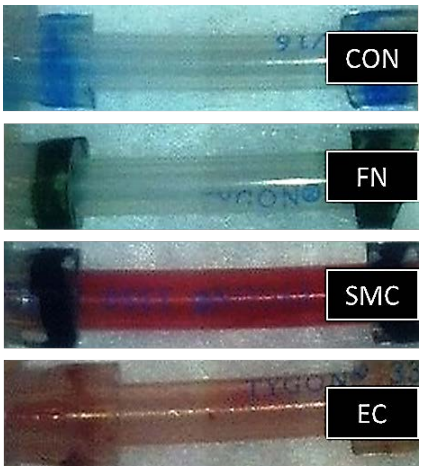

Figure 101 - Thrombogenicity in straight tubes

A matrix of experiments was performed to understand how flow and stent injury interact in stent thrombosis. Straight tubes seeded with EC, SMC or SMC underlying EC were stented with NIR stents or left intact and exposed to arterial flow, oscillatory flow and static controls. Figure 102 and Figure 103 summarize the results. Intact EC, SMC and EC/SMC constructs were always more thrombogenic when exposed to oscillatory flow. In the static controls, EC and EC/SMC were as little thrombogenic as arterial flow, but not SMC alone, that were as thrombogenic as the oscillatory case. These results are in accordance with those depicted in Figure 83 and Figure 84, and confirm TF as a good biomarker for thrombosis in this experimental setup. Furthermore, the EC/SMC construct, when intact, behaves exactly like an EC monoculture. When cells were stented and exposed to different flow regimes, the results experienced interesting variations. While SMC reaction to flow remained the same, the reaction of EC and EC/SMC constructs diverged from the intact data. EC, surprisingly, were much less thrombogenic under oscillatory conditions than under static or arterial flow, which

had the highest levels of clotting. Contrariwise, the EC/SMC constructs were more thrombogenic when the samples were exposed to oscillatory flow, but less when in the static controls. These data can only be explained by a counter-balance between re-endothelialization and TF expression by cells in contact with blood flow. One may hypothesize that OF promotes both TF expression, but also re-endothelialization. If SMC are present, clotting would be higher due to increase in TF from SMC, but if absent, EC recover faster the metal strut and the surface exposed to flow. Only the re-endothelialization experiments in chapter 4.1.4 can confirm these hypothesis.

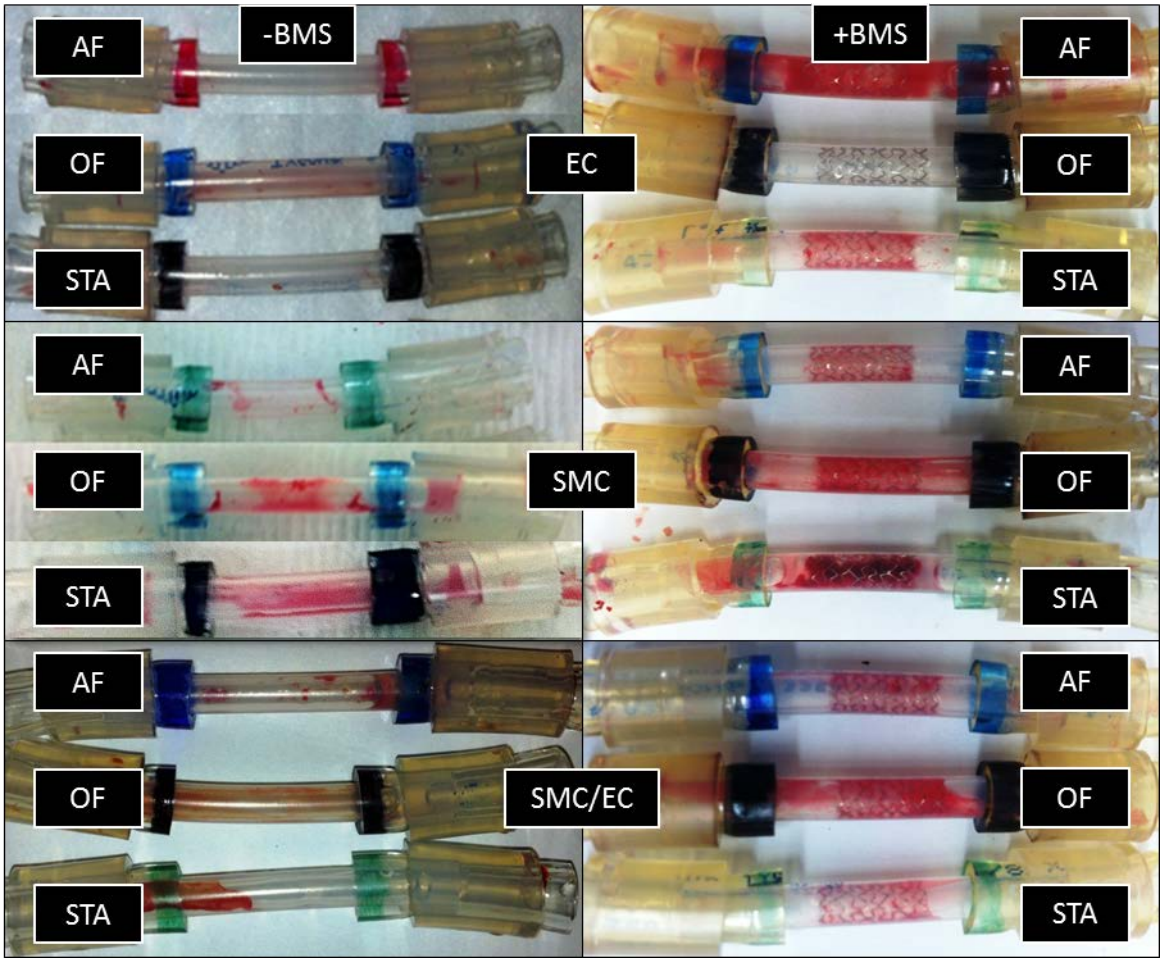

Figure 102 - Images of the thrombogenicity assays in EC, SMC or SMC/EC co-culture exposed to arterial flow (AF), oscillatory flow (OF) or static controls (STA) and injured with a metal stent (BMS)

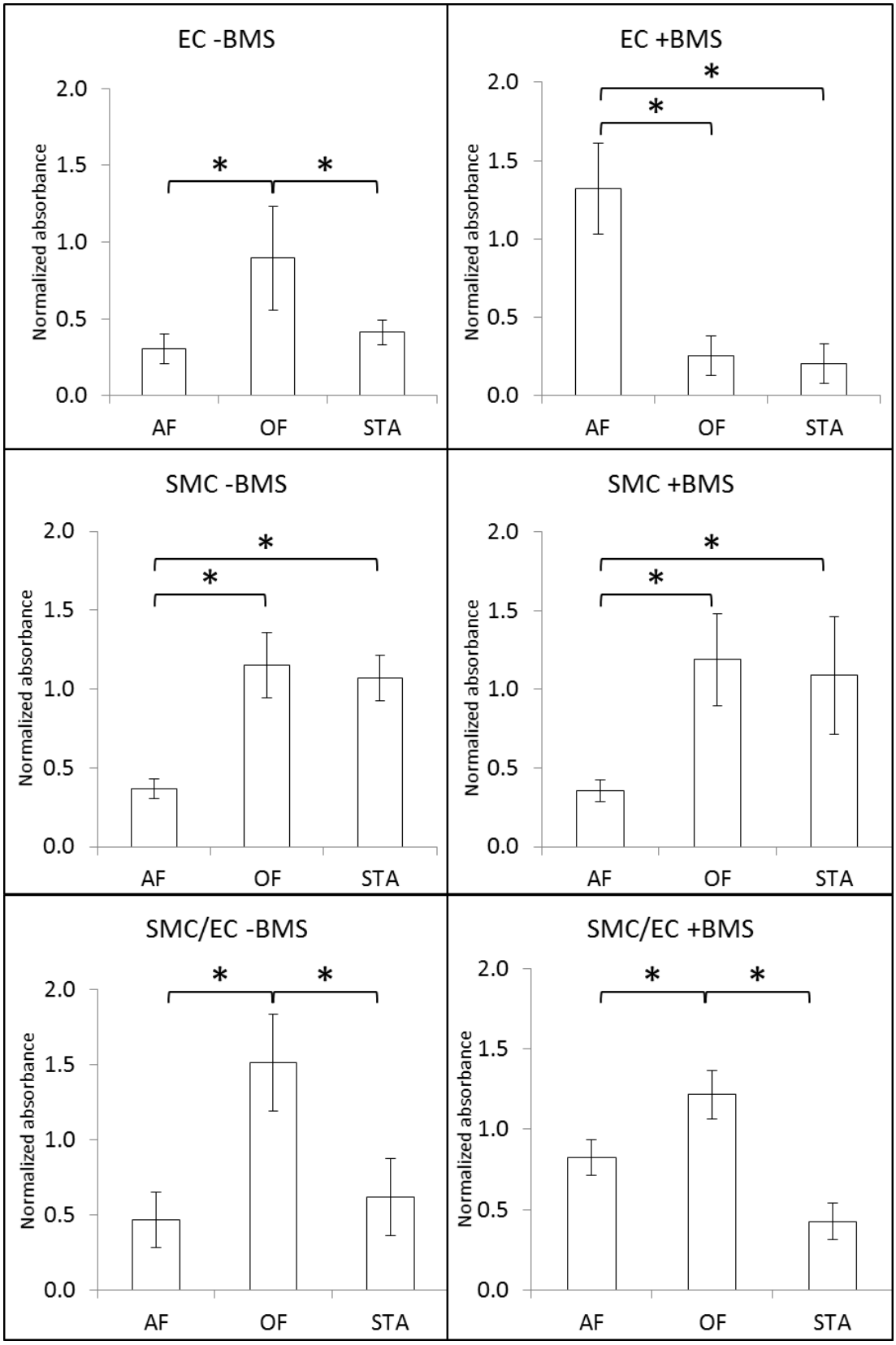

Figure 103 - Thrombogenicity assays in EC, SMC or SMC/EC co-culture exposed to arterial flow (AF), oscillatory flow (OF) or static controls (STA) and injured with a metal stent (BMS)

4.1.4 – Re-endothelialization

Stent re-endothelialization was evaluated in constructs coated with EC on top of SMC co-cultures that were injured with bare metal stents. After NIR stent deployment at 16 atm, the constructs were exposed to arterial-like flow, oscillatory flow or static condition for 24 hours. Stent injury was visually confirmed at time 0 (Figure 104, Figure 105) and the luminal coverage of the stent was evaluated after 24 hours of exposure to the different flow regimes (Figure 106). Data for the abluminal side (Figure 107) confirmed good apposition of the stent against the wall of the constructs. In parallel, total cellularization and the EC/SMC ratio was quantified. Finally, TF expressed by SMC populating the stent was also determined in the different scenarios (Figure 108). Re-cellularization of stents followed an interesting trend. Oscillatory flow had a 75% higher cellularization than the arterial flow and static cases (Figure 109). This may lead to think that OF benefits stent re-endothelialization and hence reduces thrombotic risk. Looking closely to the EC/SMC ratio (Figure 111), however, one observes that OF promotes SMC occupation of the stent strut. This directly leads to the effect observed in Figure 110. TF exposed to blood flow in the luminal side is the highest in oscillatory regimes. Furthermore, as seen in chapter 4.1.1, Figure 83, SMC exposed to OF showed higher TF expression. This increase in TF expression explains thrombogenicity results observed in chapter 4.1.3 (Figure 102 and Figure 103), in which co-cultured, stented constructs presented larger blood clots when exposed to oscillatory regimes. These results have direct impact in stent implantation: the majoritarian presence of SMC on the stent struts implanted in oscillatory regions can promote restenosis and thrombosis. Contrariwise, stent struts placed in regions of artery-like flow, although they might re-cellularize later, promote EC growth predominantly, reducing the risk of stent thrombosis and restenosis. In any case, if a stent

were to be placed in an oscillatory region, the indication would be to minimize endothelial damage to limit SMC (and hence TF) exposure to flow.

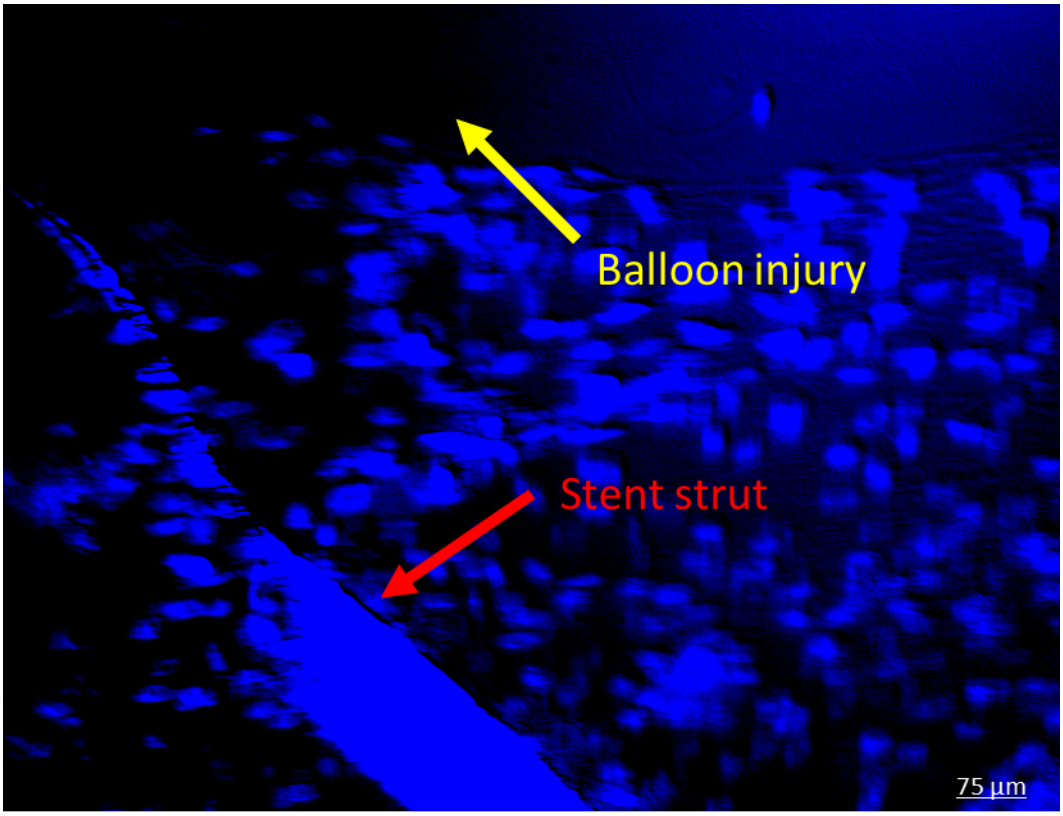

Figure 104 - Stent and balloon abluminal injury in EC/SMC (DAPI, blue) coated construct

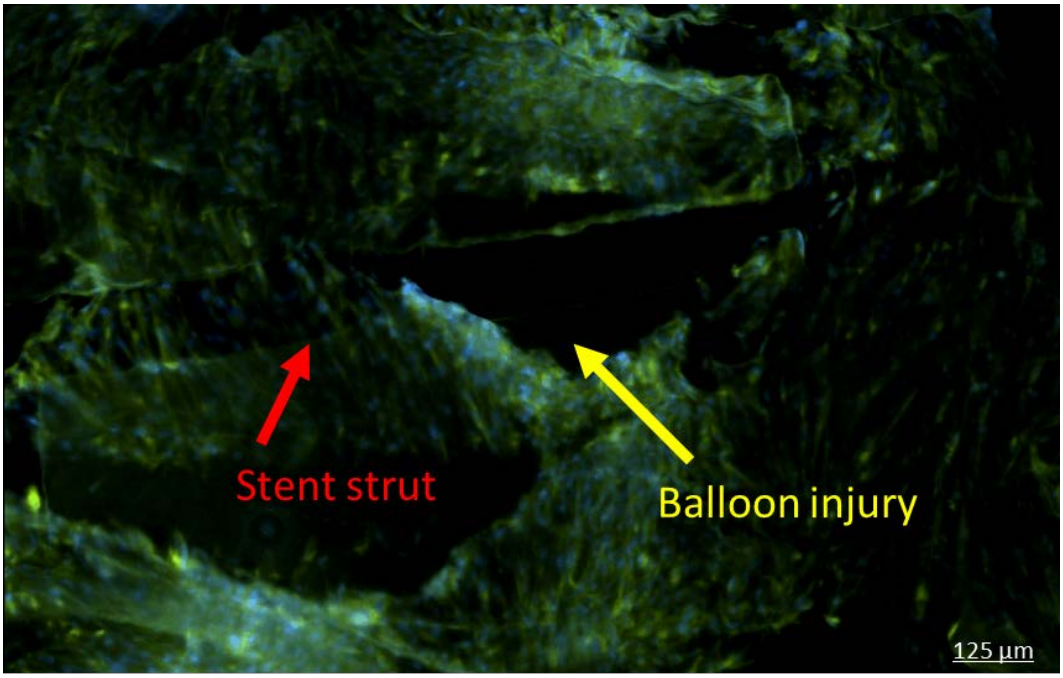

Figure 105 - 3D projection of a stent apposition on the abluminal side of an EC/SMC (DAPI, blue, TF, yellow) coated construct

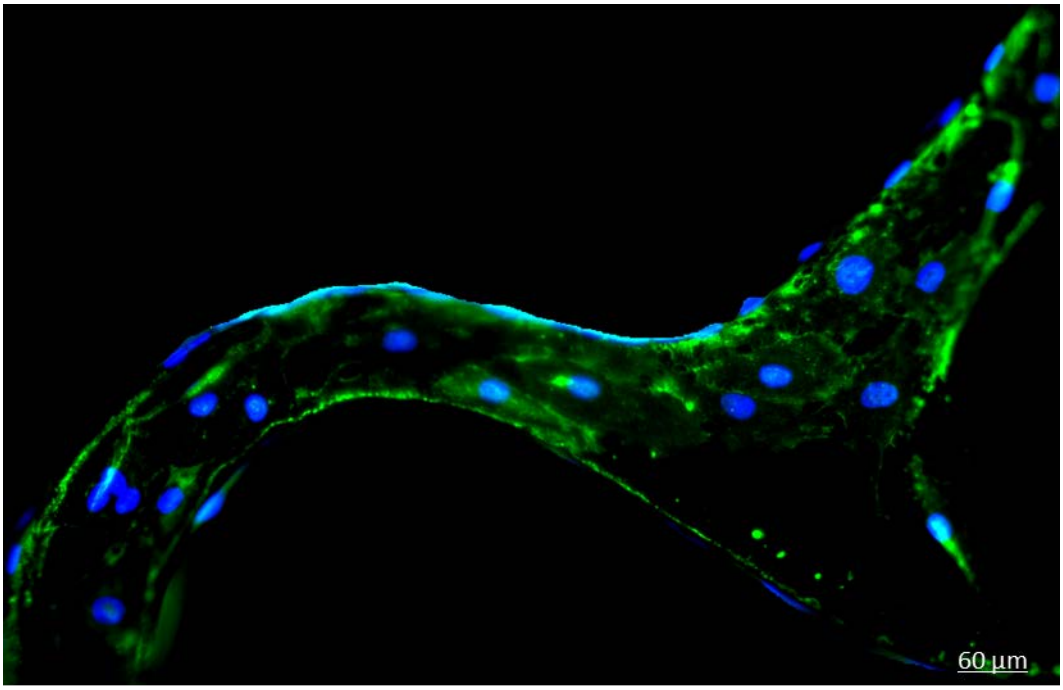

Figure 106 - Luminal side of a stent 24 hours after deployment in an EC/SMC (DAPI, blue, CD31, green) coated construct

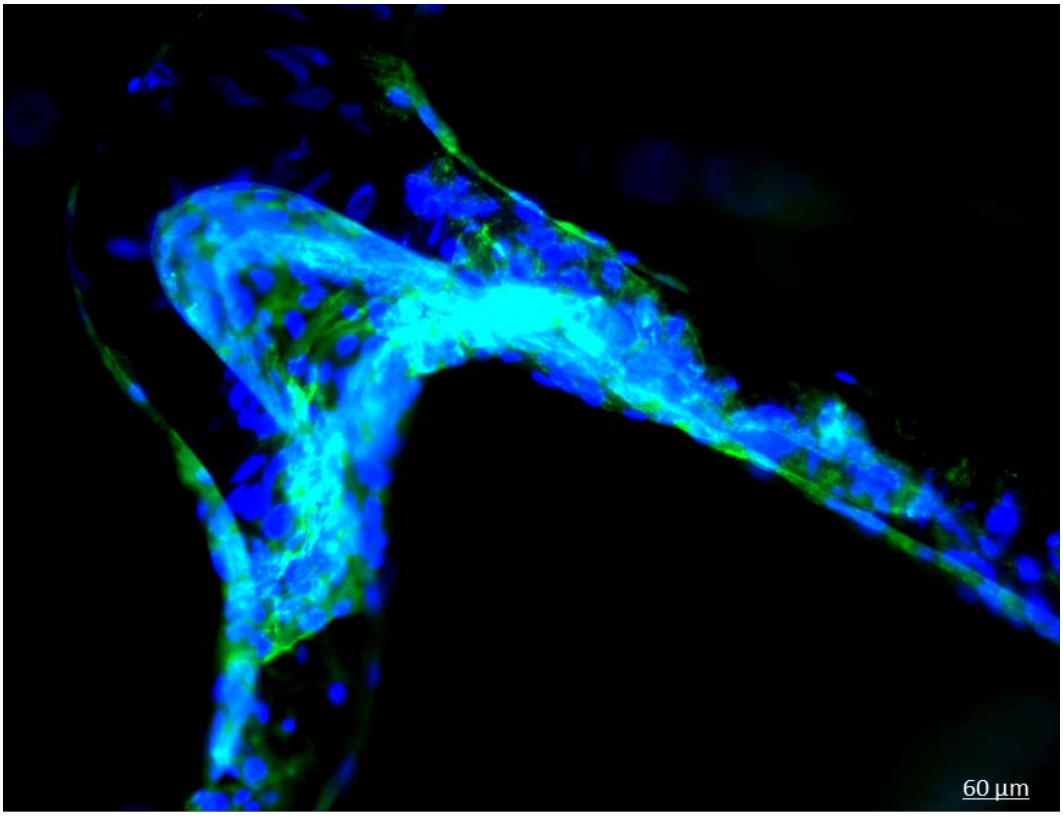

Figure 107 - Abluminal side of a stent 24 hours after deployment in an EC/SMC (DAPI, blue, CD31, green) coated constructs

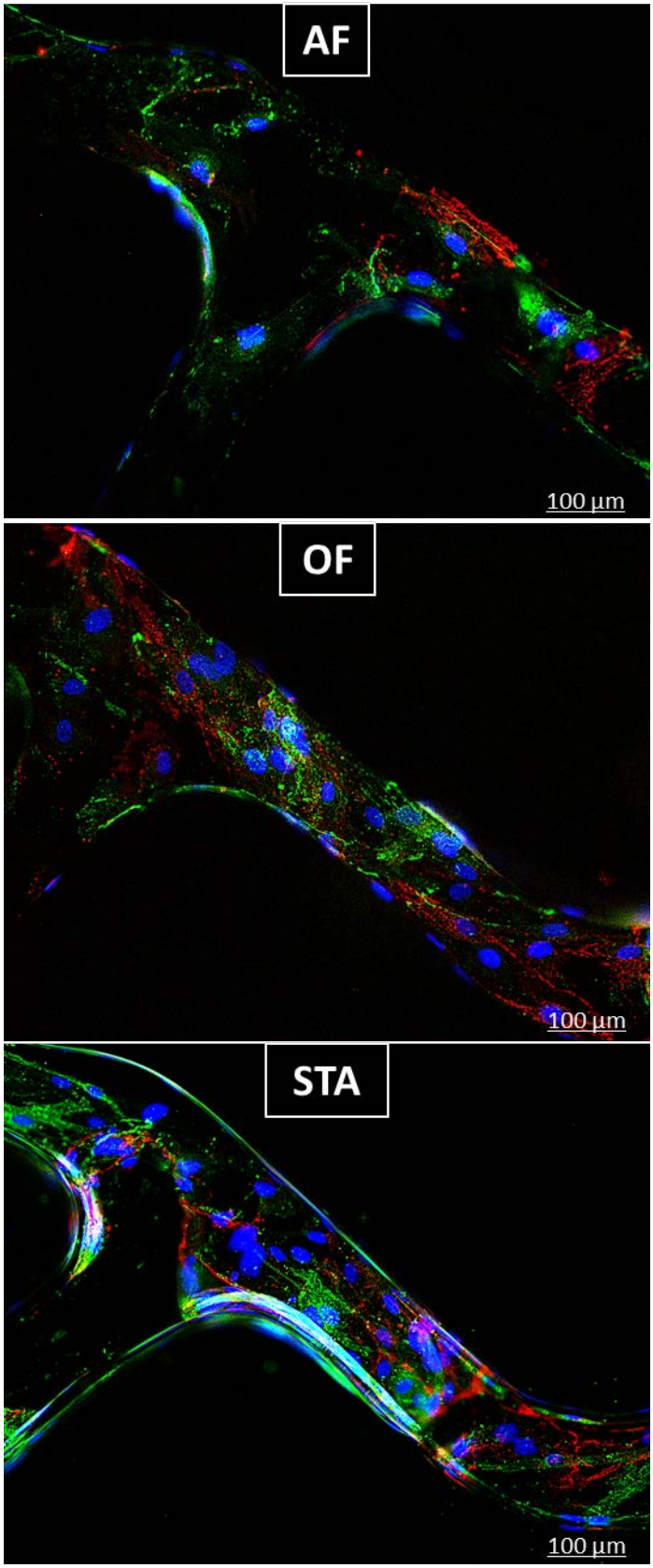

Figure 108 - Stent cellularization 24 hours after deployment in EC (CD31, green) / SMC (TF, red) coated constructs as a function of flow regime

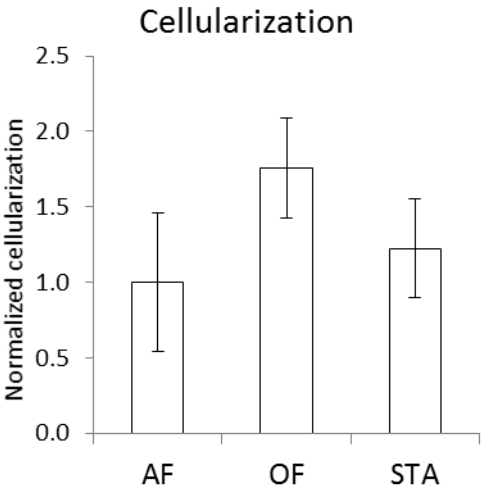

Figure 109 - Stent cellularization as a function of flow regime

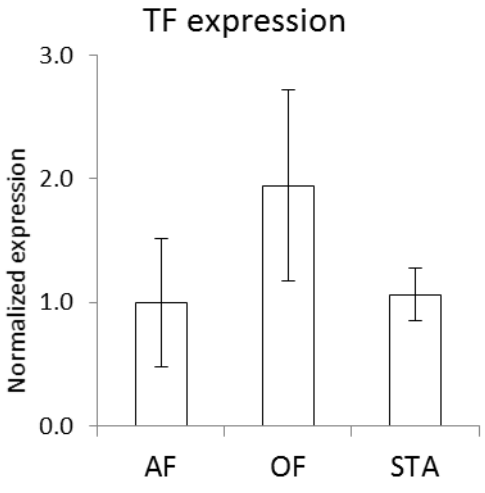

Figure 110 - TF expression of cells on the luminal side of the stent as a function of flow regime

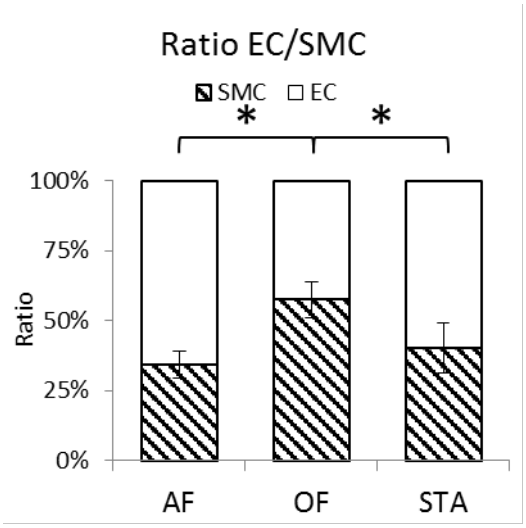

Figure 111 - Ratio EC/SMC on top of stent struts as a function of flow regime

4.2. – Uremia related risk factors

As described in chapter 1.4, uremic patients are at amplified risk of thrombosis when subject to stent implantation. This section will evaluate the effect of uremic milieu in thrombosis biomarkers such as TF expression and activity. As already seen in Figure 76, TF expression in quiescent EC is not in the detectability range while SMC is. Increased baseline SMC TF is consistent with the highest amount of clot formation observed in the SMC-coated flow loop tubes (Figure 100). In consequence, mono-cultured SMC, model of endothelial denudation after intervention, will be used to evaluate thrombosis biomarkers in uremic milieu.

4.2.1 – TF expression

SMC were exposed for 24 hours to 5% serum pooled from end stage renal diseases patients suffering from uremia in DMEM (uremic serum) and compared to SMC exposed to 5% serum pooled from healthy volunteers conditions in DMEM (control serum). Results revealed that uremic serum doubles TF expression in SMC when compared to control serum (Figure 112). Furthermore, TF localization is altered. TF is mainly located in the cellular membrane of untreated or exposed to control serum SMC. In the case of uremic serum, remarkably, TF is not only located in the cell membrane, but is also intense in the cell nucleus. On the one hand, one could think that TF in the cell membrane has migrated to the nucleus as observed in other proteins that signal proliferation[88, 102]. On the other hand, uremic serum may be causing high levels of TF translation at nuclear level and what is observed in the picture would be TF ready to traffic towards the membrane[54].

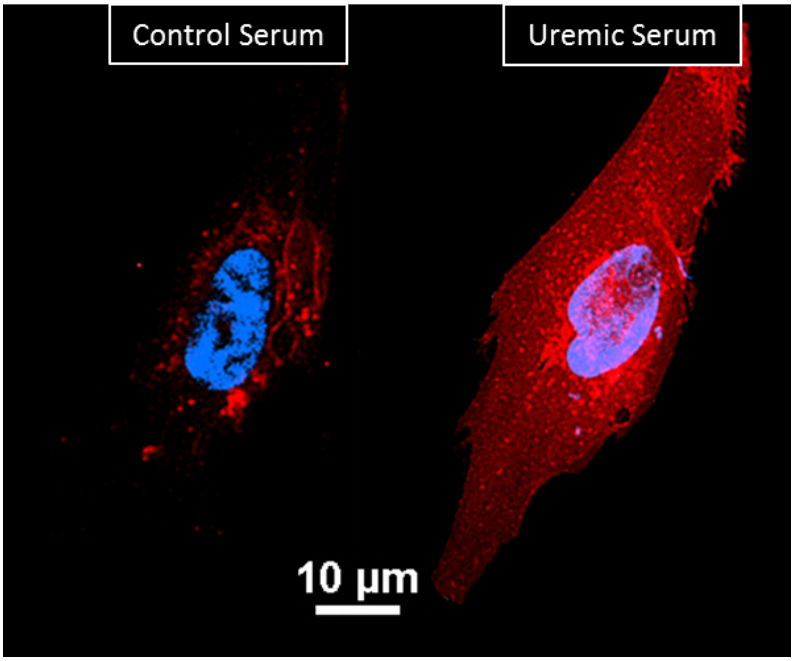

Figure 112 - TF expression in SMC exposed to control serum (left) and uremic serum (right)

Uremic solutes are the products of intermediate metabolism or retained proteins that failed to be fully excreted. The effect of a selected group previously linked to vascular dysfunction[103] of water soluble and protein-bound solutes in SMC TF expression was evaluated individually. Uric acid, the most significant water soluble solute, was evaluated with sodium hydroxide as a negative control (Figure 113). Among protein-bound solutes, indoxil acetate (IA), indoxil sulfate (IS) and homocysteine were chosen, with human serum albumin (HSA) as negative control. SMC were exposed for 24 hours to those solutes or their respective controls (Figure 114). While homocysteine had no significant effect on TF expression, uric acid, IA and

IS increased 2.3- to 3.5-fold compared to their respective controls. The mechanisms by which TF expression is higher in IA, IS and uric acid cases were further studied by Chitalia et al[43]. Briefly, IA and IS increased the stability of TF by interfering with its ubiquitination process, increasing TF levels. Potentially, their indole ring may be able to interfere in TF binding with its putative E3 ubiquitin ligase. The mechanism of UA-mediated TF regulation remains elusive. Uric acid did not significantly affect neither TF mRNA nor protein stability. It is possible that uric acid regulates TF translation or that it triggers an inflammatory response, indirectly regulating TF production. All of these possibilities warrant further investigation and prove the complexity of the effects of uremic solutes on TF regulation and are beyond the scope of this thesis.

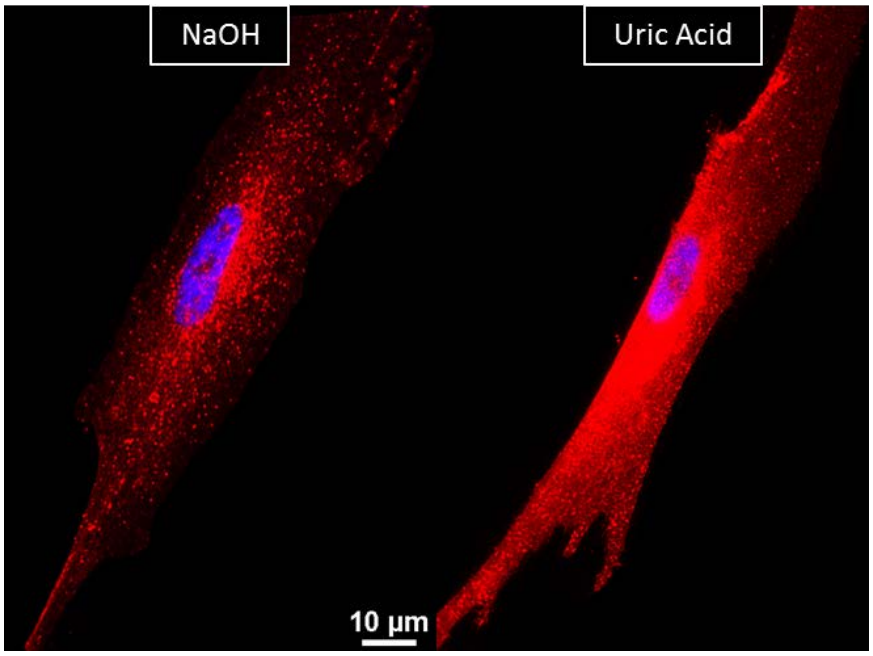

Figure 113 - TF expression in SMC exposed to sodium hydroxide (left) and uric acid (right)

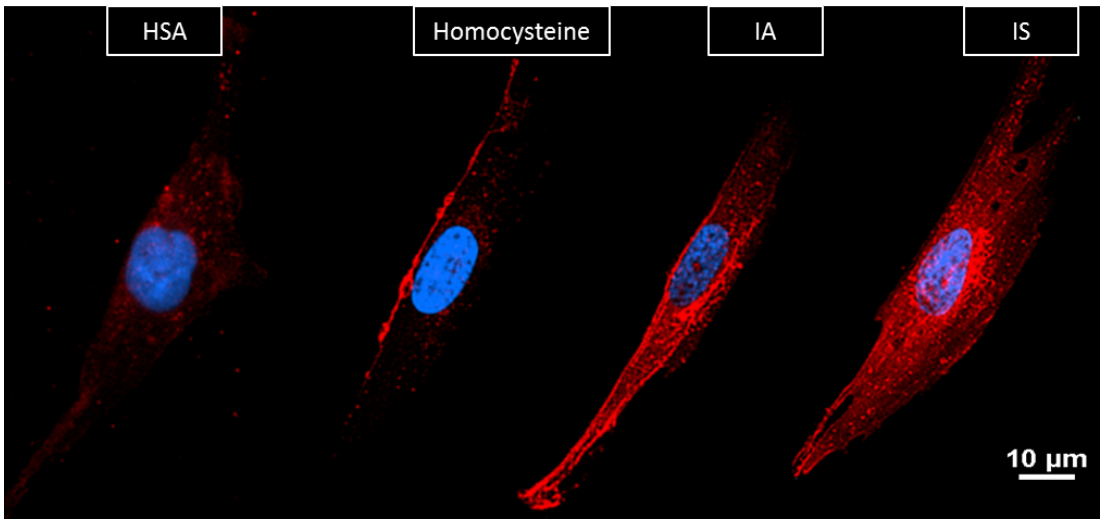

Figure 114 - TF expression in SMC exposed to different protein-bound solutes

4.2.2 – TF activity

The flow loop assay described in chapter 5.3 was used to determine thrombogenicity in straight tubes coated with SMC. Cells were exposed for 24 hours to uremic serum, uric acid, IA, IS or their respective controls, control serum sodium hydroxide (NaOH) or human serum albumin (HSA), respectively. In a second set of experiments, cells were exposed to the treatment (uremic serum, uric acid, IA, IS) and incubated for 1 hour with control antibody or anti TF antibody. Figure 115 shows examples of the different clots and Figure 116, Figure 117, Figure 118 and Figure 119 show the normalized hemoglobin levels for each experiment.

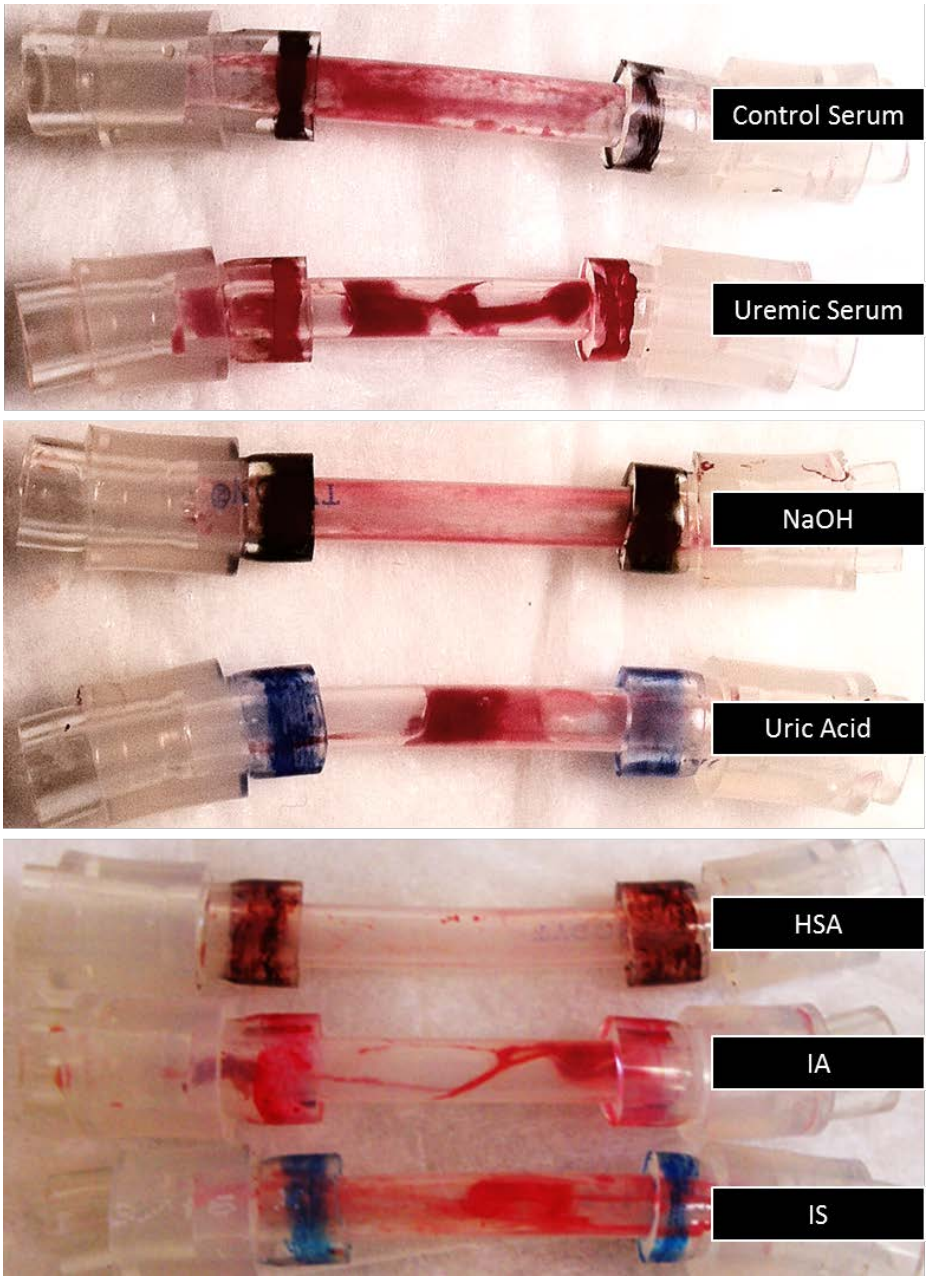

Figure 115 - Thrombogenicity in SMC-coated tubes exposed to uremic serum and uremic solutes

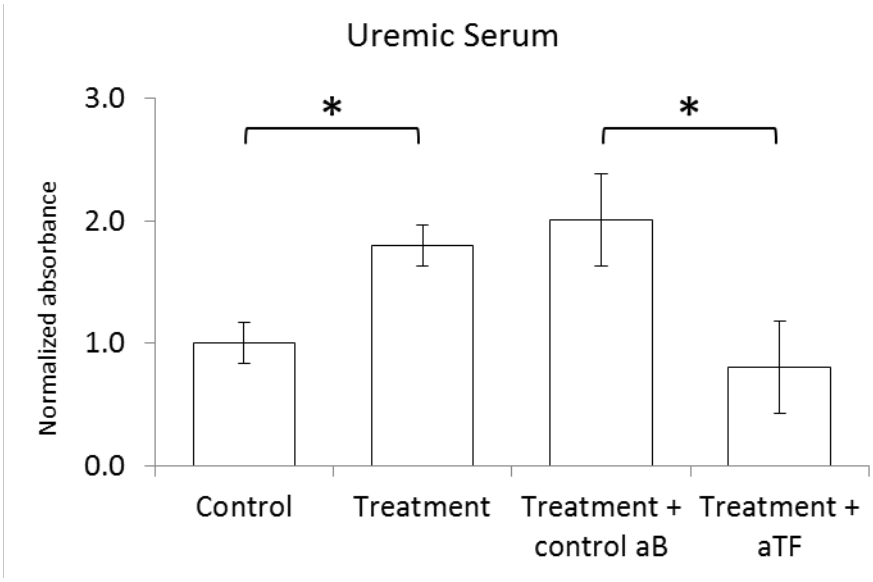

Figure 116 - Thrombogenicity of SMC exposed to uremic serum

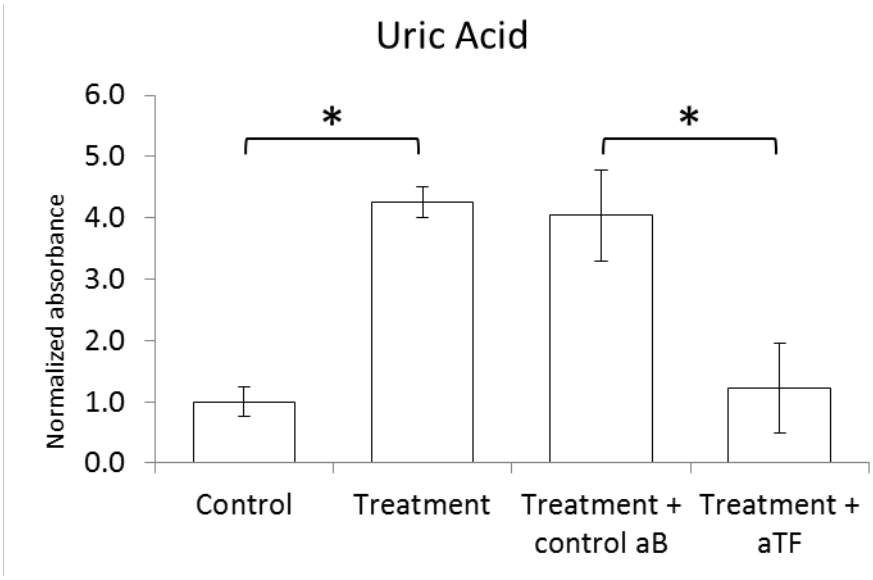

Figure 117 - Thrombogenicity of SMC exposed to uric acid

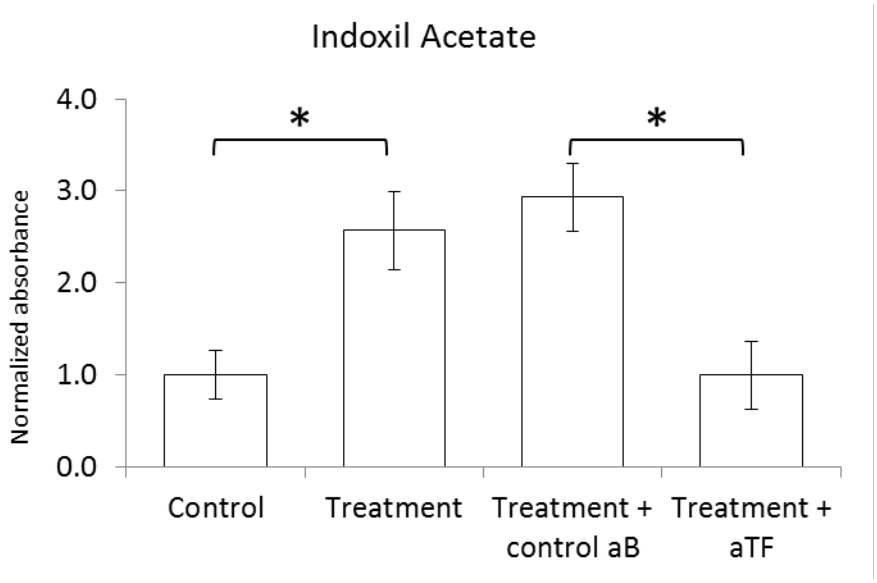

Figure 118 - Thrombogenicity of SMC exposed to indoxil acetate

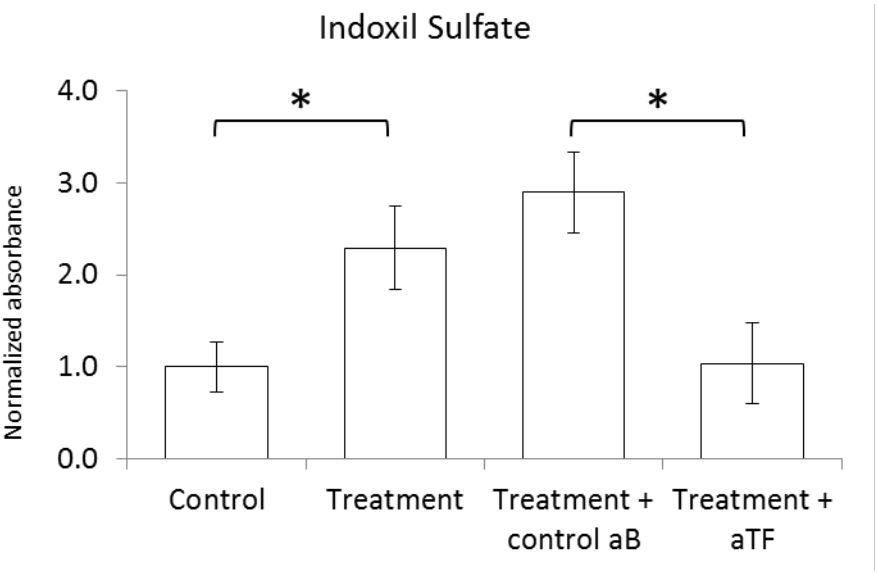

Figure 119 - Thrombogenicity of SMC exposed to indoxil sulfate

SMC-coated constructs were consistently more thrombogenic when exposed to uremic serum (2-fold increase), uric acid (4-fold increase), IA (2.5-fold increase) and IS (2.5-fold increase). These results are in accordance with those observed in Figure 112, Figure 113 and Figure 114, correlating TF increase with augment of thrombogenicity. To confirm that thrombogenicity was activated through the extrinsic coagulation pathway, the treated SMC constructs were incubated with control antibody or anti-TF antibody. The increase in thrombogenicity was muted as TF was blocked by the antibody, confirming the hypothesis that TF was responsible for the observed increases in thrombogenicity.

5 – MATERIALS AND METHODS

5.1 – Cell Culture

5.1.1 – Materials and reagents

CS: Calf Serum, mycoplasma tested, virus tested and endotoxin tested (Life Technologies, 16170-078, New Zealand)

Dextran: Dextran from Leuconocstoc mesenteroides (Sigma, D5376, US)

DMEM: Dulbecco's Modified Eagle Medium with low glucose with L-glutamine, 25mM HEPES buffer, 110mg/mL sodium pyruvate, pyridoxine hydrochloride (Life Technologies, 12320-032, US), with 5% CS and 1% PSG added and filtered with a 0.22µm filter to sterilize it.

EGM-2: Endothelial cell Basal Medium-2 bulletkit (Lonza, CC-3162, US) with FCS 0.02 mL/mL supplemented with EGF-1 5 ng/mL, bFGF 10 ng/mL, Long R3 IGF 20 ng/mL, VEGF-165 0.5 ng/mL, Ascorbic Acid 1 µg/mL, Heparin 22.5 µg/mL , Hydrocortisone 1 µg / ml, 5% FBS and 1% PS and sterile-filtered with a 0.22µm filter.

FB: Human aortic adventitial fibroblasts, cryopreserved cells (Cat. No. C-12380, Promocell, Germany)

FBS: Fetal Bovine Serum (Life Technologies, 26140-079, US)

Fn: Fibronectin from bovine plasma (Sigma-Aldrich, F4759, US)

SMC: Human Aortic Smooth Muscle Cells, cryopreserved cells (Cat. No. PCS-100-012, ATCC, US)

EC: Human Coronary Artery Endothelial Cells, cryopreserved cells (Cat. No. C-12221, Promocell, Germany)

PBS: Phosphate Buffer Saline, pH 7.4 at 25ºC (Life Technologies, 70011-044, US)

PS: Penicillin10000 units/ml penicillin G sodium with Streptomycin 10 mg/mL streptomycin sulfate in 0.85% NaCl (Life Technologies, 25030-081, US)

PSG: PS with L-glutamine-200mM, 29.2 mg/mL in 0.85%NaCl (Life Technologies, 25030-081, US)

TRYPSIN: 0.05% Trypsin in 0.53mM EDTA (Life Technologies, 25300-054, US)

NIR Stent: Stent NIR® ELITE 15 mm x 3.5 mm, 7 cell, 316 stainless steel (Medinol, Product Number NIR® Elite OTW H7493486015350, US)

Cordis BMS: Cordis® Bx Velocity Stent, 18mm x 3.5 mm

Cordis DES: Cordis® Cypher Stent, 33mm x 3.5 mm, sirolimus-eluting stent

5.1.2 – Equipment

COULTER COUNTER: Particle counter and size analyzer, Coulter Z2 (Coulter Corporation, US)
CENTRIFUGE: G9095 IEC Model CL Centrifuge (IEC, US, 428). Rotor 215: 4x50ml, RCF 1750 g, Max Speed 3350rpm
OM: Optical Microscope, Nikon Diaphot inverted tissue culture microscope
FM: Fluorescence Microscope, Nikon Eclipse TE epifluorescence microscope coupled to a Hamamatsu CA 4742-95 camera
CM: Confocal Microscope, Perkin-Elmer spinning disk confocal system coupled to a Zeiss Axiovert 200M microscope and a Hamamatsu Orca ER camera

5.1.3 – Cell culture on plates

Cryopreserved human coronary artery endothelial cells (EC), human aortic smooth muscle cells (HASMC) and human aortic adventitial fibroblasts (FB) were thawed, seeded, grown and passaged onto 100mm tissue culture polystyrene plates (TCP100) as follows. The same procedure was followed for each cell type. 10 mL of previously warmed EGM-2 for EC and FB or DMEM for SMC were poured into a TCP100. Then, a 2mL cryovial containing about 1.3 million cells was thawed in the water bath at 37ºC for less than 2 minutes and poured in the TCP100. The TCP100 was placed in the 37ºC incubator, at 5% CO_2. After 4-5 hours, the attachment of the cells was visually confirmed under the optical microscope and culture medium was replaced with 10mL of fresh medium. Every 2-3 days, culture medium was replaced by 10mL fresh medium, visually checking cells' health under the optical microscope; culture plates were kept in humidified incubator while not being manipulated. Once the cell surface coverage reached 95% of the plate, cells were passaged in a ratio 1:3 to continue with their culture. Supernatant was removed and cells were rinsed with 10mL PBS. After aspirating off PBS, 3mL of Trypsin were poured on the cells and incubated during 5 minutes. Then, 7mL of DMEM were added to the plate in order to neutralize the effect of trypsin. The content of the plate was transferred into a 50mL Falcon® tube, and the plate was rinsed with additional 5mL of DMEM, transferring again the content of the plate into the same tube. The cell suspension was centrifuged for 5 minutes at 2000 rpm and then the supernatant medium was removed, keeping only the cell pellet. The pellet was resuspended in 30mL of corresponding medium and split into three new TCP100.

5.1.4 – Cell culture on tubes and constructs

Flow experiments required culturing cells on the luminal surface of tubes or bifurcated constructs. After culturing enough cells for the experiments (≈2-5 million cells/TCP100), cells were seeded and cultured on straight tubes and bifurcations following the procedure detailed below. Prior to cell seeding, tubes or constructs were washed in 0.2% SDS for 20 minutes, rinsed twice with distilled water for 20 minutes and autoclaved. Tubes were coated with 100 (straight tube, coronary bifurcation) or 150µg/ml (carotid bifurcation) fibronectin (Fn) in PBS overnight at 4ºC. A cell suspension was prepared as described above and resuspended at 1 million cells/mL. FB, SMC and EC were sequentially layered with 48h of difference between strata. In order to ensure homogeneous distribution of cells along the inner surfaces of tubes and bifurcations, tubes and constructs were placed in a cylindrical, 25cm diameter rotator turning at 3 rpm inside a 37ºC, 5% CO_2 humidified incubator. After this process, tubes or bifurcations were ready to be stented (if necessary) and subsequently connected to a perfusion bioreactor.

5.1.5 – Stenting

Before exposure to flow, some experiments required stenting the cell-seeded constructs (Figure 120). A catheter with a 3.5mm-wide, 16mm long NIR® elite stent mounted on an inflatable balloon was introduced through the construct. The balloon was inflated at 16 gauge atm, so the deployed stent remained well apposed on the silicone construct (Figure 121). The balloon was then deflated to -0.5 gauge bar and the catheter retrieved.

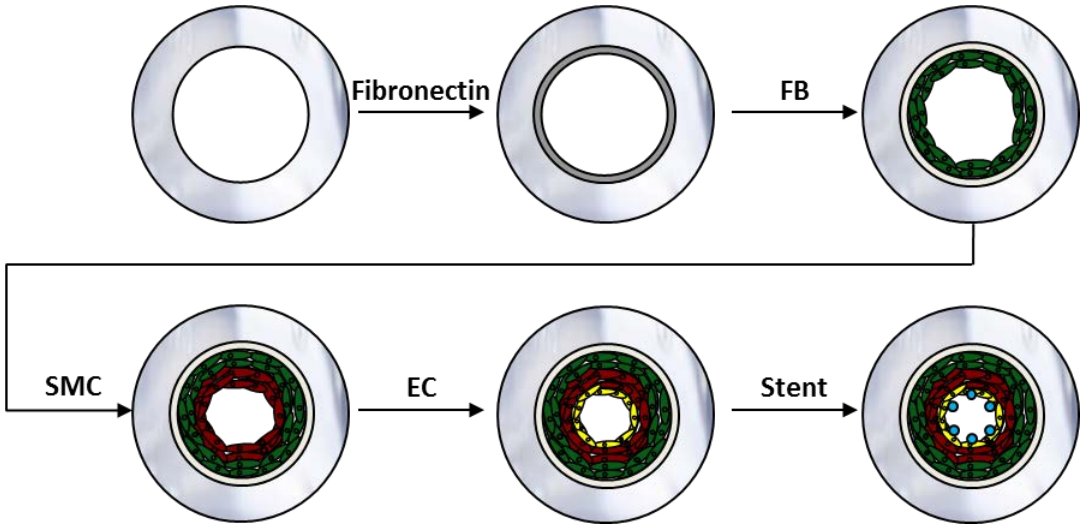

Figure 120 - Overall vessel-like seeding and stenting process

Figure 121 - Stented straight construct

5.2 – Perfusion Bioreactor

The perfusion bioreactor is a flow delivery system designed to provide the tubular constructs with any flow type (steady, pulsatile, oscillatory) and to enable study of how cells react to different flow stimuli. It was designed coupled to a humidified incubator (37ºC, 5% CO_2) where tubing and cell-seeded constructs are placed and connected to flow. Flow is driven by analogic pumps consisting of a digital drive (Cole Parmer, EW-78002-00) and a pump head with 12 channels and 8 rollers (Cole Parmer, EW-78002-36). A program in LabView® previously created by Dr. Peter Wu generated an electrical signal adjusted with a customized manual control to generate the desired flow waveform. Only the pump drive was placed outside the incubator, while pump head and tubing remained inside. The original incubator by Thermo Scientific had to be modified to connect the pump heads to the tubing system. Holes were drilled to allow the pump's transmission through the water jacket until the pump head. The modifications were designed using Autocad® and Thermo Scientific executed the proposed modifications. Similarly, the trays were redesigned to allow space for the pump head and proper positioning of the reservoirs. The setup used to propel flow through the construct differed as a function of the type of construct studied. Generally (Figure 122), the reservoir was connected to a 10-cm long 4.78 mm ID Silastic® tube (Dow Corning – Cat No. 515-013) and attached to two-stop pump Pharmed BPT tubing, ID 2.79mm (Cole-Parmer, 95713-48) with 1/8" ID straight connectors (Cole-Parmer 30703-02). For carotid constructs (Figure 124), the system was divided into four channels so the pump delivered four times the maximal flow and merged into a single channel before entering the cell-seeded construct. After flowing through the carotid scaffold, medium returned to the reservoirs by merging the two outlets. 3.18 mm ID Silastic® tubes (Dow Corning – Cat No. 515-012) and Y connectors (Cole Parmer – Cat No. EW-40727-41) were used. For coronary constructs (Figure 125) and straight tubes (Figure 123), the system used a single two-stop pharm tube to reach the flow rates and the systems followed the schemes in (coronary) and (straight tube). The static loops were 15 cm-long 4.78 mm ID Silastic® tubes connecting both extremes of the cell-seeded construct. Straight vessel-like constructs and bifurcated constructs were connected to the perfusion bioreactor as seen in Figure 123, Figure 124 and Figure 125. Straight tubes were exposed to coronary artery–like flow, oscillatory flow or static conditions. AF was 1-Hz pulsatile flow of 17 dyne/cm^2 maximal shear stress and OF was 1Hz oscillatory flow of 5 dyne/cm^2 maximal shear stress. In the coronary model, medium flowed at 1 Hz pulses with 17 dyne/cm^2 maximal shear stress. In the carotid model, flow pulsed at 1 Hz with 12 dyne/cm^2 maximal shear stress.

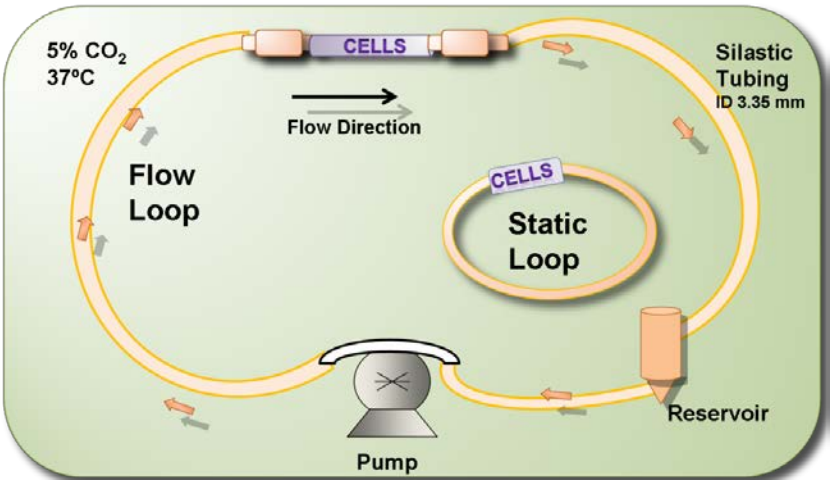

Figure 122 - General connection scheme of the bioreactor

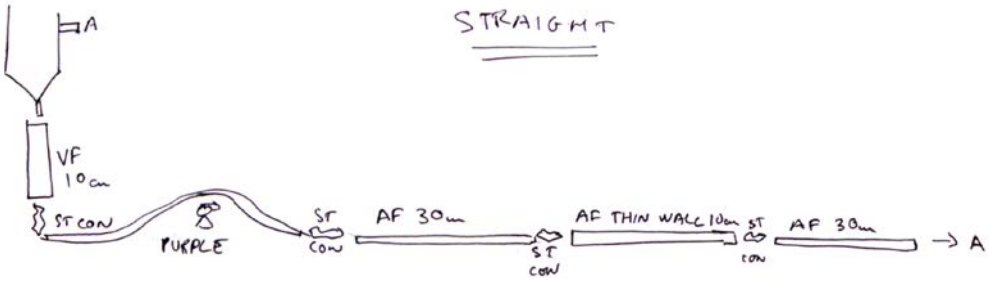

Figure 123 - Straight tubes connection scheme

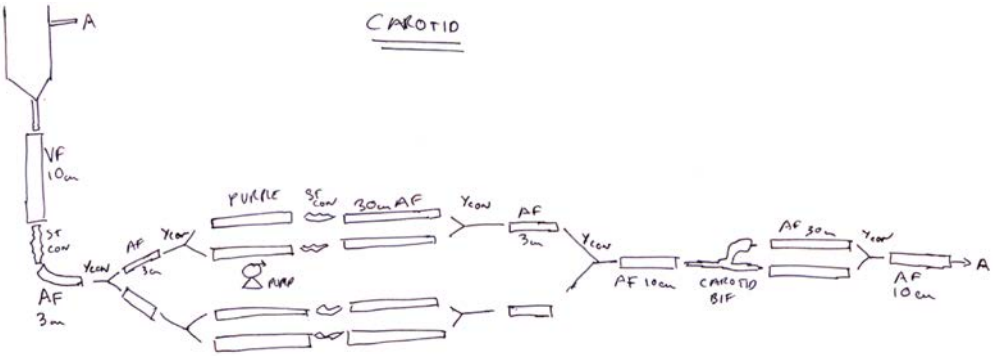

Figure 124 - Carotid constructs connection scheme

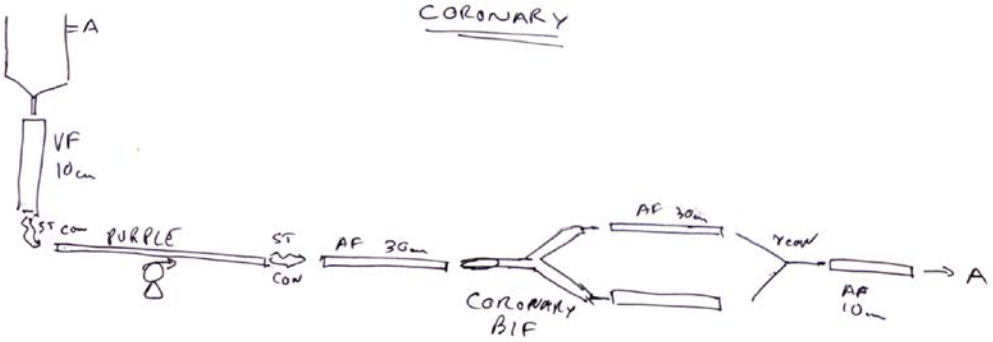

Figure 125 - Coronary constructs connection scheme

5.3 – Thrombogenicity device

A modified Chandler loop evaluated endovascular device thrombosis. Motor-controlled rotors accelerate blood-filled flow loops (Figure 126), generating pulsatile flow simulating coronary-like hemodynamics (peak flow, 100 mL/min). A flow loop consisted of 4 cm-long, 1/8" ID Tygon® 3350 tubes (Saint-Gobain, France) coated with vascular cells (prepared and seeded as described in chapter 5.1.4). The loop was subjected to a coronary flow condition that emulates the endovascular intervention ex vivo and serves as a screening tool to examine thrombosis in various vascular beds. Before cell seeding, Tygon® tubes were cleaned and autoclaved and injected with one million cells/mL of SMC or EC into fibronectin-coated tubes and cultured for 48 hours under axial rotation at 10 rph, 37°C, 5% CO2. Cell seeded tubes were exposed to different arterial flow types or kept static (no flow) as control or when evaluating the effect of uremic serum and uremic solutes. The exposure time for the different stimuli was always 24 hours. The segments were explanted, gently flushed to remove the media, and positioned in the reactive site flow loop model as seen in Figure 127.

Fresh whole blood was collected from healthy volunteers in a 10% acid/citrate dextrose solution (0.085 M trisodium citrate, 0.069 M citric acid, 0.111 M glucose, pH 4.6). Immediately before testing, a 0.1 M $CaCl_2$ and 0.075 M $MgCl_2$ solution was added to the blood (70-µL solution per 1 mL blood) and loaded into the flow loops. After 10 to 15-minute runs, loops were emptied and flushed with 60 mL Tyrodes buffer (0.01 M HEPES, 0.75 M MgCl2) to remove non-adherent material. After visual assessment, the clot was lysed with 1% Triton-X solution for 20 minutes. Lactate dehydrogenase and hemoglobin were measured with the use of Quantichrome heme assay and Cyto-Tox 96 nonradioactive cytotoxicity assay (Promega) as measures of erythrocyte content and total clot mass, respectively.

TF neutralizing assay was performed as follows. After SMC-coated tubes were exposed to uremic serum or uremic solutes for 24 hours, the constructs were treated with isotype control antibody anti-Iba1 (Santa Cruz Biotechnology) or anti-TF neutralizing antibody (50 µg/mL) (American Diagnostica) for 1 hour at 37ºC and 5% CO_2 before the flow loop experiment.

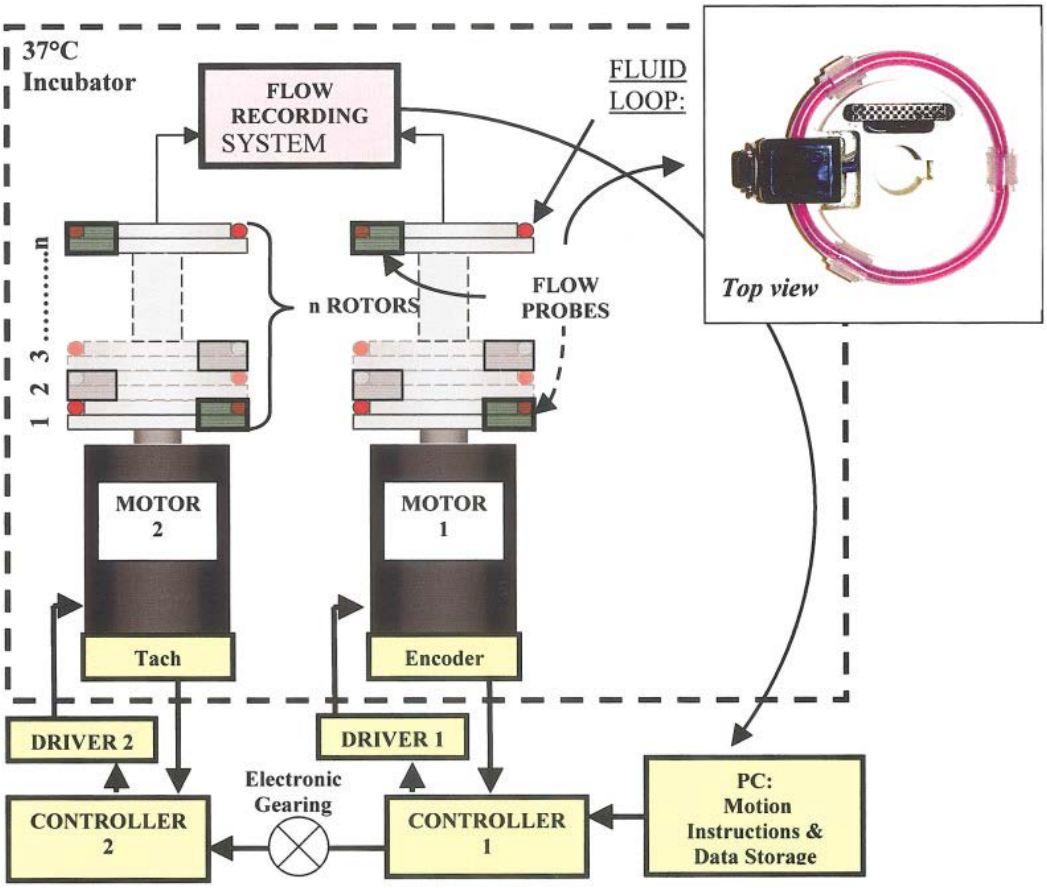

Figure 126 - General two-axis system schematic and fluid loop design[75]

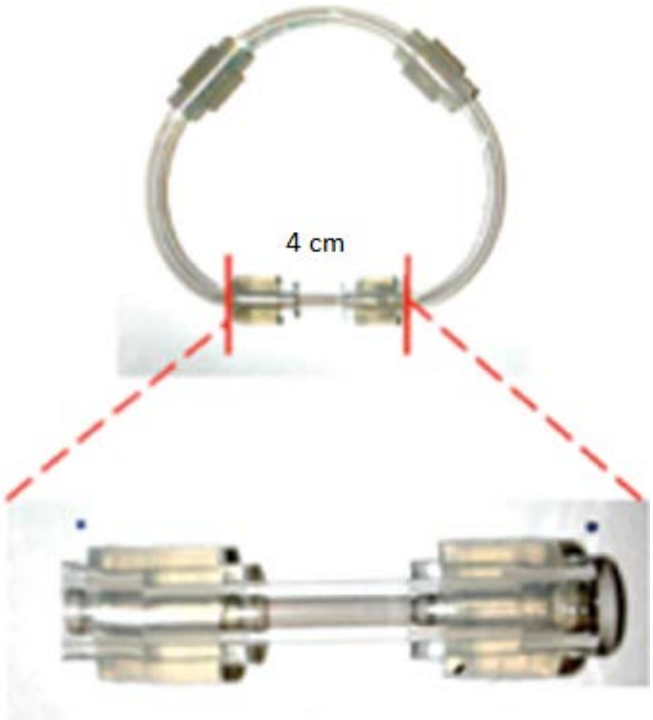

Figure 127 - Close-up of the flow loop and the reactive site[76]

5.4 – Monocyte isolation and adhesion

Fresh blood was drawn from healthy male subjects (Blood research components) and shipped with 10% EDTA. The blood was mixed 1:1 with a PBS/EDTA solution (0.5 M EDTA in PBS) and homogenized. The blood/PBS/EDTA solution was very carefully layered onto the same amount of Histopaque 1077 (Sigma) in order to avoid the mixing of the two liquids. The resultant bilayered tube was centrifuged at 400g for 30 minutes at room temperature. The result of the centrifugation is shown in Figure 128.

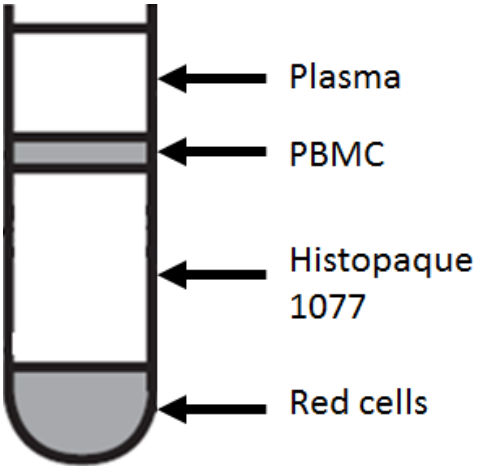

Figure 128 - Blood/PBS/EDTA/Histopaque 1077 mix after centrifugation

After centrifugation, supernatant plasma was carefully aspirated and discarded. With a pipette, the peripheral blood mononuclear cells (PBMC) – typically 5 mL – were transferred into another centrifugation tube and 10 mL of EDTA/PBS were added. This tube was spun at 400g for 10 minutes and the supernatant was discarded. The pellets from every tube were gathered by resuspending them in the same 10 mL of PBS/EDTA. The concentration of mononuclear cells was evaluated by cell counting and the suspension was centrifuged again for 10 minutes and concentrated. Monocytes were isolated from PBMC by negative selection. Non monocytes were magnetically labeled with a cocktail of biotin-conjugated antibodies that were recognized by an anti-biotin antibody conjugated to magnetic beads (Miltenyi Biotec).

The concentrated pellet of mononuclear cells was dissolved in a mix of 1 µL blocking reagent/million PBMC, 1 µL primary antibody/million PBMC and 30 µL of PBS/EDTA/iFBS (1% inactivated FBS in PBS/EDTA). After vortex and 10 minutes of incubation 4 °C, 2 µL secondary antibody/million PBMC were added to the mix. After vortex, the mixture was incubated for 15 minutes at 4 °C. Cells were subsequently washed with 10 mL of PBS/EDTA and centrifuged at 400 g for 10 minutes. The supernatant was discarded and the pellet was resuspended in 1 mL of PBS/EDTA/iFBS. A magnetic column (MACS) was placed on the magnetic support and equilibrated by rinsing it with 1 ml PBS/EDTA/iFBS). The cell suspension was ran through column twice and the eluent containing the isolated monocytes was recollected at the bottom. The column was washed with 500 µL of PBS/EDTA/iFBS and the entire effluent of the washing steps was gathered and mixed with the monocyte solution. After counting, isolated

monocytes were mixed with EGM-2, injected in the tissue culture plates or constructs at a density of 1 monocyte/endothelial cell and incubated at 37ºC and 5% CO_2 for 2 hours. EC within the tubes or constructs had previously been exposed to medium supplemented with TNF-α for 24 hours. Thereafter, the constructs were rinsed with PBS, fixed and stained for α-tubulin and DAPI. Fluorescent images were obtained at 405nm and 640nm. The ratio of adhered monocytes was quantified by analyzing the obtained IF images.

5.5 – Microscopic examinations

For IF, tissue culture plates or constructs were rinsed with PBS and fixed with 4% paraformaldehyde for 30 minutes at room temperature. Excessive aldehydes were quenched with 0.2M glycine in PBS for 10 minutes and, after washing with PBS, cells were permeabilized with 0.2% X-100 Triton in PBS. After two consecutive washes with PBS for 10 minutes and 1 hour blotting with 5% goat serum in PBS-BSA (PBS, 1% bovine serum albumin), cells were labeled overnight at 4^0C with their respective antibodies, generally diluted 1:50 in PBS-BSA. Cells were rinsed twice with PBS-BSA for 10 minutes and stained with the appropriate secondary antibodies and DAPI solution (1:100 in PBS-BSA) for 2h. Two additional 10 minutes washes with PBS were performed to remove any unbound antibody. Specimens were imaged using a Nikon Eclipse TI-E epifluorescence microscope or a Perkin-Elmer spinning disk confocal system coupled to a Zeiss Axiovert 200M microscope. The list of antibodies used is detailed in chapter 5.7.

For SEM, cells on constructs were first fixed in 3% glutaraldehyde, rinsed with PBS and subjected to a series of dehydration steps, which included 30 minutes incubations in ethanol solutions of increasing content in ethanol (50, 70, 95 and 100%) and 1h in acetone. Specimens were air dried overnight, sputter coated for 45s using a Denton (Mooretown, NJ) Vacuum Desk II Sputter Coater and imaged with a Hitachi (Tokyo, japan) S-3400N scanning electron microscope.

For H&E, cells on constructs were fixed in 4% PFA and subjected to a series of infiltration steps, which included 24 hours incubations in Spurr's resin (Electron Microscopy Sciences, Hatfield, PA) solutions in ethanol solutions of increasing content in Spurr's resin (25, 50, 75, 95, 100%). The resulting blocks were sampled and micro ground using an EXAKT 400CS Micro Grinding System (EXACT, Norderstedt, Germany) progressively until a 70-80 µm thickness. The samples were finally observed using an optical microscope.

5.6 – Radioimmunoprecipitation assay (RIPA) and western blot analysis

Non-specific cell lysis was performed by rinsing cell-coated constructs twice with ice cold PBS and then incubating them for 30 minutes on ice in radioimmunoprecipitation assay buffer containing 50 mM Tris-HCl, pH 7.4, 150 mM NaCl, 1% NP-40, 0.5% sodium deoxycholate, 0.1% SDS and 5 mM EDTA. The supernatant was extracted after centrifugation for 30 minutes at 13000 g and 4ºC, and mixed with 1:4 v/v of Laemlli's buffer (Boston Bioproducts) with 8% mercaptoethanol (Sigma). 10% acrylamide gels (Life Technologies) were used for protein separation. Gels were blotted using Life Technologies gel transfer stacks and blotting system. Membranes were blocked with 5% powdered milk and incubated overnight at 4^0C while shaking with the antibodies of interest diluted at their optimal concentration. After two washes with PBS-T (PBS, 0.05% Tween20, Sigma), membranes were incubated with appropriate HRP-conjugated secondary antibodies diluted 1:2,000 for 1h while shaking at room temperature. After two 10 minutes washes in PBS-T, Luminata™ Forte Western HRP Substrate (Milipore) was applied and luminescence was detected in a Chemidoc XRS+ (Bio-Rad). Densitometry plots were analyzed using ImageJ (NIH).

5.7 – Antibodies

Table 2 and Table 3 summarize the primary and secondary antibodies used for immunofluorescence (IF) and western blot (WB) and their respective dilutions.

Primary antibodies	IF dilution	WB dilution
Mouse monoclonal anti-CD106 (Santa Cruz Biotechnology)	1:50	1:50
Mouse monoclonal anti-TF (Sekisui Diagnostics)	1:50	1:1000
Mouse monoclonal anti-α-smooth muscle cell actin (Sigma)	1:50	N/A
Rabbit polyclonal anti-CD31 (abcam)	1:50	N/A
Rabbit polyclonal anti-CD54 (Cell Signaling)	1:50	N/A
Rabbit polyclonal anti-Ki67 (abcam)	1:50	N/A
Rabbit polyclonal anti-α-tubulin (Santa Cruz Biotechnology)	1:50	1:200
Rabbit polyclonal anti-cytoglobin (Santa Cruz Biotechnology)	N/A	1:200

Table 2 - Primary antibodies used in IF and WB

Secondary antibodies	IF dilution	WB dilution
Alexa Fluor® 488 goat anti-mouse IgG (H+L) (Life Technologies)	1:100	N/A
Alexa Fluor® 488 goat anti-rabbit IgG (H+L) (Life Technologies)	1:100	N/A
Alexa Fluor® 568 goat anti-rabbit IgG (H+L) (Life Technologies)	1:100	N/A
Alexa Fluor® 647 goat anti-mouse IgG (H+L) (Life Technologies)	1:100	N/A
Alexa Fluor® 647 goat anti-rabbit IgG (H+L) (Life Technologies)	1:100	N/A
HRP goat anti-mouse IgG (H+L) (Bio-Rad)	N/A	1:2000
HRP goat anti-rabbit IgG (H+L) (Bio-Rad)	N/A	1:2000

Table 3 - Secondary antibodies used in IF and WB

5.8 – ELISA and TF activity assay

The ELISA KIT 845 from Sekisui Diagnostics was used to determinate soluble TF in static experiments. The Human TF Activity Kit from Assaypro was used to determinate TF activity. After each experiment, culture medium was collected; cells were rinsed with PBS, detached with trypsin and counted using the Cell Counter. The collected medium was poured into Millipore® Centriplus 15 mL filters (10 kDa) and centrifuged for 30 minutes. One can easily obtain 1:10 dilutions with this method without drying the sample or losing signal quality. The medium outside of the filter was recovered and the medium inside was discarded; the medium able to go through the filter did not include TF (47 kDa) while the fraction that had not been through the filter contained TF more concentrated than initially. Initial and final volumes were computed to calculate concentration factor. Samples were collected and the standards were prepared. Remaining medium was stored at -80°C.

For the ELISA kit, 100 µL of TF standard or sample was added to each pre-coated microwell and incubated overnight at 4°C in a refrigerator. The day after, wells were washed 4 times with wash buffer. Afterwards, 100 µL of detection antibody were added to each well and incubated for 1 hour at room temperature. Wells were washed 4 times with wash buffer. 100 µL of diluted enzyme conjugate, a solution of 1 µL of conjugate per mL diluent, were added to each well and incubated for 1 hour at room temperature. After 4 washes, 100 µL of substrate solution were added to each well and the plate was incubated for 20 minutes at room temperature, developing a blue color. The reaction was stopped by adding 50 µL of 0.5M H_2SO_4 and the solution color turned yellow. Absorbances were read at 450 nm within 30 minutes. The experiment was repeated by diluting or concentrating the original samples if results were not within the standard's range.

For the TF activity kit, all reagents and working standards were diluted following manufacturer's instructions. The Assay Mix was prepared, consisting of 50 µL Assay Diluent, 10 µL FVII and 10 µL FX for each sample or standard. On each well of the 96 well plate, 70 µL of the Assay Mix were mixed gently with 10 µL of TF Standard or samples and incubated at 37ºC for 30 minutes. Afterwards, 20 µL of FXa Substrate were added and gently mixed. The absorbance at 405 nm was read at zero minutes for background OD. The plate was incubated at 37ºC and the absorbance read at 405 nm every 2 minutes for 12 minutes. The data with best signal to noise ratio before saturation were selected as final results.

5.9 – Numerical methods for simulations

According to Equation 11 and Equation 12, parabolic velocity profile in arteries can ideally be modeled by a Gaussian distribution. In order to introduce this velocity profile in the CFD software, this function was adjusted using data from real patients. Equation 12 was slightly modified into Equation 15 by adding the constant base velocity observed in real patients. The maximal velocity of the parabola for one pulse now reads:

$$v_0 = v_{base} + v_{pulse} \cdot e^{-\frac{(t-t_{pulse})^2}{\sigma^2}}$$

Equation 15 - Adjusted velocity profile for one pulse in CFD simulations

In this equation, v_{base} is the constant velocity, $v_{base} + v_{pulse}$ is the maximal velocity in the center of the artery, t_{pulse} is the time of pulse and σ the width of the pulse. This equation applies to one pulse only. If multiple pulses want to be applied, the equation for the number of pulses n_{pulse} and the heart frequency frec in beats per minute is modified as follows:

$$v_0 = v_{base} + v_{pulse} \cdot \sum_{i=0}^{n_{pulse}-1} \left(e^{-\frac{(t-t_{pulse}-i\cdot frec/60)^2}{\sigma^2}}\right)$$

Equation 16 - Adjusted velocity profile for n pulses in CFD simulations

The tangential component of the velocity vector (vTan), calculated as the dot product of its local velocity vector and the normalized direction vector representing the vessel centerline, was used as a measure of the velocity of the fluid flow. Based on this vTan metric the extent of flow recirculation was classified into three categories: severe, mild or negligible. If the maximal backwards velocity ($vTan_{MIN}$) was above 20% of the inlet velocity during the pulse, the extent of recirculation was considered severe. If $vTan_{MIN}$ was between 5% and 20%, the extent was considered mild and negligible if the former criteria were not met. vTan was evaluated at each node and all the tetrahedrons containing at least one node with negative vTan were summed to estimate the "Total Recirculating Volume" (VolRec) for each branch (EQ). The parameter "Normalized vTan·VolRec" (NVV) was calculated multiplying VolRec by vTan and dividing it by the volume of the branch and normalizing it to the value of the straight segment of the bifurcation.

$$VolRec = \sum (Tetrahedrons_{vTan<0})$$

Equation 17 - Total recirculation volume

$$NVV = \frac{\frac{vTan \cdot VolRec}{Vol\ Branch}}{\left(\frac{vTan \cdot VolRec}{Vol\ Branch}\right)_{Straight\ branch}}$$

Equation 18 - NVV calculation

The diffusion of sTF was adimensionalized in order to reduce the simulation time. Although this underestimates the convective term of the mass transfer equation, it is an approach to the actual distribution when computing resources are limited. The adimensional number π_1 (Equation 19) proves that, given a diffusivity D, a mass flow $\dot{m}$ increasing the viscosity μ of the fluid reduces the time t_D that a solute needs to diffuse.

$$\pi_1 = \frac{\mu^2 \cdot D \cdot t_D}{\dot{m}^2}$$

Equation 19 - Viscosity adimensionalization for diffusion time

The arterial bifurcation design program has three different modules that require different inputs and return different outputs. Table 4, Table 6 and Table 8 present the geometrical parameters used for the arterial bifurcations studied; Table 5, Table 7 and Table 9 show the specific inputs for each module used.

Dimension	Length (mm)	Width (mm)	Ratio
CCA 1	8	8	1
CCA 2	32	8	1
CCA 3	56	8	1
CCA 4	80	8	1
ICA 0	0	8.3	1
ICA 1	7.28	8.9	1
ICA 2	14.48	8.2	1
ICA 3	24	6	1
ICA 4	36	5.7	1
ICA 5	45	5.7	1
ECA 0	0	5.6	1
ECA 1	15	5.5	1
ECA 2	30	4.6	1
ECA 3	45	4.6	1
ECA Angle (º)	25.1	-	-
ICA Angle (º)	25.4	-	-

Table 4 - Geometrical parameters for the carotid bifurcation

Module	Parameter	Value
Simulation	First Pulse (s)	1
	Pulse Width (s)	0.05
	Frequency (bpm)	60
	V base (m/s)	0.1
	V max (m/s)	0.6
Mold Design	Thickness (mm)	1
	Tolerance (mm)	0.4
3D Print	Thickness (mm)	-

Table 5 - Specific inputs for the carotid bifurcation

Dimension	Length (mm)	Width (mm)	Ratio
LM 1	4	3.61	1
LM 2	20	3.61	1
LM 3	45	3.61	1
LM 4	70	3.61	1
LAD 0	0	2.8	1
LAD 1	5	2.8	1
LAD 2	12	2.8	1
LAD 3	24	2.8	1
LAD 4	40	2.8	1
LAD 5	60	2.8	1
LCX 0	0	2.77	1
LCX 1	15	2.77	1
LCX 2	30	2.77	1
LCX 3	60	2.77	1
LAD Angle (º)	31.5	-	-
LCX Angle (º)	31.5	-	-

Table 6 - Geometrical parameters for the flat coronary bifurcation

Module	Parameter	Value
Simulation	First Pulse (s)	0.4
	Pulse Width	0.05
	Frequency (bpm)	60
	V base (m/s)	0.05
	V max (m/s)	0.8
Mold Design	Thickness (mm)	0.6
	Tolerance (mm)	0.4
3D Print	Thickness (mm)	0.75

Table 7 - Specific inputs for the flat coronary bifurcation

Dimension	X	Y	Z	Width (mm)	Ratio
LM 1	-9.474	29.159	37.000	3.61	1
LM 2	-7.659	30.720	38.000	3.61	1
LM 3	-6.138	31.579	39.000	3.61	1
LM 4	-4.150	32.000	40.000	3.61	1
LAD 1	-21.493	23.049	37.000	2.8	1
LAD 2	-25.273	19.044	33.000	2.8	1
LAD 3	-26.968	15.570	29.000	2.8	1
LAD 4	-27.992	11.309	26.000	2.8	1
LAD 5	-27.789	6.929	24.000	2.8	1
LAD 6	-27.920	3.428	21.000	2.8	1
LCX 1	-14.365	22.120	42.000	2.77	1
LCX 2	-13.689	20.295	45.000	2.77	1
LCX 3	-12.235	18.139	49.000	2.77	1
LCX 4	-12.093	16.049	52.000	2.77	1
Bif. Center	-12.480	26.760	38.000	3.61	1

Table 8 - Geometrical parameters for the curved coronary bifurcation

Output	Parameter	Value
Simulation	First Pulse (s)	0.4
	Pulse Width (s)	0.05
	Frequency (bpm)	60
	V base (m/s)	0.05
	V max (m/s)	0.8
	Number of Pulses	2
Mold Design	Thickness (mm)	-
	Tolerance (mm)	-
3D Print	Thickness (mm)	0.75
Support	Thickness (mm)	0.75
	Tolerance (mm)	0.4

Table 9 - Specific inputs for the curved coronary bifurcation

The numerical methods used to resolve the systems of equations shown in chapter 1.6 require a series of boundary conditions. GID gives a user-friendly environment to introduce these boundary conditions and other geometrical and mathematical resolution methods as parameters. Table 10 shows the parameters modified in the simulations run, the rest were left as default. These conditions, particularly meshing size and time increment are function of each particular problem. The table shows the values used in the coronary and carotid cases. Figure 129, Figure 130 and Figure 131 show the mesh density for each case studied. For sTF distribution, with a diffusivity of $2.05 \cdot 10^{-11}$ m^2/s, initial sTF concentrations were 2.2 ng/cell for the stented area and 0.7 ng/cell in healthy regions. These data were obtained by analyzing the released sTF in injured plates (chapter 4.1.2).

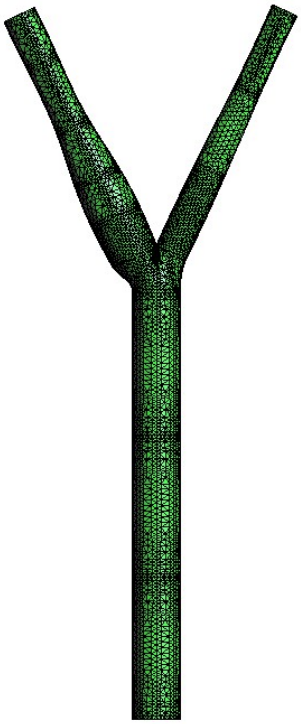

Figure 129 - Carotid bifurcation's mesh

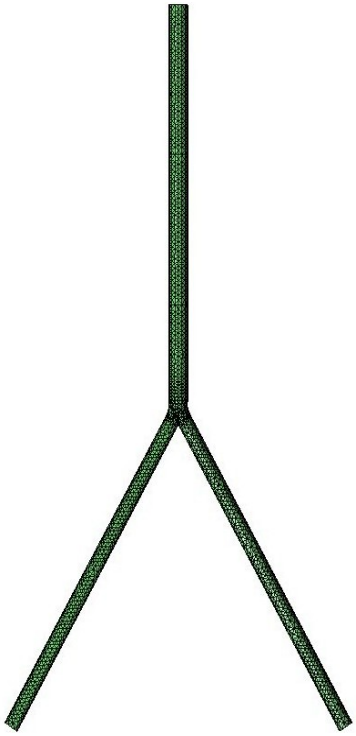

Figure 130 - Flat coronary bifurcation's mesh

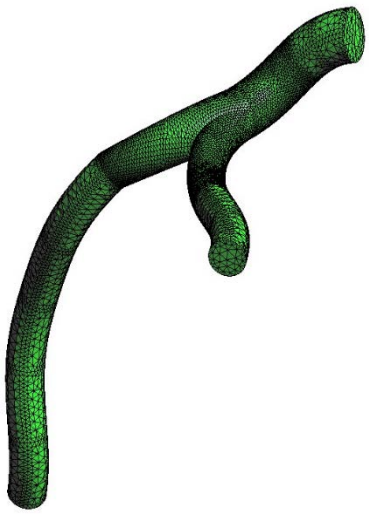

Figure 131 - Curved coronary bifurcation's mesh

GID Command	Value		
Problem Type	Tdyn 3D		
Units Data	IN/OUT	mm	
	GEOMETRY	mm	
Gravity Vector	Y=-9.81m/s^2 (Carotid) Y=9. 81m/s^2 (Flat Coronary) Z=9. 81m/s^2 (Curved Coronary)		
Results	Velocity, Pressure, Wall Shear Stress, Advection		
	Results file: ASCII		
Fluid Solver	Stab Bi-Conjugate		
Other	Use Total Pressure: 101325 Pa		
Fluid properties	Density	1035 kg/m^3	
	Viscosity	0.0035 kg/m.s	
Fluid boundaries	Wall	Bound. type	VfixWall
		Angle	0.0
	Inlet	Bound. type	Inlet VelC
		VelY field	Function of problem
	Outlet	Press. field	0.0 Pa
Analysis	Time Increment	0.5 ms	
	Number of steps	Function of problem	
	Maximal iterations	15	
Output	Output Step	Function of problem	
	Output Start	Function of problem	
Mesh Generation	Mesh Size	Coronary	Central Vol: 0.25
			Ext Vol: 0.35
		Carotid	Central Vol: 0.95
			Ext Vol: 0.7
	Size Transition	0.7	

Table 10 - Conditions for GID simulations

5.10 – Scaffold and support design

5.10.1 – Teflon® molds CNC Manufacturing

The positive molds manufacturing consisted of three processes, a “Roughing.1” followed by two consecutives “ZLevel.1”. The initial “Roughing” target was to do a rapid approximation to the geometry with a bigger tool, so the slower “ZLevel.1” would be shorter and more precise. The “Roughing” smoothed down the Teflon® pad at a radial stepover of 1/50 tool diameter ratio, with a machining tolerance of 0.1mm, using with a flat-end tool of 8mm diameter, spinning at 1000 rpm (c.f. Figure 5.6.1.1). Once finished, a first “ZLevel.1” dug along the geometry, digging at a constant stepover of 0.025mm, and a scallop height of 0.025mm, until the whole geometry was drawn. The definitive “ZLevel.2” had to be programmed to polish the figure because nor the “Roughing” nor “ZLevel.1” were able to correctly rough the area next to the bifurcation. The particular condition for “Zlevel.2” was 1mm offset both on the “Part” (whole geometry) and the “Check” (area near the bifurcation). In both “ZLevel.1” and “ZLevel.2”, the machining tolerance was 0.1mm, using a ball-end tool of 2mm diameter, spinning at 3000 rpm. (cf. Figure 5.6.1.2). The Fagor® 8055 lasted about 45 minutes to finish the complete manufacturing. The cuvette manufacture consisted in a unique “ZLevel.1” process, which dug along the geometry, digging at a constant stepover of 0.025mm, and a scallop height of 0.025mm, until the whole geometry was created. The tolerance of the machining was 0.1mm using a ball-end tool of 2mm diameter, spinning at 3000 rpm. The Fagor® 8055 lasted about 3 hours to finish the manufacturing.

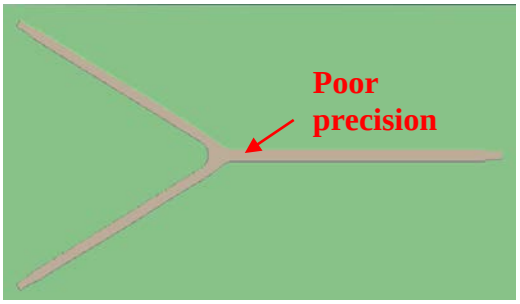

Figure 132 - Coronary artery positive mold after “Roughing”

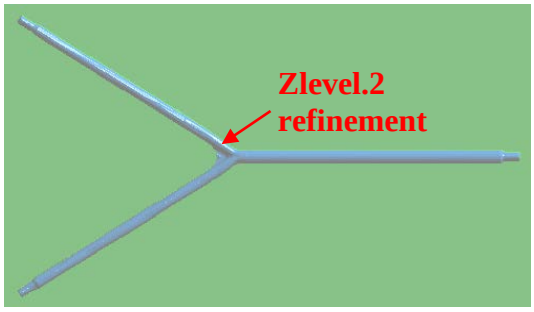

Figure 133 - Coronary artery positive mold after “ZLevel.2”

5.10.2 – Photo-polymeric scaffold 3D Printer

After running the Visual Basic® program in 3D Print module, an STL file with the desired geometry is generated. STL is the format used by 3D Printers to cast prototypes. The STL file generated was sent to ZSI, a company that gives the possibility to lend its 3D Printers. The 3D Printer used is the Objet Eden 500V. This printer offers a print resolution of 42 µm in the X and Y axis and 16 µm in the Z axis. It has a thickness limitation of 0.6mm. The material polymerized is called FULLCURE® 930 TANGOPLUS, consisting in a mix of urethane acrylate oligomer (30 to 60%), methacrylate oligomer (10 to 30%), Exo-1,7,7-trimethylbicyclo[2.2.1]hept-2-yl acrylate (10 to 30%), polyurethane (10 to 30%), and a photo-initiator (0 to 1%). The 3D printer sequentially added the liquid mix in a layer-by-layer manner, using UV light to polymerize and solidify the mixture. At the same time, the printer creates a polymeric support to ensure the stability of the scaffold. The support is dissolvable in 1 M sodium hydroxide at 37ºC and overnight agitation.

5.10.3 – Polycarbonate support 3D printer

The STL file from the square support module of the Visual basic interface was adapted and prepared by the software Insight® and sent to a Fortus 400mc (Stratasys) 3D printer that casted the polycarbonate supports for curved coronary bifurcations. This 3D printer uses fused deposition modeling (FDM) technology to cast its prototypes. Briefly, a plastic filament or metal wire is unwound from a coil, supplying material to an extrusion nozzle which can turn the flow on and off. The nozzle is heated to melt the material and can be moved in both horizontal and vertical directions by CNC and directly controlled by a computer-aided manufacturing (CAM) software package. The model is produced by extruding small beads of thermoplastic material to form layers, as the material hardens immediately after extrusion from the nozzle. In order to print the parts of the geometry that are suspended and could collapse before hardening, a support is printed (with the same material as the model, or a different one). Once the whole geometry has been 3D printed, all the supports are removed.

5.11 – Microparticle tracking

The following steps were carried out to follow microparticles flowing through the PDMS scaffolds. The studied scaffold was connected to 3.18 mm ID Silastic® tubes with two reservoirs and a peristaltic pump (Ismatec Ecoline VC-360) completing the circuit, as seen in Figure 134. The scaffold was placed under an optical microscope coupled to a recording camera Genie HM640. The circuit was filled with a water solution containing 20 g/L of dextran and 0.3 g/L of polyethylene microparticles (Cospheric, ID: BLPMS 27-45 µm, 1000 kg/m^3). Finally, the pump was connected in order to fill the reservoir 1 and make the liquid flow through the bifurcation. The fluid's velocity was regulated by varying the height of the reservoir 1. The microparticles trajectories were recorded by the camera and tracked with the software "Tracker 4.62". This process was repeated at different fluid velocities and with the carotid and flat coronary scaffolds.

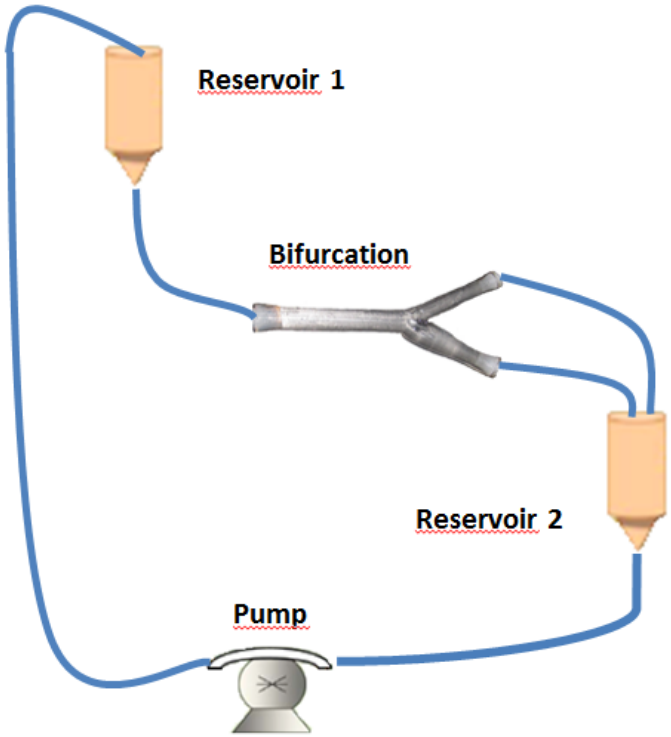

Figure 134 - Microparticle tracking experimental setup

5.12 – Statistical Analysis

The *in vitro* experiments described were performed at least by triplicate and repeated two to four separate times. In graphical presentations, data are expressed as average ± standard error of the mean and * or # means significant difference between averages. Kruskal-Wallis one-way analysis of variance followed by Scheffé's method post-hoc analysis was conducted to determine statistical differences between values; p-values < 0.05 were considered significant.

6 – CONCLUSIONS

A Visual Basic® 2010 framework was developed to replicate vascular bifurcations. The framework created the specific computer aided design files for CFD simulations, for mold manufacture using computer numeric control, and for polymeric scaffold manufacturing using photopolymeric 3D-Printers. Using conventional medical imaging techniques, arterial geometries of different patients were reconstructed based on the extracted geometric features. The files were used to run computational flow simulations that predicted velocity distributions and identified regions of flow recirculation and stagnation. A scalar metric (NVV) was defined to capture the extent of recirculation for a patient-specific geometry. The interface was also used to cast *in vitro* models of the coronary and carotid bifurcations that were manufactured in PDMS. Simulating patient-specific, physiologic conditions, endothelial cells and/or smooth muscle cells were sequentially layered and remained functional on the polymeric substrate.

Vascular health is a complex fingerprint of many factors that can be identified with markers of proliferation to give a sense of growth, expression of critical proteins give a sense of synthetic function and responsive genes and surface molecules to indicate sensitivity. Bench-top derived measurements of atherogenic and thrombotic markers and their geometry-specific variations were correlated with the model-based predictions. More specifically, VCAM-1 expression, Ox-LDL uptake and monocyte adhesion were chosen as biomarkers for atherogenesis, and tissue factor was chosen as predictor of thrombotic phenotype.

The full sequence of atherogenesis was activated in the regions of flow recirculation and stagnation. We also observed that not only flow disruptions exacerbated vascular disease indicators, but arterial flow promoted endothelial health, independently of the studied arterial bed. In particular, the amount of recirculation correlated with monocyte adhesion to activated endothelial cells and Ox-LDL uptake by quiescent endothelial cells. The expression of VCAM-1 rose when quiescent endothelial cells were exposed to flow disruptions, but this increase was muted when cells were activated with inflammatory agents. Further, tissue factor expression and thrombogenicity in SMC increased very significantly in subjects associated with a larger extent of recirculation. Soluble tissue factor from injured arterial walls predominantly nested on regions of flow recirculation. These observations highlight the importance of accounting for patient-specific geometry variations and flow derangements to extend the derived biologic inferences well beyond idealized cell culture models to real world settings. Furthermore, the data suggests that practitioners should take into account the local

recirculation as a critical parameter to define the parameters of stent placement, focusing on minimizing endothelial denudation especially in regions of flow recirculation.

Simplified straight channel models lack the spatial resolution of the different regions of a bifurcated artery. While all of the inflammation and thrombogenic biomarkers generally rose when cells were exposed to oscillatory flow and static conditions, these values showed a clear correlation with the local amount of recirculation for each branch on each arterial bed. Our model analyzes locally the recirculation extent and compares values between cells that are genetically identical and exposed to the same solutes. The main factor that varies among these cells is the amount of recirculation, which ends up altering the vascular cell phenotype. The three-dimensional approach localizes better the impact of the flow patterns but poses novel challenges at the same time. The studied biomarkers presented levels near the detection thresholds of the analytical methods applied, especially in small sections such as the recirculation regions of the bifurcated constructs. This limits, i.e., the study of TF in EC and the differentiation in signaling from SMC vs. EC in a bilayer such as the one described.

Not only are the fluid dynamics of the vessel crucial in determining thrombotic and atherosclerotic risk, but also the biochemical composition of blood flow may affect that severely. In terms of atherosclerosis, it was observed that the presence of inflammatory factors such as tumor necrosis alpha can modulate the values of the disease's biomarkers. The inflammatory cytokine TNF-α provoked global expression of VCAM-1 independently of flow regime, and triggered monocyte adhesion to endothelial cells, inexistent without it. Only Ox-LDL uptake remained unaffected by the presence of the inflammatory stimuli. In terms of thrombosis, TNF-α did not significantly modify TF expression by SMC, but uremic serum and some solutes did. In particular, uric acid, indoxil acetate and indoxil sulfate considerably augmented TF and thrombogenicity registers in SMC. This finding links the 6-fold increase in stent thrombosis in patients with chronic renal disease with the solutes' concentration in uremic serum and offers novel stent thrombosis risk predictors for these patients.

Integrated frameworks such as the one described in this thesis could be very useful in a range of biomedical fields. As an *in vitro* tool, our platform allows for a set of flow- and biochemical-related experiments that may help researchers to answer an array of biological and clinically relevant questions. The model can be extended to any bifurcated geometry, not only vascular, but respiratory or urinary as well, and represents an improvement from existing approaches.

Physicians may use it to refine the adequate treatments and adapt them to the individual state and vascular geometries of each patient and hence prevent flow- and drug-related post-implantation complications. The platform is also a cheap, reproducible, and flexible tool to test medical devices such as stents or balloons and could help pharmaceutical companies by limiting the amount of in vivo assays done on development of such devices. The platform holds the capacity to cast bio-implantable vascular grafts in a close future. Current engineering techniques already allow direct 3D printing of arterial bifurcations using biocompatible materials such as collagen-based matrices. Once the geometry of the patient had been studied, the casted implant would have the optimal fluid dynamic conditions to minimize the graft's risks like thrombosis or restenosis. The platform holds the capacity to cast bioimplantable vascular grafts in a close future

7 – REFERENCES

1. Fox SI, McGraw-Hill Companies. *Human physiology*. New York: McGraw-Hill; 2011.
2. Martorell J, Santoma P, Molins JJ, Garcia-Granada AA, Bea JA, Edelman ER, Balcells M. Engineered arterial models to correlate blood flow to tissue biological response. *Annals of the New York Academy of Sciences*. 2012;1254:51-56
3. Li YS, Haga JH, Chien S. Molecular basis of the effects of shear stress on vascular endothelial cells. *Journal of biomechanics*. 2005;38:1949-1971
4. Chiu JJ, Chien S. Effects of disturbed flow on vascular endothelium: Pathophysiological basis and clinical perspectives. *Physiological reviews*. 2011;91:327-387
5. Chiu JJ, Wang DL, Chien S, Skalak R, Usami S. Effects of disturbed flow on endothelial cells. *J Biomech Eng*. 1998;120:2-8
6. Chien S. Mechanotransduction and endothelial cell homeostasis: The wisdom of the cell. *American journal of physiology. Heart and circulatory physiology*. 2007;292:H1209-1224
7. Phelps JE, DePaola N. Spatial variations in endothelial barrier function in disturbed flows in vitro. *American journal of physiology. Heart and circulatory physiology*. 2000;278:H469-476
8. Davies PF, Remuzzi A, Gordon EJ, Dewey CF, Jr., Gimbrone MA, Jr. Turbulent fluid shear stress induces vascular endothelial cell turnover in vitro. *Proc Natl Acad Sci U S A*. 1986;83:2114-2117
9. Myers DD, Hawley AE, Farris DM, Wrobleski SK, Thanaporn P, Schaub RG, Wagner DD, Kumar A, Wakefield TW. P-selectin and leukocyte microparticles are associated with venous thrombogenesis. *Journal of vascular surgery*. 2003;38:1075-1089
10. Chiu JJ, Chen CN, Lee PL, Yang CT, Chuang HS, Chien S, Usami S. Analysis of the effect of disturbed flow on monocytic adhesion to endothelial cells. *Journal of biomechanics*. 2003;36:1883-1895
11. Liu Y, Chen BP, Lu M, Zhu Y, Stemerman MB, Chien S, Shyy JY. Shear stress activation of srebp1 in endothelial cells is mediated by integrins. *Arterioscler Thromb Vasc Biol*. 2002;22:76-81
12. Skilbeck C, Westwood SM, Walker PG, David T, Nash GB. Dependence of adhesive behavior of neutrophils on local fluid dynamics in a region with recirculating flow. *Biorheology*. 2001;38:213-227
13. Chen CN, Chang SF, Lee PL, Chang K, Chen LJ, Usami S, Chien S, Chiu JJ. Neutrophils, lymphocytes, and monocytes exhibit diverse behaviors in transendothelial and

subendothelial migrations under coculture with smooth muscle cells in disturbed flow. *Blood*. 2006;107:1933-1942

14. Warboys CM, Amini N, de Luca A, Evans PC. The role of blood flow in determining the sites of atherosclerotic plaques. *F1000 medicine reports*. 2011;3:5
15. Burt HM, Hunter WL. Drug-eluting stents: An innovative multidisciplinary drug delivery platform. *Advanced drug delivery reviews*. 2006;58:345-346
16. Richter Y, Groothuis A, Seifert P, Edelman ER. Dynamic flow alterations dictate leukocyte adhesion and response to endovascular interventions. *The Journal of clinical investigation*. 2004;113:1607-1614
17. Chatzizisis YS, Jonas M, Coskun AU, Beigel R, Stone BV, Maynard C, Gerrity RG, Daley W, Rogers C, Edelman ER, Feldman CL, Stone PH. Prediction of the localization of high-risk coronary atherosclerotic plaques on the basis of low endothelial shear stress: An intravascular ultrasound and histopathology natural history study. *Circulation*. 2008;117:993-1002
18. Methe H, Balcells M, Alegret Mdel C, Santacana M, Molins B, Hamik A, Jain MK, Edelman ER. Vascular bed origin dictates flow pattern regulation of endothelial adhesion molecule expression. *American journal of physiology. Heart and circulatory physiology*. 2007;292:H2167-2175
19. Hansson GK, Robertson AK, Soderberg-Naucler C. Inflammation and atherosclerosis. *Annual review of pathology*. 2006;1:297-329
20. Niessner A, Goronzy JJ, Weyand CM. Immune-mediated mechanisms in atherosclerosis: Prevention and treatment of clinical manifestations. *Current pharmaceutical design*. 2007;13:3701-3710
21. Siegel-Axel D, Daub K, Seizer P, Lindemann S, Gawaz M. Platelet lipoprotein interplay: Trigger of foam cell formation and driver of atherosclerosis. *Cardiovascular research*. 2008;78:8-17
22. Zernecke A, Bernhagen J, Weber C. Macrophage migration inhibitory factor in cardiovascular disease. *Circulation*. 2008;117:1594-1602
23. Hamik A, Lin Z, Kumar A, Balcells M, Sinha S, Katz J, Feinberg MW, Gerzsten RE, Edelman ER, Jain MK. Kruppel-like factor 4 regulates endothelial inflammation. *The Journal of biological chemistry*. 2007;282:13769-13779
24. Waldo SW, Li Y, Buono C, Zhao B, Billings EM, Chang J, Kruth HS. Heterogeneity of human macrophages in culture and in atherosclerotic plaques. *The American journal of pathology*. 2008;172:1112-1126

25. Doran AC, Meller N, McNamara CA. Role of smooth muscle cells in the initiation and early progression of atherosclerosis. *Arterioscler Thromb Vasc Biol*. 2008;28:812-819

26. Pepine CJ. The effects of angiotensin-converting enzyme inhibition on endothelial dysfunction: Potential role in myocardial ischemia. *The American journal of cardiology*. 1998;82:23S-27S

27. Duran M. Propietats espectroscòpiques anòmales del 9-amino-2,7,12,17-tetrafenilporficè. *Photochemistry*. 2010;Treball Final de Carrera

28. Voorhees AB, Jr., Jaretzki A, 3rd, Blakemore AH. The use of tubes constructed from vinyon "n" cloth in bridging arterial defects. *Annals of surgery*. 1952;135:332-336

29. Browning MB, Dempsey D, Guiza V, Becerra S, Rivera J, Russell B, Hook M, Clubb F, Miller M, Fossum T, Dong JF, Bergeron AL, Hahn M, Cosgriff-Hernandez E. Multilayer vascular grafts based on collagen-mimetic proteins. *Acta biomaterialia*. 2012;8:1010-1021

30. Dahl SL, Kypson AP, Lawson JH, Blum JL, Strader JT, Li Y, Manson RJ, Tente WE, DiBernardo L, Hensley MT, Carter R, Williams TP, Prichard HL, Dey MS, Begelman KG, Niklason LE. Readily available tissue-engineered vascular grafts. *Science translational medicine*. 2011;3:68ra69

31. Greenwald SE, Berry CL. Improving vascular grafts: The importance of mechanical and haemodynamic properties. *The Journal of pathology*. 2000;190:292-299

32. Klinkert P, Post PN, Breslau PJ, van Bockel JH. Saphenous vein versus ptfe for above-knee femoropopliteal bypass. A review of the literature. *European journal of vascular and endovascular surgery : the official journal of the European Society for Vascular Surgery*. 2004;27:357-362

33. Ravi S, Chaikof EL. Biomaterials for vascular tissue engineering. *Regenerative medicine*. 2010;5:107-120

34. Iwasaki K, Kojima K, Kodama S, Paz AC, Chambers M, Umezu M, Vacanti CA. Bioengineered three-layered robust and elastic artery using hemodynamically-equivalent pulsatile bioreactor. *Circulation*. 2008;118:S52-57

35. Edelman ER, Rogers C. Hoop dreams. Stents without restenosis. *Circulation*. 1996;94:1199-1202

36. Rogers C, Tseng DY, Squire JC, Edelman ER. Balloon-artery interactions during stent placement: A finite element analysis approach to pressure, compliance, and stent design as contributors to vascular injury. *Circulation research*. 1999;84:378-383

37. Edelman ER, Rogers C. Pathobiologic responses to stenting. *The American journal of cardiology*. 1998;81:4E-6E

38. Garcia-Garcia HM, Vaina S, Tsuchida K, Serruys PW. Drug-eluting stents. *Archivos de cardiologia de Mexico*. 2006;76:297-319

39. Pache J, Dibra A, Mehilli J, Dirschinger J, Schomig A, Kastrati A. Drug-eluting stents compared with thin-strut bare stents for the reduction of restenosis: A prospective, randomized trial. *European heart journal*. 2005;26:1262-1268

40. Luscher TF, Steffel J, Eberli FR, Joner M, Nakazawa G, Tanner FC, Virmani R. Drug-eluting stent and coronary thrombosis: Biological mechanisms and clinical implications. *Circulation*. 2007;115:1051-1058

41. Yang YJ, Kang S, Xu B, Chen JL, Qiao SB, Qin XW, Yao M, Chen J, Wu YJ, Liu HB, Yuan JQ, You SJ, Li JJ, Dai J, Gao RL. Short- and long-term outcomes of single bare metal stent versus drug eluting stent in nondiabetic patients with a simple de novo lesion in the middle and large vessel. *Journal of translational medicine*. 2008;6:42

42. Gallego L, Martinez-Selles M, Garcia E, Franco J, Estevez A, Sarnago Cebada F, Fernandez-Aviles F. Characteristics and outcome of angiographically confirmed stent thrombosis. *Revista espanola de cardiologia*. 2009;62:220-223

43. Chitalia VC, Shivanna S, Martorell J, Balcells M, Bosch I, Kolandaivelu K, Edelman ER. Uremic serum and solutes increase post-vascular interventional thrombotic risk through altered stability of smooth muscle cell tissue factor. *Circulation*. 2013;127:365-376

44. Balcells M, Martorell J, Olive C, Santacana M, Chitalia V, Cardoso AA, Edelman ER. Smooth muscle cells orchestrate the endothelial cell response to flow and injury. *Circulation*. 2010;121:2192-2199

45. Kolachalama VB, Levine EG, Edelman ER. Luminal flow amplifies stent-based drug deposition in arterial bifurcations. *PloS one*. 2009;4:e8105

46. Drachman DE, Edelman ER, Seifert P, Groothuis AR, Bornstein DA, Kamath KR, Palasis M, Yang D, Nott SH, Rogers C. Neointimal thickening after stent delivery of paclitaxel: Change in composition and arrest of growth over six months. *Journal of the American College of Cardiology*. 2000;36:2325-2332

47. Tzafriri AR, Vukmirovic N, Kolachalama VB, Astafieva I, Edelman ER. Lesion complexity determines arterial drug distribution after local drug delivery. *Journal of controlled release : official journal of the Controlled Release Society*. 2010;142:332-338

48. Steffel J, Latini RA, Akhmedov A, Zimmermann D, Zimmerling P, Luscher TF, Tanner FC. Rapamycin, but not fk-506, increases endothelial tissue factor expression: Implications for drug-eluting stent design. *Circulation*. 2005;112:2002-2011

49. Breitenstein A, Camici GG, Tanner FC. Tissue factor: Beyond coagulation in the cardiovascular system. *Clinical science*. 2010;118:159-172

50. Broze GJ, Jr. Tissue factor pathway inhibitor and the revised theory of coagulation. *Annual review of medicine*. 1995;46:103-112

51. Chris Pallister AG, Malcolm S. Watson. *Haematology*. Scion Publishing; 2010.

52. Abcam. Blood coagulation cascade.

53. Furie B, Furie BC. Mechanisms of thrombus formation. *The New England journal of medicine*. 2008;359:938-949

54. Mandal SK, Pendurthi UR, Rao LV. Cellular localization and trafficking of tissue factor. *Blood*. 2006;107:4746-4753

55. Pendurthi UR, Ghosh S, Mandal SK, Rao LV. Tissue factor activation: Is disulfide bond switching a regulatory mechanism? *Blood*. 2007;110:3900-3908

56. Steffel J, Luscher TF, Tanner FC. Tissue factor in cardiovascular diseases: Molecular mechanisms and clinical implications. *Circulation*. 2006;113:722-731

57. Giesen PL, Rauch U, Bohrmann B, Kling D, Roque M, Fallon JT, Badimon JJ, Himber J, Riederer MA, Nemerson Y. Blood-borne tissue factor: Another view of thrombosis. *Proc Natl Acad Sci U S A*. 1999;96:2311-2315

58. Ting HH, Tahirkheli NK, Berger PB, McCarthy JT, Timimi FK, Mathew V, Rihal CS, Hasdai D, Holmes DR, Jr. Evaluation of long-term survival after successful percutaneous coronary intervention among patients with chronic renal failure. *The American journal of cardiology*. 2001;87:630-633, A639

59. Park DW, Park SW, Park KH, Lee BK, Kim YH, Lee CW, Hong MK, Kim JJ, Park SJ. Frequency of and risk factors for stent thrombosis after drug-eluting stent implantation during long-term follow-up. *The American journal of cardiology*. 2006;98:352-356

60. Iakovou I, Schmidt T, Bonizzoni E, Ge L, Sangiorgi GM, Stankovic G, Airoldi F, Chieffo A, Montorfano M, Carlino M, Michev I, Corvaja N, Briguori C, Gerckens U, Grube E, Colombo A. Incidence, predictors, and outcome of thrombosis after successful implantation of drug-eluting stents. *JAMA : the journal of the American Medical Association*. 2005;293:2126-2130

61. Kimura T, Morimoto T, Kozuma K, Honda Y, Kume T, Aizawa T, Mitsudo K, Miyazaki S, Yamaguchi T, Hiyoshi E, Nishimura E, Isshiki T, Investigators R. Comparisons of baseline demographics, clinical presentation, and long-term outcome among patients with early, late, and very late stent thrombosis of sirolimus-eluting stents: Observations from the registry of stent thrombosis for review and reevaluation (restart). *Circulation*. 2010;122:52-61

62. Lasala JM, Cox DA, Dobies D, Baran K, Bachinsky WB, Rogers EW, Breall JA, Lewis DH, Song A, Starzyk RM, Mascioli SR, Dawkins KD, Baim DS, Arrive, Physicians AP. Drug-eluting stent thrombosis in routine clinical practice: Two-year outcomes and predictors from the taxus arrive registries. *Circulation. Cardiovascular interventions*. 2009;2:285-293

63. Lambert ND, Sacrinty MT, Ketch TR, Turner SJ, Santos RM, Daniel KR, Applegate RJ, Kutcher MA, Sane DC. Chronic kidney disease and dipstick proteinuria are risk factors for stent thrombosis in patients with myocardial infarction. *American heart journal*. 2009;157:688-694

64. Mercier E, Branger B, Vecina F, Al-Sabadani B, Berlan J, Dauzat M, Fourcade J, Gris JC. Tissue factor coagulation pathway and blood cells activation state in renal insufficiency. *The hematology journal : the official journal of the European Haematology Association / EHA*. 2001;2:18-25

65. Dubin R, Cushman M, Folsom AR, Fried LF, Palmas W, Peralta CA, Wassel C, Shlipak MG. Kidney function and multiple hemostatic markers: Cross sectional associations in the multi-ethnic study of atherosclerosis. *BMC nephrology*. 2011;12:3

66. Serradell M, Diaz-Ricart M, Cases A, Zurbano MJ, Aznar-Salatti J, Lopez-Pedret J, Ordinas A, Escolar G. Uremic medium disturbs the hemostatic balance of cultured human endothelial cells. *Thrombosis and haemostasis*. 2001;86:1099-1105

67. Kario K, Matsuo T, Matsuo M, Koide M, Yamada T, Nakamura S, Sakata T, Kato H, Miyata T. Marked increase of activated factor vii in uremic patients. *Thrombosis and haemostasis*. 1995;73:763-767

68. Miyazaki Y, Nomura S, Miyake T, Kagawa H, Kitada C, Taniguchi H, Komiyama Y, Fujimura Y, Ikeda Y, Fukuhara S. High shear stress can initiate both platelet aggregation and shedding of procoagulant containing microparticles. *Blood*. 1996;88:3456-3464

69. Lin MC, Almus-Jacobs F, Chen HH, Parry GC, Mackman N, Shyy JY, Chien S. Shear stress induction of the tissue factor gene. *The Journal of clinical investigation*. 1997;99:737-744

70. Grabowski EF, Reininger AJ, Petteruti PG, Tsukurov O, Orkin RW. Shear stress decreases endothelial cell tissue factor activity by augmenting secretion of tissue factor pathway inhibitor. *Arterioscler Thromb Vasc Biol*. 2001;21:157-162

71. Badimon L, Badimon JJ, Galvez A, Chesebro JH, Fuster V. Influence of arterial damage and wall shear rate on platelet deposition. Ex vivo study in a swine model. *Arteriosclerosis*. 1986;6:312-320

72. Blackman BR, Garcia-Cardena G, Gimbrone MA, Jr. A new in vitro model to evaluate differential responses of endothelial cells to simulated arterial shear stress waveforms. *J Biomech Eng*. 2002;124:397-407

73. DePaola N, Gimbrone MA, Jr., Davies PF, Dewey CF, Jr. Vascular endothelium responds to fluid shear stress gradients. *Arteriosclerosis and thrombosis : a journal of vascular biology / American Heart Association*. 1992;12:1254-1257

74. Kolandaivelu K, Edelman ER. Low background, pulsatile, in vitro flow circuit for modeling coronary implant thrombosis. *J Biomech Eng*. 2002;124:662-668

75. Kolandaivelu K, Edelman ER. Environmental influences on endovascular stent platelet reactivity: An in vitro comparison of stainless steel and gold surfaces. *J Biomed Mater Res A*. 2004;70:186-193

76. Kolandaivelu K, Swaminathan R, Gibson WJ, Kolachalama VB, Nguyen-Ehrenreich KL, Giddings VL, Coleman L, Wong GK, Edelman ER. Stent thrombogenicity early in high-risk interventional settings is driven by stent design and deployment and protected by polymer-drug coatings. *Circulation*. 2011;123:1400-1409

77. Castro MA, Putman CM, Cebral JR. Computational fluid dynamics modeling of intracranial aneurysms: Effects of parent artery segmentation on intra-aneurysmal hemodynamics. *AJNR. American journal of neuroradiology*. 2006;27:1703-1709

78. White FM. *Fluid mechanics*. New York, N.Y.: McGraw Hill; 2011.

79. J Marinel·lo Roura JJS. *Diagnóstico hemodinámico en angiología y cirugía vascular*. Barcelona: Ed. Glosa; 2003.

80. Abbott MB, Basco DR. *Computational fluid dynamics : An introduction for engineers*. Harlow, Essex, England, New York: Longman Scientific & Technical ; Wiley; 1989.

81. Petterson NOH. *Introduction to the finite element method*. New York: Ed. Prentice Hall; 1992.

82. Tdyn. Http://www.Compassis.Com/compass/en/productos/tdyn. 02-12-2013
83. Kolachalama VB, Bressloff NW, Nair PB. Mining data from hemodynamic simulations via bayesian emulation. *Biomedical engineering online*. 2007;6:47
84. Martorell J. In silico and in vitro study of physical and biological effects of stenting complex vascular environments. *Chemical Engineering Department, Biotechnology Section*. 2010;Masters in Chemical Engineering
85. Group TSC. Http://www.Surgcare.Net/surgery/carotid.Htm. 10-07-2008
86. Aldoori MI, Benveniste GL, Baird RN, Horrocks M, Fairgrieve J. Asymptomatic carotid murmur: Ultrasonic factors influencing outcome. *The British journal of surgery*. 1987;74:496-499
87. Rajagopalan S, Somers EC, Brook RD, Kehrer C, Pfenninger D, Lewis E, Chakrabarti A, Richardson BC, Shelden E, McCune WJ, Kaplan MJ. Endothelial cell apoptosis in systemic lupus erythematosus: A common pathway for abnormal vascular function and thrombosis propensity. *Blood*. 2004;103:3677-3683
88. Collier ME, Ettelaie C. Induction of endothelial cell proliferation by recombinant and microparticle-tissue factor involves beta1-integrin and extracellular signal regulated kinase activation. *Arterioscler Thromb Vasc Biol*. 2010;30:1810-1817
89. Welty-Wolf KE, Carraway MS, Miller DL, Ortel TL, Ezban M, Ghio AJ, Idell S, Piantadosi CA. Coagulation blockade prevents sepsis-induced respiratory and renal failure in baboons. *American journal of respiratory and critical care medicine*. 2001;164:1988-1996
90. Szotowski B, Antoniak S, Poller W, Schultheiss HP, Rauch U. Procoagulant soluble tissue factor is released from endothelial cells in response to inflammatory cytokines. *Circulation research*. 2005;96:1233-1239
91. Jimenez-Quevedo P, Sabate M, Angiolillo DJ, Alfonso F, Hernandez-Antolin R, Gomez-Hospital JA, Sanmartin M, Banuelos C, Moreno R, Escaned J, Fernandez C, Costa MA, Fernandez-Aviles F, Macaya C. [efficacy of sirolimus-eluting stent implantation in diabetic patients with very small vessels (< or = 2.25 mm). Insights from the diabetes trial]. *Revista espanola de cardiologia*. 2006;59:1000-1007
92. Vassilev D, Gil RJ. Relative dependence of diameters of branches in coronary bifurcations after stent implantation in main vessel--importance of carina position. *Kardiologia polska*. 2008;66:371-378; discussion 379
93. Darling D. Http://www.Daviddarling.Info/images/coronary_arteries.Jpg. 04-28-2013

94. Hozumi T, Yoshida K, Akasaka T, Asami Y, Ogata Y, Takagi T, Kaji S, Kawamoto T, Ueda Y, Morioka S. Noninvasive assessment of coronary flow velocity and coronary flow velocity reserve in the left anterior descending coronary artery by doppler echocardiography: Comparison with invasive technique. *Journal of the American College of Cardiology*. 1998;32:1251-1259

95. Yasu T, Yamagishi M, Beppu S, Nagata S, Miyatake K. Left main coronary flow velocity associated with stenosis. Evaluation by transesophageal color-guided pulsed doppler technique. *Chest*. 1993;104:690-693

96. Halligan KE, Jourd'heuil FL, Jourd'heuil D. Cytoglobin is expressed in the vasculature and regulates cell respiration and proliferation via nitric oxide dioxygenation. *The Journal of biological chemistry*. 2009;284:8539-8547

97. Davies MJ, Gordon JL, Gearing AJ, Pigott R, Woolf N, Katz D, Kyriakopoulos A. The expression of the adhesion molecules icam-1, vcam-1, pecam, and e-selectin in human atherosclerosis. *The Journal of pathology*. 1993;171:223-229

98. Chappell DC, Varner SE, Nerem RM, Medford RM, Alexander RW. Oscillatory shear stress stimulates adhesion molecule expression in cultured human endothelium. *Circulation research*. 1998;82:532-539

99. Nakashima Y, Raines EW, Plump AS, Breslow JL, Ross R. Upregulation of vcam-1 and icam-1 at atherosclerosis-prone sites on the endothelium in the apoe-deficient mouse. *Arterioscler Thromb Vasc Biol*. 1998;18:842-851

100. Kolachalama VB, Tzafriri AR, Arifin DY, Edelman ER. Luminal flow patterns dictate arterial drug deposition in stent-based delivery. *Journal of controlled release : official journal of the Controlled Release Society*. 2009;133:24-30

101. Camici GG, Steffel J, Amanovic I, Breitenstein A, Baldinger J, Keller S, Luscher TF, Tanner FC. Rapamycin promotes arterial thrombosis in vivo: Implications for everolimus and zotarolimus eluting stents. *European heart journal*. 2010;31:236-242

102. Chitalia V, Shivanna S, Martorell J, Meyer R, Edelman E, Rahimi N. C-cbl, a ubiquitin e3 ligase that targets active beta-catenin - a novel layer of wnt regulation. *The Journal of biological chemistry*. 2013

103. Brunet P, Gondouin B, Duval-Sabatier A, Dou L, Cerini C, Dignat-George F, Jourde-Chiche N, Argiles A, Burtey S. Does uremia cause vascular dysfunction? *Kidney & blood pressure research*. 2011;34:284-290

8 – ANNEXES (CD)

8.1 – Arterial Replication Platform.exe

8.2 – Recirculation Volume.exe

8.3 – Balcells et al. Circulation 2010.pdf

8.4 – Martorell et al. Tecnicas Endovasculares 2011.pdf

8.5 – Martorell et al. Annals NYAS 2012.pdf

8.6 – Martorell et al. Tecnicas Endovasculares 2013.pdf

8.7 – Chitalia et at. Circulation 2013.pdf